University of California
Los Angeles

Supermassive Black Hole Growth During The Peak Of Cosmic Star Formation

A dissertation submitted in partial satisfaction
of the requirements for the degree
Doctor of Philosophy in Astronomy

by

Nathaniel Robert Ross

2016

Abstract of the Dissertation

Supermassive Black Hole Growth During The Peak Of Cosmic Star Formation

by

Nathaniel Robert Ross

Doctor of Philosophy in Astronomy

University of California, Los Angeles, 2016

Professor Matthew A. Malkan, Chair

Massive galaxies in the nearby universe all show evidence of a central Supermassive Black Hole. The black holes are seen to grow over time by accretion of gas from their host galaxy, a phenomenon referred to as an Active Galactic Nucleus. This process is believed to be fundamental to the observed correlations between black hole mass and properties of the host galaxies. We have a more limited and biased understanding of the growth of supermassive black holes in more 'typical' galaxies at $z \sim 1-2$. In this work, we search for Active Galactic Nuclei in a population of star-forming galaxies spanning a mass range of $M_* \sim 10^7 - 10^{12}$ $M_\odot$ at $0.62 < z < 2.39$, during the peak of cosmic star formation and massive black hole growth. Our data are drawn from the WFC3 Infrared Spectroscopic Parallels (WISP) survey, for which we designed and implemented a suite of data analysis routines for discovering and measuring star-forming galaxies and active galactic nuclei. We find a sample of 50 active galactic nuclei, identified by their strong, rest-frame optical, emission-line ratios. We find that growing supermassive black holes in low-mass galaxies at $z \gtrsim 1$ either make up a greater fraction of their galaxies' masses than those in massive galaxies, or perhaps emit a greater fraction of their energy in [O III].

The dissertation of Nathaniel Robert Ross is approved.

Dino DiCarlo

Alice E. Shapley

Matthew A. Malkan, Committee Chair

University of California, Los Angeles

2016

Dedicated to the memories of my grandparents, John & Helen Ross and Bahjat & Ann Yousif. They have each had a great impact on my life and been a source of inspiration in good times and bad.

Table of Contents

List of Figures

List of Tables

Acknowledgments

I have so many people to acknowledge and thank for supporting me through this dissertation. I have learned so much from my professors at UCLA, and would especially like to thank Alice Shapley, who organized the extragalactic reading group and so many other interesting discussions; Steve Furlanetto, whose seminar on the First Galaxies helped inspire some of the discussion in this work; Ned Wright, for his enthusiasm for Astro-ph Coffee. I also thank the WISP team for their assistance in the data reduction and analysis, especially James Colbert, Hakim Atek, Mark Rafelski, Sophia Dai, Claudia Scarlata, Dan Masters, Michael Rutkowski, Vihang Mehta, Micaela Bagley, Melanie Noble Beck, and Alaina Henry. I also want to thank all of the UCLA graduate students, past and present, who helped troubleshoot computer issues, advise on data analysis techniques, and provide emotional support in times of stress, especially: Fred Davies, Shane Frewen, Ian Crossfield, Betsy Mills, Ryan Sanders, Kathy Kornei, Adam Greenberg, Kevin Hainline, Robin Rehagen, Anna Boehle, Julia Fang, Tom Esposito, and David Rodriguez. I'd like to thank my advisor, Matt Malkan, for being an enthusiastic observer, willing to send me all over the world for a telescope run and to stay up all night with me on Lick runs. Finally, I thank my parents, Robert and Sue Ross, without whose love and support, I would not be the man I am today.

Vita

2005	Fenwick High School, Oak Park, Illinois.
2009	B.S. (Physics, Astronomy), The Ohio State University, Columbus, Ohio. *Summa Cum Laude, Phi Beta Kappa,* *with Research Distinction in Astronomy*
2011	M.S. (Astronomy), UCLA, Los Angeles, California.

CHAPTER 1

Introduction

In the nearby universe, nearly all galaxies with massive spheroidal components of their stellar distributions show evidence of a central Super-massive Black Holes (SMBH) (e.g. Kormendy & Richstone, 1995; Richstone et al., 1998; Magorrian et al., 1998). These black holes are seen to grow by accreting gas from the surrounding galaxy (Soltan, 1982). As gas spirals in toward the black hole it is viscously heated and shines brightly across the electromagnetic spectrum. We refer to this phenomenon as an "Active Galactic Nucleus" (AGN). In the brightest AGN, the luminosity of the SMBH accretion disk outshines the combined starlight of all of the stars in the galaxy.

The gravitational potential of a galaxy is dominated by the black hole only within the central several parsecs. Nonetheless, in the past 20 years, astronomers have discovered strong correlations between SMBH mass and host galaxy properties at much larger scales, such as spheroid stellar mass, luminosity, and velocity dispersion (e.g. Magorrian et al., 1998; Ferrarese & Merritt, 2000; Gebhardt et al., 2000; Treu et al., 2004; Häring & Rix, 2004; Woo et al., 2008; Gültekin et al., 2009). These relations have their strongest constraints from measurements of nearby galaxies. There is controversy over whether these relationships evolve (e.g. Bennert et al., 2011; Park et al., 2015) or remain constant (e.g. Schulze & Wisotzki, 2014; Shen et al., 2015; Sun et al., 2015) over the history of the universe. To explain these correlations at least one of two things must be true: either the SMBH host galaxies must funnel a fixed fraction of their gas into the central few

parsecs to be accreted onto the black hole (e.g. Kauffmann & Haehnelt, 2000), or else the radiation from accretion onto the black hole may be a source of negative feedback to quench star formation in the host galaxy (e.g. Cattaneo et al., 2006).

While the accretion disks of AGN emit light across the electromagnetic spectrum, they are perhaps most notable for their bright X-ray emission, which is believed to come from the inverse Compton scattering of UV photons from the accretion disk by hot electrons (e.g. Haardt & Maraschi, 1993). Furthermore, the X-ray luminosity of the AGN is typically much greater than can be produced by thermal bremsstrahlung or X-ray binaries in the host galaxy (e.g. Laird et al., 2010). However, large columns of neutral hydrogen ($N_H > 10^{24}$ cm^{-2}) can absorb X-rays, causing some AGN to be missed by X-ray surveys. The X-ray selection of AGN has proven difficult at higher redshifts, where only a few very deep X-ray surveys are sensitive enough to detect moderately-accreting AGN and may completely miss a significant population of obscured AGN. Furthermore, spectroscopic follow-up of X-ray-selected AGN at $z > 1$ frequently fails to detect emission lines, which makes it hard to determine the distance, and therefore the luminosity, of the host (Aird et al., 2010).

Beyond the X-ray, the emission properties of AGN can become quite complicated. Unobscured, Type 1, AGN typically show a power-law continuum extending from the rest-frame UV to near-IR. With moderate dust reddening, they may have a second peak in their Spectral Energy Distributions (SEDs) in the mid-infrared, believed to come from thermal emission of "hot" dust ($\sim 40-100$ K, e.g. Edelson & Malkan, 1986) at the outskirts of the accretion disk. Type 1 AGN also typically show broad permitted lines with line widths in excess of 2000 km s^{-1}, possibly originating from a wind driven from the surface of the accretion disk by radiation pressure (e.g. Konigl & Kartje, 1994; Kashi et al., 2013). Obscured, Type 2, AGN may have the majority of the UV–optical power-law continuum hidden by dust absorption, with a larger fration of their bolometric luminosities

emitted in the infrared. Both Type 1 and Type 2 AGN show strong "narrow" forbidden-line emission and permitted line components with line widths of several hundred km s^{-1}. The narrow-line regions of AGN have higher gas densities ($10^2 - 10^4$ cm^{-3}) and emission-line ratios consistent with ionization by the hard UV continuum of the accretion disk (e.g. Koski, 1978; Vaona et al., 2012; Zhang et al., 2013). The narrow-line region may extend as far as $R_{\rm NLR} \sim 7$ kpc into the host galaxies of the most luminous AGN (Hainline et al., 2014).

It is still uncertain how the gas that fuels SMBH growth is delivered into the central pc to be accreted by the black hole. The simulations of Hopkins et al. (2005, 2006) demonstrated that gas-rich major mergers of galaxies can funnel gas at low angular momentum in sufficient amounts to explain quasar luminosities and lifetimes. Treister et al. (2012), however, found evidence of major mergers around only the brightest of AGN in a sample that spanned a range 10^{43} erg/s$<$ $L_{bol} < 10^{46}$ erg/s. For lower AGN luminosities (and accretion rates), gas could be delivered to the SMBH through interaction with a stellar bar structure or through minor galaxy mergers.

Even less is known about the origins of SMBH. There are two general scenarios for SMBH seed formation: (1) $\sim 100 - 1000$ $M_\odot$ remnants of the first generation of stars formed in the universe, or (2) direct collapse of gas to form $\sim 10^4 - 10^5$ $M_\odot$ SMBH seeds (Agarwal et al., 2012; Johnson et al., 2013). In the low-mass seed scenario, multiple seeds are expected to form, migrate together by dynamical friction, and merge in a Hubble time. However, relativistic simulations show that the merger of unequal-mass black holes produces a kick that imparts a velocity[1] to the merged black hole, causing it to migrate around the host galaxy or even be ejected from the halo entirely (Blecha & Loeb, 2008; Tanaka & Haiman, 2009). Thus, in some cases, black hole mergers can actually deplete a dark matter halo of its massive black hole instead of increasing its mass.

[1]Due to the anisotropic radiation of gravitational waves during the final stages of the merger.

The direct collapse scenario for forming SMBH seeds requires gas that is unable to cool efficiently, in order to prevent Jeans fragmentation (Jeans, 1902). In other words, the gas must have essentially no enrichment from heavy elements and no molecular hydrogen (e.g. Bromm & Loeb, 2003). As the gas collapses, it becomes very optically thick and, for a large fraction of the interior of the cloud, the diffusion timescale for photons in the gas exceeds the infall rate of the gas. Thus the photons are carried along with the gas as it collapses into the black hole in a hidden, super-Eddington accretion mode (Alexander & Natarajan, 2014). However, the large UV radiation background required to dissociate molecular hydrogen may imply that the halo be in close proximity to a rapidly-star-forming companion galaxy (Agarwal et al., 2014).

In order to place constraints on the theories of SMBH origin and evolution, we require samples of AGN that span cosmic history and the vast array of galactic environments. The redshift regime $1 < z < 2.5$ encompasses the peak in the star formation history of the universe (e.g. Madau & Dickinson, 2014; and references therein) and of peak SMBH growth, as measured by X-rays (Hopkins et al., 2007; Aird et al., 2010). By $z \sim 1$, all of the strong rest-frame-optical emission lines for star-forming galaxies (SFG) and active galactic nuclei (AGN) are redshifted into the near-infrared (NIR). Large rest-frame-optical spectroscopic samples of galaxies in this redshift range have been impeded by the strong NIR atmospheric absorption and emission, the poor sensitivity of NIR spectrographs, and the paucity of NIR multi-object spectrographs. With the new age of multi-object NIR spectrographs on 8–10m-class telescopes, larger spectroscopic samples are beginning to be assembled, although they are limited to redshift ranges where the strong rest-frame-optical lines fall in relatively transparent atmospheric windows (e.g. Steidel et al., 2014; Kriek et al., 2015).

A complementary approach for building up rest-frame-optical spectroscopic samples of galaxies at $z > 1$ is to use a spectrograph that is above the Earth's

atmosphere. This method was successfully carried out in the past with the slitless grism spectrographs on the *Hubble Space Telescope* (*HST*) Near Infrared Camera and Multi-Object Spectrometer (NICMOS, Thompson et al., 1998) and Advanced Camera for Surveys (ACS, Ford et al., 1998) in the HST-NICMOS parallel grism survey (McCarthy et al., 1999; Shim et al., 2009) and PEARS Survey (Straughn et al., 2009; Pirzkal et al., 2013), respectively. The installation of Wide Field Camera 3 (WFC3) in 2009 included two infrared grisms[2]), each of which disperse the full $2' \times 2'$ WFC3-IR field of view into low-resolution spectra. The G102 grism has a resolution $R \sim 210$ and covers a wavelength range of $0.8 - 1.15\mu$m while the G141 grism has $R \sim 160$ and covers wavelength range of $1.1 - 1.7\mu$m. Together, the two grisms allow for continuous coverage from $0.8 - 1.7\mu$m.

In Chapter 2, we present the data analysis software we developed for determining emission-line galaxy redshifts and measuring emission-line fluxes in the WISP data. In Chapter 3, we use the rest-frame optical emission-line ratios of the WISP galaxy sample to select a sample of AGN at $0.62 < z < 2.39$. We show that some of the WISP AGN sample are AGN candidates residing in young, low-stellar-mass, dwarf galaxies which may represent extreme outliers from the local M_{bh}-M_* relation. Throughout this work, magnitudes are reported in the AB system (Oke, 1974) and a flat ΛCDM cosmology with $H_0 = 70$ km/s/Mpc and $\Omega_M = 0.3$ is assumed, unless otherwise specified.

[2]The WFC3 UVIS channel also has an ultraviolet/optical grism with resolution $R \sim 70$ and a wavelength range of 1900–4500Å.

CHAPTER 2

The WISP Emission-Line Galaxy Sample

2.1 The WISP Data Products

The WISP Survey has been allocated over 1500 pure-parallel orbits of (*HST*) to obtain imaging and slitless near-infrared (NIR) spectra of tens of thousands of galaxies in the redshift range $z = 0.3$–2.5 (Programs GO 11696, 12283, 12568, 12902, 13352, 13517[1], P.I. Malkan). The pure-parallel observing mode is enabled by the fact that the various cameras of *HST* are distributed in a common focal plane. Thus when one science team is pointing the telescope at a single target for multiple orbits to obtain deep spectroscopy with the Cosmic Origins Spectrograph (COS, Froning & Green, 2009) or the Space Telescope Imaging Spectrograph (STIS, Kimble et al., 1998), WFC3 can collect data simultaneously in an adjacent field. The WISP Survey uses both of the WFC3-IR grisms to obtain spectra of galaxies in uncorrelated, high-galactic-latitude fields. A description of the WISP Survey and first results were presented in Atek et al. (2010).

The WISP Survey has pursued multiple observing strategies over the past five years in order to take advantage of the different opportunities presented by the "prime" COS and STIS programs. The general strategy has been two-pronged: the WISP "deep" survey consists of opportunities with four or more orbits at the

[1]The first four program IDs correspond to Cycles 17–20. In Cycle 21, WISP was the only team awarded pure-parallel orbits. There proved to be an over-abundance of deep parallel opportunities for program 13352, so the WISP team aksed for, and were granted, an additional 200 orbits. For practical reasons, these additional targets were allocated to a second Cycle 21 program, 13517.

same pointing, while the WISP "wide" survey consists of opportunities with three or fewer orbits at the same pointing. In the deep survey, imaging is obtained in the F110W filter and either the F140W or F160W filters, along with spectra in both the G102 and G141 grisms. In the wide survey, imaging is obtained in only the F140W or F160W filter and spectra in only the G141 grism. In both cases, the grism:imaging integration-time ratio is $\sim 6:1$ in order to match the sensitivities in imaging and spectra[2]. In the deep survey, the integration times for the two grisms are balanced in a $\sim 5:2$ ratio (G102:G141) in order to match the sensitivities between the direct and dispersed images. Since Cycle 18 (Program 12283), optical imaging has been obtained in some of the deep survey fields using the WFC3-UVIS channel and the F475X, F600LP, F606W, and F814W filters (see below). Details of all of these filters can be found in Table 2.1. One of my contributions to the WISP effort was implementing the WISP survey strategy by planning exposures in the IR and UVIS for each of the > 1500 orbits we received through Cycle 21.

The amount of time for which the telescope is unocculted and locked onto guide stars (the visibility time) varies for each orbit. Each set of exposures is tailored to match sensitivities between the imaging filters and grism spectra, but also to use as much of the available visibility time as possible. The WFC3-IR data are reduced using a modification to the standard reduction procedures that accounts for the fact that the telescope can not be dithered in pure-parallel observing mode (see Atek et al., 2010; for details). The dispersion solutions of the G102 and G141 grisms are well known and have been incorporated into the software package `aXe` (Kümmel et al., 2009), which is used to extract and calibrate individual spectra from the two-dimensional WFC3 grism images. In order to establish the extraction locations, wavelength solutions, and flux calibrations for `aXe`, direct images are

[2]Exposure times in the WFC3 IR camera are quantized, depending on the sampling options chosen by the observer. Therefore the exposure time ratios reported here are typical, but each WISP field has an idiosyncratic set of exposure times in the imaging and grism frames.

taken of the field on the same orbit as the grism exposures. Source Extractor (SE, Bertin & Arnouts, 1996) is used to obtain the required source positions, sizes, shapes, and magnitudes. The WFC3-UVIS data are reduced following the procedures developed by Rafelski et al. (2015) for the UVUDF.

As can be seen from Table 2.1, the choice of imaging filters changed over the course of the survey. In Cycle 17 (the first cycle after the installation of WFC3; Program 11696), the F140W filter was originally selected in order to set the wavelength and flux scales for objects in the G141 grism images, as it provides the best match in spectral coverage. Once the WISP team received the first data from the WFC3-IR grisms, it became clear that the science goals of the program could be expanded beyond the primary goal of measuring the Star-Formation-Rate Density at $z \sim 1$ using Hα, into projects such as measurements of extreme star-forming dwarf galaxies (Atek et al., 2011, 2014), the Mass-Metallicity Relation (as measured by R_{23}; Henry et al., 2013), dust extinction (as measured Balmer Decrement; Domínguez et al., 2013), and post-starburst galaxies (Bedregal et al., 2013). These additional goals required estimates of stellar mass for the WISP emission-line galaxies. The observing filter set was changed in order to place better constraints on the stellar mass through SED fitting. The F160W filter was then used in place of the F140W filter because the F160W filter does not overlap with the F110W filter, and thus can better constrain stellar population parameters in SED-fitting. The WFC3-UVIS very-broad F475X and F600LP filters were added to some of the deepest WISP targets (in general those with more than 5 orbits) with 2×2 on-chip binning in order to obtain deep optical imaging as quickly as possible. In subsequent cycles, the on-chip binning of WFC3-UVIS imaging was ceased due to poor support of this rarely-used observing mode. Later, the WFC3-UVIS filter set was changed to the F606W and F814W broad filters, because these filters are more commonly used by the community and better supported. In Cycle 19 (Program 12568), none of the available targets could be observed for

more than three orbits, and so the observing program was modified in order to obtain shallow G102 and G141 data in the three-orbit targets with imaging in only the F140W filter. For the one- and two- orbit targets, the observing strategy follows the general strategy of the WISP "wide" survey.

The data output by the reduction pipeline include: direct images, full grism 2-d images, 2-d cutouts of all extracted spectra; 1d flux- and wavelength-calibrated spectra; the Source Extractor catalogs with position, shape, and magnitude measurements for all objects in the images; DS9 regions files for the positions of the SE-extracted stars and galaxies in the direct images, and the `aXe` predictions for the locations of first-order spectra and zero-order images for each extracted object. With fully reduced, extracted, and calibrated spectra output by `aXe`, the analysis of the resulting extracted spectra for their redshifts, line fluxes and other properties remains. The open spectrograph style of the WFC3 grisms makes fully-automated identification of emission lines impossible. Zero-order images and persistence from bright stars and galaxies can mimic emission lines in the extracted spectra of other galaxies. Furthermore, crowding in the field can make it difficult to estimate the continuum level for galaxies whose spectra partially overlap. In principle, the `aXe` software predicts the locations and strengths of these sources of contamination, but in practice the `aXe` estimates are insufficient to fully correct them. Additionally, `aXe` can make no predictions for contamination from sources and galaxies that lie outside of the field of view in the direct images, but whose spectra are dispersed into the field of view in the grism images. Finally, because there can be no dithering in pure-parallel mode, and often only a few exposures per filter or grism image, cosmic ray rejection and chip artifacts can produce features that mimic emission lines in the 1-d spectrum, and need to be rejected as spurious by a review of the 2-d grism image.

2.2 The WISP Data Analysis Pipeline

To overcome the challenges outlined in Section 2.1, I developed a three-stage process in which an automated routine is used to find emission-line "candidates." This step is followed by a by-eye review of these candidates to determine whether each candidate is a real emission line, or an artifact caused by crowding. If the emission-line candidate is deemed "real", then the redshift of the line is estimated and recorded by the reviewer. Finally, the emission lines are measured for each galaxy.

2.2.1 The Automated Emission-Line Candidate Finder

The first stage of the WISP data analysis pipeline is the automatic detection of emission-line "candidates" among the WISP spectra. I developed a custom Python routine to select emission-line candidates. First, the continuum level for each galaxy is estimated using the IRAF[3]/Pyraf *continuum* routine. The continuum is fit in each grism spectrum with a 3-segment cubic spline, including 3-σ outlier rejection, so that the routine does not try to fit emission lines. The continuum is subtracted from the spectrum, and the result is divided by the `aXe` estimate of the spectrum noise to produce a continuum-subtracted signal-to-noise (S/N) spectrum. Each spectrum is scanned for groupings of three or more contiguous pixels above a signal-to-noise of $\sqrt{3}$, such that the minimum total S/N for any emission-line candidate will be $\geq$3. Finally, if the line candidate has an equivalent width (EW) less than 10Å, it is rejected as spurious. This final rejection was motivated by the WISP team's comprehensive completeness tests (Colbert et al., 2013), in which emission lines with equivalent widths less than $\sim$ 30Å (observed frame) are not recovered. This conservative rejection criterion

[3]IRAF is distributed by the National Optical Astronomy Observatories, which are operated by the Association of Universities for Research in Astronomy, Inc., under cooperative agreement with the National Science Foundation.

eliminates spurious emission-line candidates that come from poor continuum fits of the spectra of bright stars.

The number of line candidates produced by this automated selection technique varies from field to field. More line candidates appear in fields where there are more bright stars and in fields for which the grism spectra are deep enough for crowding to become a serious issue. Typically, the number of candidate emission lines found is in the range of $150 - 500$, among which there are $40 - 50$ secure emission lines in $25 - 30$ line-emitting galaxies. The method presented here errs on the side of having the human reviewers examine more emission-line candidates without missing real emission lines that could be detected at $> 3\sigma$ significance. This line candidate detection mechanism prevents the human reviewers from having to look through the hundreds of galaxies in each image whose spectra are smooth and featureless, without contamination by zero-order images or overlap with nearby sources.

2.2.2 Examination of Emission-Line Candidates and Redshift Estimation

The second stage of the WISP data analysis pipeline is the examination of the emission-line candidates produced by the automated line-candidate finder routine. I developed a custom Python routine that is run in the interactive-Python (or iPython) environment, and simultaneously displays a plot of the 1d spectrum, continuum-subtracted S/N spectrum, the 2d spectral stamps, and the direct images for each emission-line candidate. The `aXe` outputs include wavelength-calibrated 2d stamp cutouts of each grism spectrum. The XPA Messaging System[4] (Mandel & Tody, 1995) is used to port commands into a DS9 display window to load each of the direct images and the wavelength-calibrated 2d grism stamps. The `aXe`-produced DS9 regions files are used to display the predicted positions of zero-

[4] `http://hea-www.harvard.edu/RD/xpa/index.html`

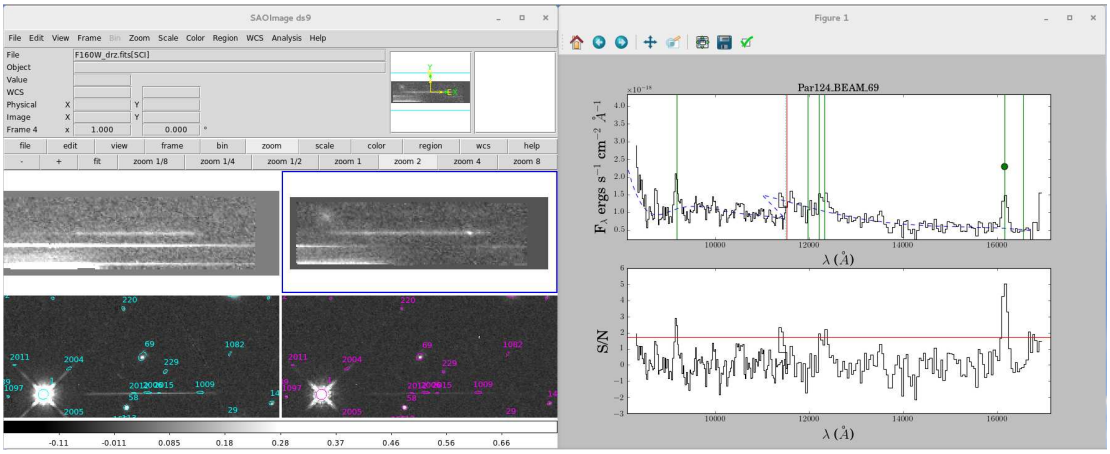

Figure 2.1 Screenshot of the line-candidate-examination software. The left side of the screen shows a DS9 window with wavelength-calibrated Grism cutouts on top and direct images on bottom. The right side of the screen shows the plot of the extracted spectrum (top) and S/N spectrum (bottom). In the extracted 1d spectrum, a green dot marks the current line candidate up for review, assumed by default to be Hα. Vertical green lines mark the expected positions of other strong emission lines if the identification of the candidate as Hα is correct. The blue dashed curve shows the continuum model used in finding the emission-line candidates and the red vertical line marks the division between the two grisms. In the S/N spectrum, the red horizontal line marks the S/N/pix threshold used to select emission-line candidates (i.e. $\sqrt{3}$). This object shows strong Hα and [O II], with weaker [O III] and undetected Hβ and [S II].

order images on the grism stamp cutouts for objects brighter than $H_{140} = 23.0$. The XPA Messaging System is used to pan to the coordinates of each object in the direct images and to load the appropriate DS9 regions files into each frame. The human reviewer can then use all of the available evidence to determine whether each emission-line candidate is a real emission line, or an artifact of crowding in the field. A screenshot of this display method is shown in Figure 2.1.

If the reviewer determines that a given candidate is a real emission line, then they are asked to determine the emission-line species. The reviewer may try several different identifications (Hα, Hβ, [O II], [O III] 4959, [O III] 5007, etc.) for the emission line. The associated redshift is determined based on the line identification and its central wavelength. Vertical lines mark the expected locations of

other strong emission lines, assuming the current guess of the line identification is correct. Frequently, there are multiple significant emission lines in a spectrum, and so the reviewer will match the lines to the most likely identifications that produce the correct separation for these lines. A reviewer may also notice lower-S/N features which were not found by the automatic emission-line candidate finder, which nonetheless may help determine the redshift of the line. When there is only a single emission line found in a spectrum, it is assumed to be Hα, as this is the most common line expected in the WISP survey. The contamination of the WISP Hα-selected galaxy sample by higher-z galaxies due to this default assumption is only $\sim$ 6%, although this leads to an incompleteness of $\sim$ 50% in the WISP [O III]-selected galaxy sample, especially at low S/N (Colbert et al., 2013). Finally, the reviewer has the option of including additional information in the form of adding a flag for possible contamination or a comment explaining their judgment on a particular candidate. There are two optional contamination flags: one if the feature is determined to be a real emission line, but with some contamination in the continuum due to overlap with another source; the other if the feature itself is likely to be caused by contamination and is therefore not likely a real emission line.

The outputs of this routine are a pair of emission-line lists: one with the true emission lines, including redshift estimates and any reviewer comments or contamination flags; the other with rejected line candidates that were worthy of additional commentary by the reviewer. The line candidate examination is time-consuming, and therefore there is an option to continously save the progress in a temporary line list file. If the user must quit before finishing the examination of all candidates in a field, they may later recover their progress from these temporary files.

Each of the WISP emission-line candidates is reviewed by at least two reviewers individually. The lists produced by the two reviewers are then cross-matched

and galaxies are sorted by whether they are included in zero, one, or two of the reviewers' lists. Additionally, if a galaxy is included in both lists, the line measurements are checked against one another to ensure that the galaxy was determined to be at the same redshift and with the same line fluxes and FWHM. When the two reviewers disagree on the redshift of a line, or on whether or not an emission-line candidate is real, they are each asked to take a second look at the line candidate. In the event that the reviewers still disagree after their second look, an additional flag is added to the catalog. This helps to mitigate human error in the review process.

2.2.3 Measurement of Emission-Line Properties

The final stage of the WISP data analysis pipeline is measurement of the emission-line fluxes and widths for each emission-line galaxy. I developed a custom Python routine to fit gaussian line profiles to the emission lines and then obtain fluxes, line widths, equivalent widths, and their uncertainties from the fits. The Scipy least-squares minimization routine, *leastsq*, is used to perform the profile fitting. For isolated lines, a simple gaussian line profile plus linear continuum model is fit to the data. At the resolution of the WFC3 grisms, Hβ is often partially blended with the [O III] doublet, and so the Hβ and [O III] lines are fit simultaneously, under the constraint that they both have the same redshift and line width. The [O III] doublet is nearly always blended, and so is fit as a double-gaussian with amplitudes that form a 3:1 ratio. If the [S II] line is present in the spectrum, it is generally partially blended with Hα, and thus two lines are fit simultaneously, under the constraint that they have the same redshift and line width. The [N II] doublet is fully blended with Hα at the grism resolutions, so no attempt is made to fit for the [N II] lines and the reported Hα fluxes should properly be considered Hα+[N II] fluxes. A screenshot of the line-profile-fitting display is shown in Figure 2.2. Line fluxes, equivalent widths, and line widths are derived from the best-fit model

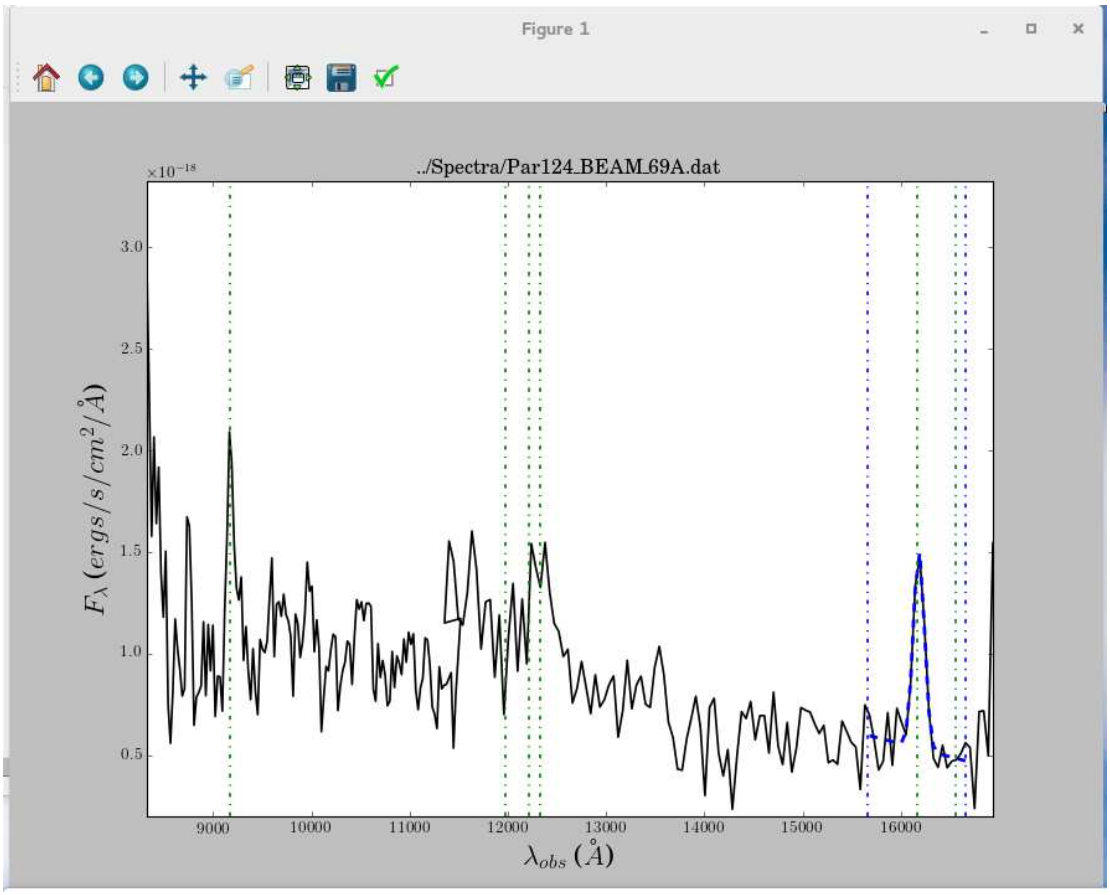

Figure 2.2 Screenshot of the line-profile-fitting display. Vertical green lines mark the expected positions of strong emission lines given the redshift of this galaxy ($z = 1.466$). Blue vertical lines mark the wavelength range of the line profile fit. The blue dashed curve shows the best-fit gaussian line profile for Hα.

parameters. Uncertainties in the fluxes, equivalent widths, and line widths are determined from the covariance matrix of the fit. Note that at the resolutions of the grisms, only lines with widths $\gtrsim$ 2000 km/s are truly resolved, even for a point-like galaxy. For the vast majority of our emission-line galaxies, the measured emission line widths represent the spatial extent of the ionized gas in the galaxy, projected onto the dispersion axis of the spectrograph. The widths measured from our profile fits are used to estimate upper limits for undetected lines in Section 2.2.4 below. The redshift distribution of the WISP emission-line galaxies is shown in Figure 2.3.

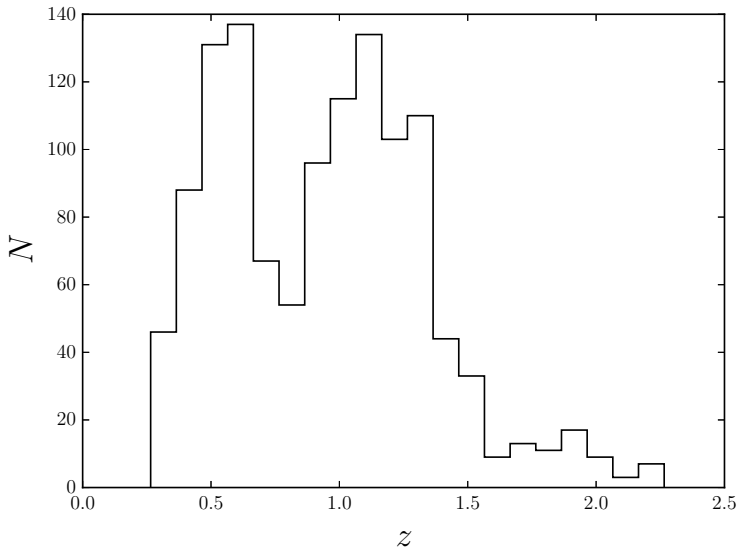

Figure 2.3 Histogram of galaxy redshifts for the WISP emission-line galaxy sample presented here. The local minimum in the number of observed sources at $0.7 \lesssim z \lesssim 0.9$ is caused by the decrease in sensitivity of the G102 grism at $\lambda \gtrsim$11,000 μm and of the G141 grism at $\lambda \lesssim$12,000 μm. At $z \gtrsim 1.4$, Hα is redshifted beyond the coverage of the G141 grism, which causes the dropoff in source counts.

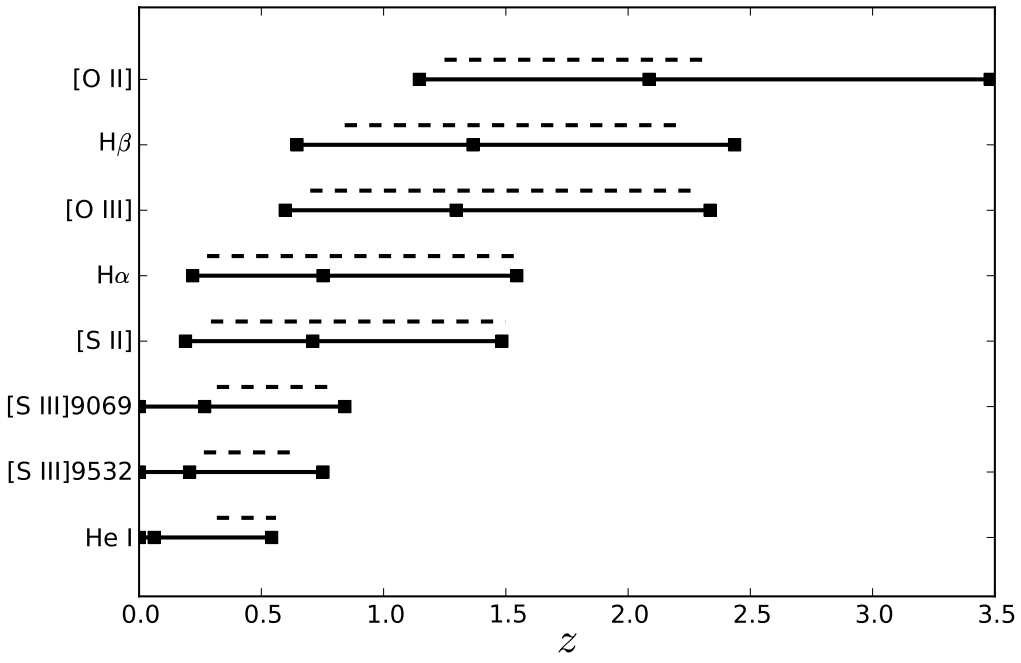

Figure 2.4 Emission-line species detected in the WISP Deep Survey. Solid lines show redshift ranges where the WFC3 grisms are technically sensitive to each particular species, with the square points marking the edges of the wavelength coverages of the two grisms. Dashed lines indicate the redshift range for which each line species was actually detected in the first 29 WISP fields presented in Colbert et al. (2013). Note that the cutoff in detection of [O II] at $z \sim 2.3$ reflects the assumption that single-line emitters are all Hα at $z < 1.55$. In other words, [O II] is likely only to be identified when [O III] and/or Hβ are present in the spectrum.

2.2.4 Detection Limits on Undetected Lines

After line measurements are obtained for the strong lines, upper limits are determined for the undetected emission line species which lie within the wavelength coverage of the grism. The same linear continuum and gaussian line profile models are used as above, with the additional constraints that the redshift and FWHM are fixed to those of the strongest detected line in the spectrum. In the case of Hβ and [S II], the best-fit [O III] and Hα profiles are subtracted, respectively, from the data before the fits are performed.

2.3 The WISP Emission-Line Galaxies Catalog

The WISP team has used the above process to produce emission-line measurements for 1230 galaxies in the 29 fields listed in Table 2.2. I was one of the line-candidate reviewers for each of these 29 fields. The different emission-line species detected in the WISP Deep Survey are shown in Figure 2.4 and Table 2.3. The emission-line measurements are presented in Table A.1, with additional measurements for the rare galaxies with detected [S III] and He I lines presented in Table A.2. In addition to flux measurements, a data quality flag is given for each galaxy using the following scheme: +1 for a disagreement of $> 50\%$ in the flux measurements of the two reviewers, +2 for multiple-line sources where the redshift is confirmed only by a close, S/N<5.0, line (i.e. Hα/[S II] or Hβ/[O III]), +4 for single-line sources, +8 for sources only selected by a single reviewer, +16 for sources with significant redshift disagreements (i.e. one reviewer identifies the line as Hα and one identifies it as [O III]).

2.3.1 Completeness and Contamination

The completeness of the WISP measurements produced by this method were examined in Colbert et al. (2013; Section 3.1), but will be summarized here. A series of 973 model galaxies were generated spanning the redshift range $z = 0.3$–2, magnitude range 19–26 (in F110W), spatial extent ranging 0.2″–1″in radius, and equivalent widths ranging from 13–3000Å in the observed frame. The software `aXeSIM` (Kuemmel et al., 2007) was used to add these model galaxies into the actual WISP data frames. They were then extracted and processed following the same procedures as the real WISP data, including the redshift-estimation and line-measurement processes. I was one of the two reviewers for each of these simulation fields. Colbert et al. (2013) demonstrated that the completeness for Hα ranges from about 50% to nearly 100% as line-flux S/N and EW increase from marginal (S/N$\sim$ 3, EW$\sim$ 40Å) to strong. In addition, the contamination rates for Hα were found to be 8.5% from false emission-lines (detector artifacts and missed cosmic rays, unmitigated due to lack of dithering) and 5.8% from misidentification of [O III] as Hα, for a total contamination rate of 14.3%. While the contamination of the WISP Hα sample due to misidentification of [O III] is only 5.8%, this misidentification leads to a significant additional source of incompleteness of order 50% in the WISP [O III] sample at $z > 1.5$. We reproduce the completeness estimates from Figure 4 of Colbert et al. (2013) in Table 2.4.

2.4 Discussion and Conclusions

2.4.1 Comparison With the WFC3 Exposure Time Calculator

The Space Telescope Science Institute (STScI) provides an online Exposure Time Calculator (ETC) for WFC3[5]. This utility can provide a signal-to-noise-per-pixel

[5] `http://etc.stsci.edu/etc/input/wfc3ir/spectroscopic/`

prediction for a pixel at a given wavelength, under various assumptions about a source spatial profile, spectrum, and strength of the sky background from zodiacal light and Earthshine (including a time-variable contribution from geocoronal He I 10830Å line emission that effects the G102 more strongly than the G141 grism, see Brammer et al., 2014). The distribution of the WISP fields all over the sky leads to a large variation in background levels and therefore a broad range in line sensitivity (see Figure 2.5). For simplicity, therefore, the median WISP line sensitivity is compared against the ETC predictions under the following assumptions:

1. The spatial profile is a point source. The typical WISP line emitter is barely resolved, so this is a reasonable approximation.

2. The spatial extraction of the spectrum is 3×1 pixels.

3. Average zodiacal and Earthshine backgrounds are assumed. The Helium line emission background is neglected.

4. The emission line profile is assumed to be Gaussian with a FWHM of 2 pixels.

5. The exposure times are assumed to be 6750s in the G102, distributed between seven exposures, and 2700s in the G141, distributed between four filters.

6. The source spectrum is assumed to be flat in $F_\lambda = 1.0 \times 10^{-18}$ erg/s/cm^2/Å.

The ETC returns a S/N/pixel for a given wavelength. This is converted to a line flux uncertainty in the following manner: assuming the flux-density of the pixel is the peak flux density of the Gaussian line profile, the total flux of the line will be $\sqrt{2\pi}\,\sigma_{\rm line}\,\delta\lambda\,F_{\lambda,\rm peak}$, where $\sigma_{\rm line} = 2/2.35$ pixels is assumed (as above), $\delta\lambda$ is 24.5Å/pixel (46Å/pixel) in the G102 (G141) grism, and $F_{\lambda,\rm peak} = 1.0 \times$

10^{-18} erg/s/cm^2/Å as input in the ETC calculation. In other words, a line with the assumed profile and a peak flux density of $F_{\lambda,\mathrm{peak}} = 1.0 \times 10^{-18}$ erg/s/cm^2/Å corresponds to a total line flux of 5.22×10^{-17} erg/s/cm^2 in the G102 and 9.80×10^{-17} erg/s/cm^2 in the G141. This assumed 'signal' is then divided by the ETC S/N estimate to produce a 1-pixel noise prediction for the line flux. Assuming all of the line flux is contained in 4 spectral pixels ($N_{\mathrm{pix,line}} = 4$; a good approximation for the assumed line profile), this 1-pixel noise prediction is multiplied by $\sqrt{4} = 2$ to approximate the total flux uncertainty of an emission line. To summarize, the 5σ limits shown in Figure 2.5 are calculated from the ETC estimations as:

$$5\sigma \text{ Line flux limit}(\lambda) = \frac{5 \times \sqrt{N_{\mathrm{pix,line}}} \times \sqrt{2\pi}\, \sigma_{\mathrm{line}}\, \delta\lambda\, F_{\lambda,\mathrm{peak}}}{[\mathrm{S/N}]_{\mathrm{ETC},\lambda}}. \tag{2.1}$$

The median WISP line sensitivities are calculated as follows: The line uncertainties derived from the line profile fitting procedure described in §2.2.3 and upper limits described in §2.2.4 are assumed and scaled to a common exposure time by $\sqrt{t_{\mathrm{nominal}}/t}$ where t_{nominal} matches the integration times assumed in the ETC calculations above (6750s in G102 and 2700s in G141) and t is the actual integration time for the spectrum in which the line was found. The scaled line uncertainties and upper limits are binned in wavelength with bin sizes of 0.02μm, and the median is taken for each bin. Figure 2.5 shows that the median line flux limits derived from the WISP line profile fits are broadly consistent with the ETC predictions for a field with average zodiacal and Earthshine backgrounds, with the primary disagreement occurring at the ends of each grism. These discrepancies are most likely accounted for by the steep dropoff in sensitivity of the grisms at each end of the spectrum, which both reduces the number of WISP measurements in those bins and makes the sensitivity vary strongly across the bin. The 25th and 75th percentiles for each bin are plotted as well. The broader tail to lower sensitivity (greater flux limit) at all wavelengths is most likely due to increased

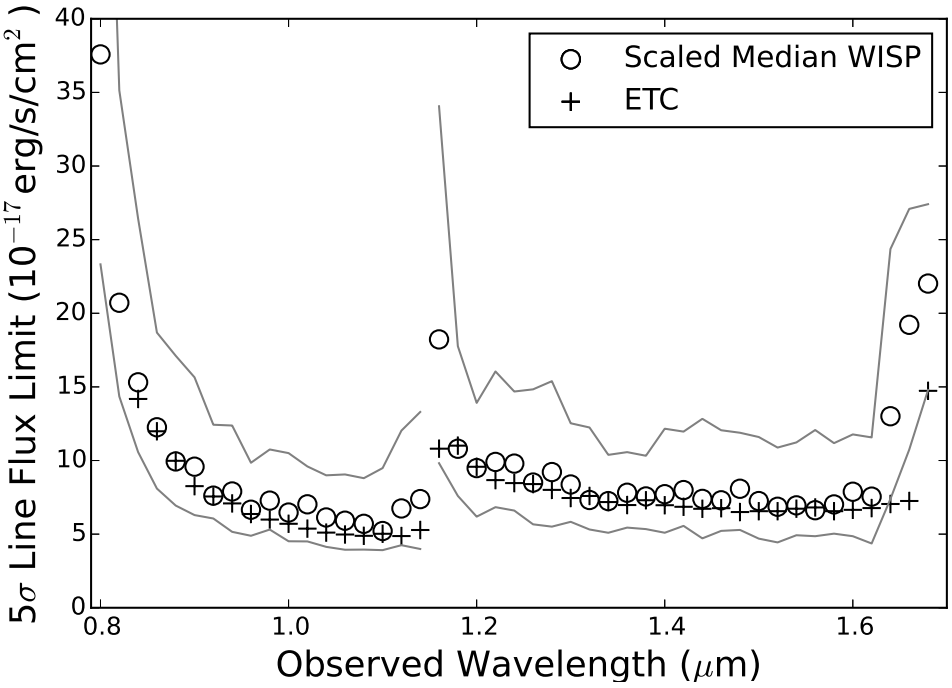

Figure 2.5 Median 5σ emission-line sensitivities for a nominal WISP field as a function of wavelength in the WISP data compared to the sensitivities predicted by the WFC3 online Exposure Time Calculator (ETC). The grey lines denote the 25th and 75th percentiles of the WISP data.

local noise from crowding and the tendency for the global noise to increase due to the time-varying Helium line emission described in Brammer et al. (2014).

2.4.2 Summary

I have presented here the method I developed for the extraction and measurement of emission-line galaxies from *HST* slitless grism spectroscopy. A fully automated emission-line detection algorithm is impossible due to contaminating sources such as zero-order images and persisitence. Instead, I developed an automated line-candidate search algorithm followed by a human review of each candidate line. The human reviewers examine both the 1-d and 2-d grism spectra, along with the direct images, to determine if a candidate is a real emission line. The reviewers

also determine the redshift of the line and use a profile fitting routine to measure the emission-line flux, FWHM, and EW. All line candidates are examined by at least two reviewers whose line lists are cross-matched. The two reviewers then re-examine any objects for which there was disagreement. The final line lists produced by this method have line flux detection limits consistent with the predictions of the online Exposure Time Calculator. These data have been used to make predictions for the planned WFIRST and Euclid surveys in Colbert et al. (2013) and Mehta et al. (2015), to measure dust extinctions in Domínguez et al. (2013), and to select a sample for stacking galaxies to measure the average Mass-Metallicity relation in Henry et al. (2013). These data will be used to measure the Hα luminosity function at $0.3 < z < 1.5$ (Bunker et al., in prep) and the Seyfert galaxy population at $z > 0.62$.

Table 2.1. Filters Used by the WISP Survey

Filter	Channel	Pivot Wavelength (Å)	FWHM (Å)
F475X[a]	UVIS	4939	2056
F600LP[a]	UVIS	7444	2292
F606W[b]	UVIS	5887	2182
F814W[b]	UVIS	8024	1536
F110W	IR	11534	4430
F140W[c]	IR	13923	3840
F160W[d]	IR	15369	2683
G102	IR		8000-11500
G141	IR		10750-17000

[a]Programs 11696, 12283

[b]Programs 12283, 12902, 13352, 13517

[c]Programs 11696, 12568

[d]Programs 11696,12283, 12902, 13352, 13517

Note. — Data obtained from the WFC3 Instrument Handbook. `http://www.stsci.edu/hst/wfc3/ins_performance/filters/`

Table 2.2. Summary of WISP Survey Fields

Field ID	Date Observed	RA [H:M:S]	Dec [D:M:S]	F110W [Sec]	G102 [Sec]	F160W [Sec]	G141 [Sec]	F475X [Sec]	F600LP [Sec]	Program ID
17	2010/02/18	02:13:38.11	+12:54:59.3	534	3409	559[a]	3409	0	0	11696
55	2010/07/22	12:20:54.68	−02:04:46.0	909	6415	484[a]	2809	0	0	11696
62	2010/08/12	13:01:16.20	−00:00:20.2	734	4712	396[a]	2006	0	0	11696
64	2010/08/18	14:37:29.04	−01:49:49.5	1112	5918	456	2306	400	400	11696
68	2010/10/14	23:33:33.04	+39:21:20.5	1215	7721	534	3009	400	400	11696
69	2010/09/12	15:24:07.75	+09:54:53.9	1087	5721	431	2309	400	400	11696
73	2010/10/01	14:05:12.86	+46:59:19.9	1034	6118	456	2509	400	400	11696
74	2010/10/03	09:10:48.14	+10:17:20.3	1065	5918	431	2306	400	400	11696
76	2010/10/08	13:27:22.17	+44:30:39.3	887	5515	406	2006	400	400	12283
78	2010/10/17	23:28:34.06	+05:10:28.3	887	5318	406	2106	0	0	12283
79	2010/11/08	01:10:08.96	−02:25:16.2	1187	7521	534	2809	400	400	11696
81	2010/11/19	01:10:09.12	−02:22:17.1	1187	7521	534	2809	400	400	11696
87	2010/12/04	09:46:46.39	+47:14:58.2	912	4915	406	1906	400	400	12283
94	2010/12/24	22:05:26.66	−00:17:48.5	1624	9024	534	3309	400	400	12283
96	2011/01/06	02:09:24.40	−04:43:41.6	4295	28081	1765	11430	3000[b]	3000[b]	
97	2011/01/16	01:10:06.30	−02:23:44.7	859	5515	406	2109	400	400	11696
114	2011/05/27	10:40:58.09	+06:07:31.0	1137	7221	456	2909	600[c]	600[c]	12283
115	2011/05/28	11:18:55.08	+02:17:09.6	912	5215	381	2106	600[c]	600[c]	12283
120	2011/06/10	13:56:51.50	+17:02:33.9	837	4512	381	1806	600[c]	600[c]	12283
124	2011/06/21	18:32:28.28	+53:44:50.9	759	4618	406	1906	0	0	12283
129	2011/06/30	11:02:18.72	+20:52:07.8	762	4712	456	2206	0	0	12283
131	2011/07/02	10:48:22.94	+13:03:50.5	2171	13039	884	5215	600	600[c]	12283
132	2011/07/03	11:26:19.80	−01:43:22.1	634	4315	356	1806	0	0	12283
135	2011/07/15	11:22:24.01	+57:50:58.9	862	4712	406	1906	600[c]	600[c]	12283
136	2011/07/16	12:26:28.84	+05:23:02.9	3036	18857	1137	7318	2000[b,c]	2000[b,c]	12283
143	2011/08/06	14:02:22.01	+09:45:51.7	1568	10133	759	4012	600[c]	600[c]	12283
146	2011/08/21	02:12:27.60	−07:32:20.7	887	4212	381	1706	600[c]	600[c]	12283
147	2011/08/23	23:58:19.51	−10:15:04.6	962	5418	406	2106	600[c]	600[c]	12283
167	2011/11/07	01:41:24.18	+13:37:34.1	659	4315	356	1806	0	0	12283

[a]H-band imaging for these fields is in the F140W.

[b]UVIS imaging for these fields is in F606W and F814W.

[c]UVIS exposures obtained using the on-chip 2×2 binning mode.

Note. — A summary of the observations performed under the HST programs GO/PAR 11696 and 12283 for the WISP Survey included in this release.

Table 2.3. WISP Emission-line Counts

Emission-line Species	Number of lines
[O II] $3726 + 3729$Å	80
Hβ	46
[O III] $4959 + 5007$Å	262
Hα	1164
[S II] $6717 + 6731$Å	118
[S III] 9069Å	13
[S III] 9532Å	27
He I 10830Å	4

Note. — Number of emission lines detected at more than 3σ significance using the methods described in §2.2

Table 2.4. Completeness Estimates for the WISP Emission-Line Galaxy Catalog

	log(S/N)			
log(EW)	1.0	1.6	2.2	2.8
3.35	···	$0.75^{+0.25}_{-0.25}$	$0.90^{+0.10}_{-0.30}$	···
2.85	$0.60^{+0.14}_{-0.14}$	$0.73^{+0.12}_{-0.12}$	$0.85^{+0.15}_{-0.17}$	$1.00^{+0.00}_{-0.35}$
2.35	$0.51^{+0.11}_{-0.11}$	$0.79^{+0.10}_{-0.10}$	$0.86^{+0.14}_{-0.20}$	···
1.85	$0.57^{+0.09}_{-0.09}$	$0.71^{+0.11}_{-0.11}$	$0.95^{+0.05}_{-0.31}$	···

Note. — Estimated completeness as a function of log(EW) and log(S/N) for the WISP emission-line catalog, as described in Colbert et al. (2013).

CHAPTER 3

The WISP AGN

3.1 Introduction

Large spectroscopic samples of Active Galactic Nuclei (AGN) have been assembled at $z < 0.5$, which have allowed us to investigate the growth of supermassive black holes in the local universe. At higher-z, the brightest AGN (quasars) are detectable by their strong rest-frame ultraviolet (UV) and X-ray emission. But at $z \gtrsim 1$, the X-ray fluxes of more moderate AGN become low enough that even the extremely deep, narrow, surveys (CDFS, CDFN, XMM-COSMOS, Giacconi et al., 2002; Alexander et al., 2003; Hasinger et al., 2007) become incomplete (e.g. Trump et al., 2009). Note that current X-ray space telescope missions potentially will be coming to an end before the next generation telescopes are launched. In contrast, the sensitivity of ground-based IR instruments has grown rapidly over the last decade. In the near future, the best methods for studying AGN during the peak of cosmic black hole growth will be in the rest-frame optical and infrared with ground-based telescopes and JWST. However, selection of AGN by their optical emission-line properties at $z \gtrsim 1$ becomes challenging due to the expected lower black hole masses – which are less luminous than massive BH at fixed Eddington ratio – and decreased contrast between the accreting nucleus and star-forming regions in the host galaxy (e.g. Coil et al., 2015; Trump et al., 2015). In this chapter, I use the WISP emission-line galaxy sample to select AGN using a variety of methods calibrated in local galaxy populations. My sample is likely to suffer from incompleteness, but I take care to select an AGN sample that is

pure and examine to properties of these rest-frame-optically-selected AGN.

3.2 Data

Here I will use the emission-line catalogs described in Chapter 2, along with data from an additional 23 WISP fields, to select line-emitting galaxies in the redshift range $0.625 < z < 2.395$, in which the [O III] and Hβ lines can be measured. I further require that the quality flag (see Section 2.3) for the emission-line measurements be less than 16, following Colbert et al. (2013). This eliminates galaxies for which the two reviewers could not agree on a redshift. These selection criteria leave us with a total sample of 1865 line-emitter galaxies. Next, I require that [O III] be detected at greater than 3σ significance. This reduces my sample to 668 galaxies.

3.2.1 HST

All of the WISP fields used here have coverage by both of the WFC3/IR grisms, G102 and G141, providing continuous spectral coverage from 0.8–1.7μm. In addition, all fields are covered with imaging in the F110W (broad J) and either the F140W (broad H) or F160W (H) filters. These two direct images are necessary for the extraction and calibration of the grism spectra. Starting at the end of Cycle 17, additional optical images were obtained for those fields with enough available visibility time to allow additional WFC3/UVIS exposures to be taken without sacrificing significant depth in the grism spectra. I list the photometric filters used in Table 3.1. The WFC3/IR imaging and grism data were reduced and the individual spectra extracted following Atek et al. (2010). The WFC3/UVIS imaging data were reduced following the procedures used for the UVUDF (Rafelski et al., 2015).

3.2.2 Spitzer

Each of these fields, excepting WISP319, was also observed in the *Spitzer Space Telescope*/IRAC 3.6μm channel (hereafter referred to as Channel 1). In addition, fields WISP79 and WISP120 were observed in the *Spitzer Space Telescope*/IRAC 4.5μm channel (hereafter referred to as Channel 2). These data were reduced following the pipeline for the *Spitzer* Enhanced Imaging Products program, as outlined in Teplitz et al. (2010). We matched our emission-line galaxies to the *Spitzer* catalogs with a radius of tolerance of 1.5″.

3.2.3 Ground-Based Optical Imaging

We obtained *g*- and *i*-band imaging of fields WISP17 and WISP132 with the Large Format Camera (LFC) on the Palomar Observatory Hale 200-inch telescope (see Table 3.2). We also obtained *g*-band imaging of fields WISP288, WISP291, WISP295, WISP297, WISP308 and WISP311 from LFC to complement our WFC3/UVIS F814W imaging. Typical limiting magnitudes are 26.5 in the *g*-band and 25.7 in the *i*-band. The Palomar images were reduced using standard procedures. The images were registered to the World Coordinate System (WCS) using the Astrometry.net software package (Lang et al., 2010). Photometric calibration was performed by matching sources in the Palomar imaging to SDSS sources with S/N$\geq$ 10 in both the *g*- and *i*-bands. Photometric zeropoints were calculated for both bands (where available) including a color term to correct for the different sensitivities of the Palomar and SDSS optical systems as a function of wavelength. Photometric catalogs were produced by running Source Extractor (hereafter SE; Bertin & Arnouts, 1996) in dual-image mode. The *i*-band image is used for detection and a 5-pixel minimum area above a detection threshold of 2.2σ is required for detection and extraction of sources. The resulting catalogs are matched to WISP sources with a radius of tolerance of 0″.75.

We obtained WIYN *g*- and *i*-band imaging of fields WISP64 and WISP74, along with *i*-band imaging of field WISP87, with the *MiniMosaic* camera on the WIYN 3.5-m telescope at Kitt Peak National Observatory. The images were registered to the WCS using bright SDSS sources. The images were then photometrically calibrated using SDSS stars between 15th and 21st magnitude in each filter. We use SE to obtain photometric catalogs in single-image mode. Detection criteria are a 7-pixel minimum area above a detection threshold of 2.2σ. The resulting catalogs are matched to WISP sources with a radius of tolerance of $1''$. Observation logs for the Palomar and WIYN imaging are shown in Table 3.2.

3.2.4 HST Photometry

For the WFC3 images, I use the Source Extractor (SE) WCS positions, elliptical rms major/minor axis lengths, and position angles extracted from the F110W catalogs from our reduction pipeline as a reference for aperture photometry. I use the Python *photutil* package to perform aperture photometry with an elliptical aperture size of $4\times$ the rms profile from the catalog. This aperture size produces the best match between the aperture photometry and the SE photometry in our IR catalogs. The same aperture parameters (in WCS) are used on the WFC3/UVIS images. Background and uncertainty estimates for each WISP source are derived by placing 2000 random apertures on the sky and calculating the mean and standard deviation, with outlier rejection. I apply a nebular emission correction to the WFC3/IR photometry using the line fluxes measured in Chapter 2.

3.3 Analysis

3.3.1 Stellar masses

I use Fitting and Assessment of Synthetic Templates (FAST) code from Kriek et al. (2009) to determine stellar masses for all [O III]emitters in the sample. A grid of stellar populations from the Conroy et al. (2009) libraries was used with delayed-exponentially declining star formation histories, a range of ages, metallicities, and extinctions (assuming the dust attenuation law of Kriek & Conroy, 2013). The parameters used by FAST are summarized in Table 3.3. I made no prior attempt to remove AGN from the sample for which I estimate stellar masses with FAST. Note that Type 1 AGN, with their bright non-stellar continua and blue UV continuum slopes, would therefore have overestimated stellar masses and underestimated stellar population ages. For Type 2 AGN, the optical–UV continuum is dominated by starlight, and at the redshifts considered here ($0.625 \lesssim z \lesssim 2.395$) our 3.6$\mu$m imaging covers the rest-frame 1.06μm–2.22μm, where the nuclear hot dust emission begins to contribute significantly to the total light of the galaxy. Therefore, I expect the AGN emission to produce an overestimate of the stellar masses for Type 2 AGN. However, as I am primarily using the stellar mass estimates to select AGN using the MEx method (Juneau et al., 2014), any overestimate of the stellar mass in AGN hosts due to AGN continuum contributions will only tend to increase my probability of identifying true AGN in my sample[1].

3.3.2 Correction for underlying Balmer absorption

I use the best-fit output spectra from the FAST stellar population fits to calculate a correction to the Balmer line fluxes for underlying stellar absorption. For each emitter in our sample, I fit and subtract a linear continuum from the stellar population sythesis model in the rest-frame wavelength ranges $4790 - 4820$Å and

[1]For the MEx selection method, $P(AGN|M_*, [\text{O III}]/\text{H}\beta)$ increases with M_*.

4910 − 4940Å. I then fit a Lorentzian profile to the continuum-subtracted Hβ absorption line. I add the flux of the line to the WISP Hβ measurements. As noted in Chapter 2 and in Colbert et al. (2013), the WISP sample becomes incomplete for equivalent widths $EW \lesssim 30$Å in the observed frame, corresponding to rest-frame equivalent widths of $EW \sim 9-18$ over the redshift range $z = 0.625-2.395$ of my sample. Therefore, these corrections to Hβ are generally minor when compared to our measured [O III] fluxes (median 2.4%). Note, however that a large fraction of our [O III] emitters have no detected Hβ emission in the WISP emission-line catalogs, and so the correction for stellar absorption can make up as much as 100% of our Hβ fluxes for many galaxies. In these cases, the correction for Balmer absorption is generally found to be within the upper limits for detection of Hβ and so I continue to treat them as upper limits. I likewise correct the Hα measurements for underlying stellar absorption. The continuum range for which I fit the Hα linear continuum model is rest-frame 6490 − 6510Å and 6610 − 6640Å. The correction to the Hα line is generally less than 5%.

3.3.3 AGN Selection

Here I rely on emission-line-ratio diagnostics to separate galaxies with emission lines consistent with ionization by hot young stars and those with emission-line strengths that indicate ionization by the harder UV ionizing continuum of an AGN. All of the diagnostics rely directly on the [O III]/Hβ ratio. For gas that is photoionized by hot young stars, this ratio is primarily sensitive to the oxygen abundance (often used as a proxy for the total metallicity) of the gas: the forbidden-line emission of heavy elements is a primary source of cooling for a hot plasma, so as the metal abundance increases, the characteristic temperature of the plasma decreases. Because the [O III] doublet is collisionally-excited, the decrease in temperature with increasing metallicity decreases the intensity of the line. But even for the hottest stars seen in the local universe, the steep decline of the ioniz-

ing continuum at high photon energies limits the [O III]/Hβ ratio[2] to $\lesssim 8-9$. The observed power-law continuum emission from the accretion disk around a SMBH can produce a much harder ionizing continuum and so it can produce much higher [O III]/Hβ ratios, even when the plasma has high metallicity and therefore more efficient cooling.

In the WISP [O III] emission-line galaxy sample, 55% of the [O III] emitters are undetected in Hβ. Nevertheless, for high-S/N detections of [O III], we can infer a diagnostically valuable lower limit on the [O III]/Hβ ratio in the following manner. For Hβ non-detections, I assume that the most probable 'true' value for the Hβ flux is just at the noise level and therefore assign Hβ a flux equal to its 1-σ upper limit. I then treat these objects as though they were simply low-S/N detections. I choose the 1-σ (as opposed to 3-*sigma*) uncertainty limit as the nominal value for Hβ non-detections primarily because the WISP emission-line catalogs include Hβ measurements even below the 2-σ when [O III] is detected at $>$ 3-σ. The corresponding uncertainty in the inferred log([O III]/Hβ) for the Hβ non-detections will be large ($> 1/\log(10) \simeq 0.434$).

For each of the diagnostics considered below, I adopt a conservative selection criterion whereby only those objects for which 95% of their uncertainty ellipses[3] lie above our selection threshold are added to the AGN sample. Therefore, I am confident that the adoption of Hβ upper limits as 1-σ detections, which will be accompanied by large uncertainty in [O III]/Hβ, will not significantly contaminate the AGN sample with low-S/N star-forming galaxies. Put another way, when Hβ is undetected, but [O III] is detected at high S/N, we can infer a stringent lower limit on [O III]/Hβ that will allow us to confidently rule out ionization by hot, massive

[2]I examine the possibility that extremely-metal-poor stars in very young galaxies at $z \sim 1-2$ produce a harder ionizing spectrum than stars in the local universe in the discussion (Section 3.4.1) below.

[3]For 2-parameter AGN selection criteria, there is generally a curve separating the parameter space. Therefore one must consider the uncertainites in both parameters. In 2-parameter space, the iso-uncertainty curves for a pair of parameter estimates will then form an ellipse.

stars. The requirement that 95% of the uncertainty ellipse lie within the selection region for each of the diagnostics will necessarily lead to some incompleteness, especially for low-S/N [O III] detections and low luminosities, but should result in a very (i.e. $> 95\%$) pure AGN sample.

3.3.3.1 Modified-BPT Diagram

In the "classic" Baldwin, Phillips, and Terlevich (hereafter BPT; Baldwin et al., 1981) diagram, the [O III]/Hβ and [N II]/Hα ratios are used to distinguish star-forming galaxies from AGN. As discussed above, the [O III]/Hβ ratio for star-forming galaxies decreases with gas-phase metallicity. The [N II]/Hα ratio, however, increases with metallicity: the first ionization potential for nitrogen is 14.5 eV, just above the ionization potential for hydrogen (13.6 eV), and so as nitrogen abundance increases, the [N II]/Hα ratio increases. A similar behavior is seen in the [S II]/Hα ratio (see, e.g. Veilleux & Osterbrock, 1987; Kewley et al., 2001, 2006)[4]. At the resolution of the WFC3 grisms ($R = 140 - 200$), we are unable to resolve [N II] from Hα, but we can resolve [S II] from the Hα+[N II] blend. I therefore combine equations 4 and 7 from Kewley et al. (2006) to produce an AGN selection criterion for a [O III]/Hβ vs. [S II]/(Hα+[N II]) modified-BPT diagram (Figure 3.1).

There is mounting evidence that galaxies at $z > 1$ may have higher nitrogen abundances (relative to oxygen) compared to galaxies in the local universe, which causes an observed offset in the "classical" BPT diagram to higher [N II]/Hα ratios at fixed [O III]/Hβ, but no such offset in the [S II]/Hα ratio (e.g. Masters et al., 2014; Shapley et al., 2015). I do not adjust my selection criterion to account for this increase in [N II]/Hα, which may lead to a small additional source of incompleteness in the AGN sample, but with an accompanied small increase in sample purity. An example of a modified-BPT-selected AGN can be found in

[4]The first ionization potential for sulfur is 10.4 eV.

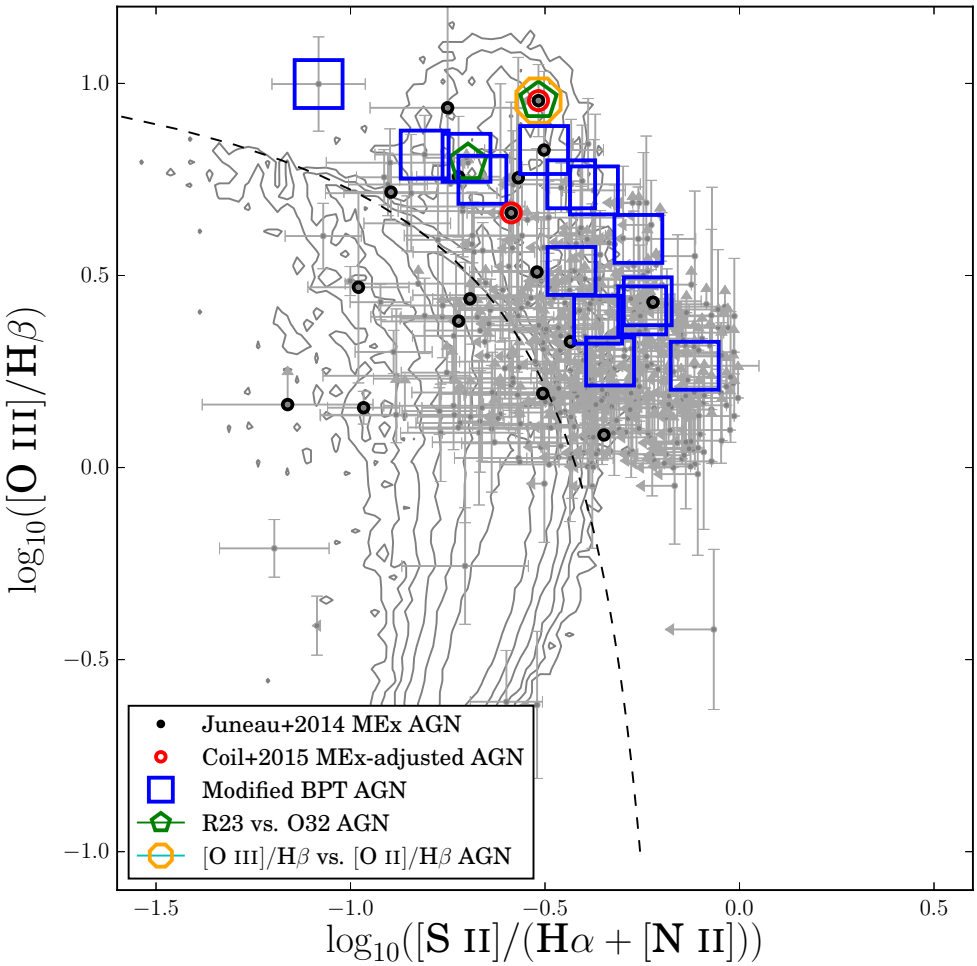

Figure 3.1 The modified BPT diagram shows one of the methods for selecting AGN from the WISP survey. Grey contours are galaxies from SDSS. The black dashed line shows our AGN selection criterion adapted from Kewley et al. (2006).

Figure 3.2

3.3.3.2 MEx Selection

The strong observed correlation between the mass of stars in a galaxy and gas-phase metallicity (e.g. Tremonti et al., 2004; Mannucci et al., 2010; Henry et al.,

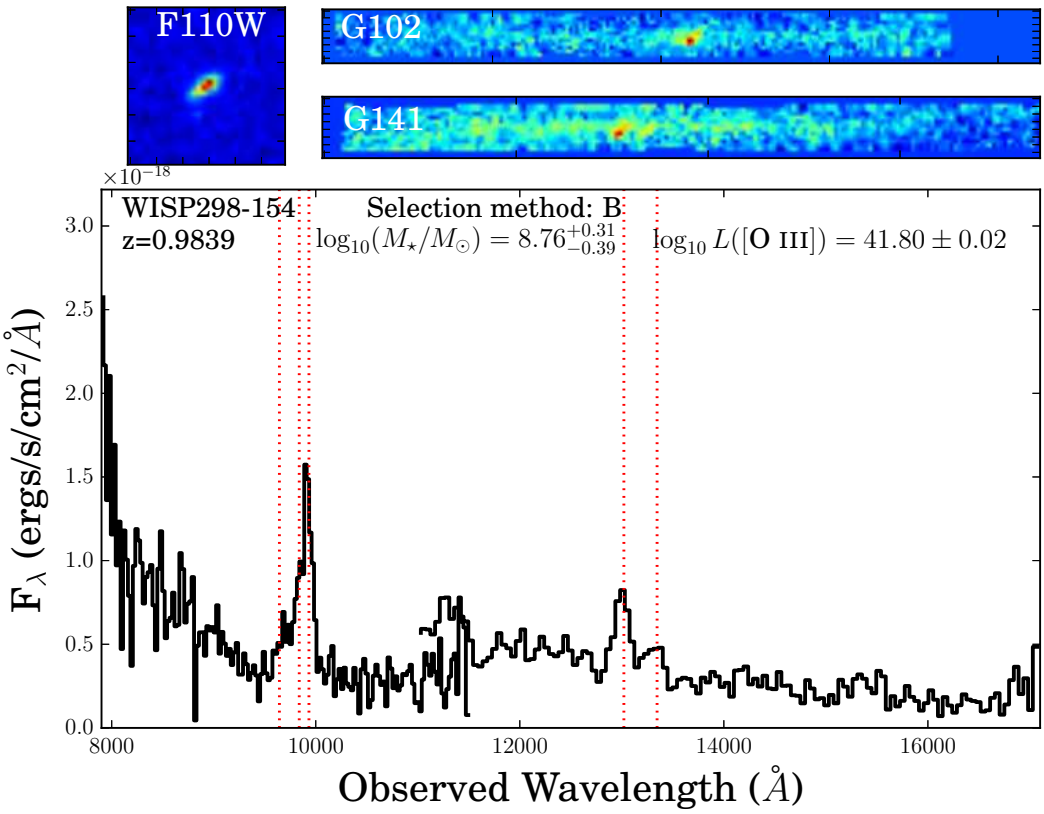

Figure 3.2 Here we show the J_{110} image, 2-d grism spectra and 1-d extracted spectrum for a galaxy selected as an AGN by our modified-BPT selection criterion. Vertical red lines mark (from left to right) the positions of Hβ, the [O III] doublet, Hα and [S II].

2013; Andrews & Martini, 2013; Maier et al., 2014; Zahid et al., 2014; Sanders et al., 2015; Ly et al., 2015) means that stellar mass can be used to infer a metal abundance (and therefore low-ionization line strength) for a galaxy. Juneau et al. (2011) introduced the Mass-Excitation selection which uses stellar mass as a proxy for [N II]/Hα to select AGN based on the [O III]/Hβ ratio. This selection technique was updated by Juneau et al. (2014) to account for the evolution of the mass-metallicity relationship over cosmic time and biases due to survey line flux limits. Note, however, that Coil et al. (2015) found that the Juneau et al. (2014) method, when applied at $z \sim 2.3$, tends to produce an AGN sample highly contaminated by star-forming galaxies when compared with the "classical" BPT diagram. Following Coil et al. (2015), I also select AGN by applying a simple offset of 0.75 dex in stellar mass to the Juneau et al. (2014) MEx selection diagram. This offset may be an overestimate for my sample because it is at a lower redshift than the Coil et al. (2015) sample. Nonetheless, it should provide a more conservative comparison to the Juneau et al. (2014) selection criteria. I note here that Juneau et al. (2014) have provided an IDL routine that returns a probability that the ionization characteristics of the gas are representative of star-forming regions, AGN, Low-Ionization Nuclear Emission Regions (LINERs, with emission-line features characteristic of shock-induced heating Heckman, 1980), or "Composite" sources, which represent a mixture of AGN activity and ongoing host-galaxy star formation. In using the probabilistic approach of Juneau et al. (2014), I adopt as my AGN selection criterion $P(SF) < 0.05$. An example spectrum of a galaxy selected by this criterion is shown in Figure 3.4.

3.3.3.3 Selection with OII

Two selection methods using [O II], [O III], and Hβ may be used to select AGN based on the high ionization ratios generated by the AGN ionizing spectrum. The first compares the [O II]/Hβ ratio to the [O III]/Hβ ratio (Figure 3.5) and the

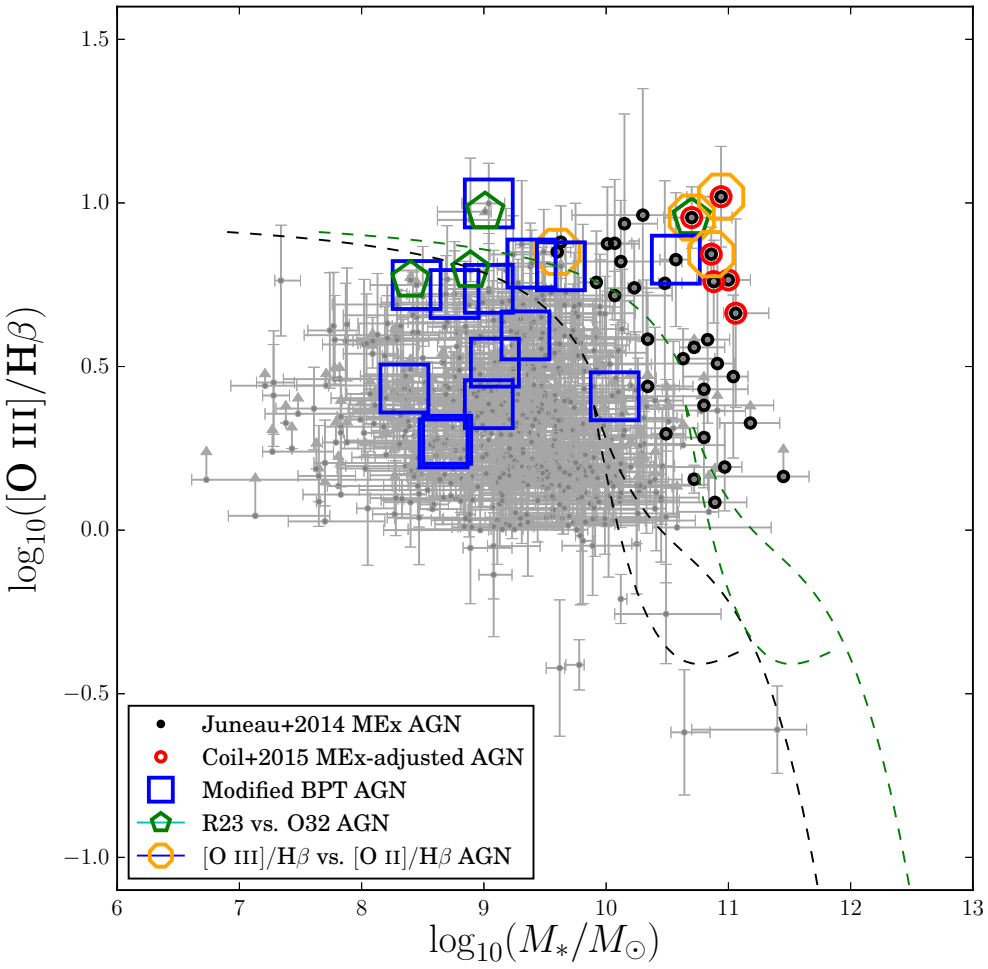

Figure 3.3 The Mass-Excitation (MEx) diagram of Juneau et al. (2014) is used to select AGN from the WISP survey. The black dashed lines show the AGN/'transition'/SF selection criteria of Juneau et al. (2011) for illustrative purposes, but in this paper, we use the updated, probabilistic approach of Juneau et al. (2014). Additionally, we consider the modification (green dashed line) to the Juneau et al. (2011) criteria recommended by Coil et al. (2015) for galaxies at $z \sim 2$, which is a simple offset of 0.75 dex to higher stellar mass.

second uses the parameters R_{23} and O_{32} (Figure 3.6), defined by:

$$R_{23} \equiv \log_{10}\left(\frac{[\mathrm{O\ II}]\lambda\lambda 3726, 3729 + [\mathrm{O\ III}]\lambda\lambda 4959, 5007}{\mathrm{H}\beta}\right) \quad \text{and} \quad (3.1)$$

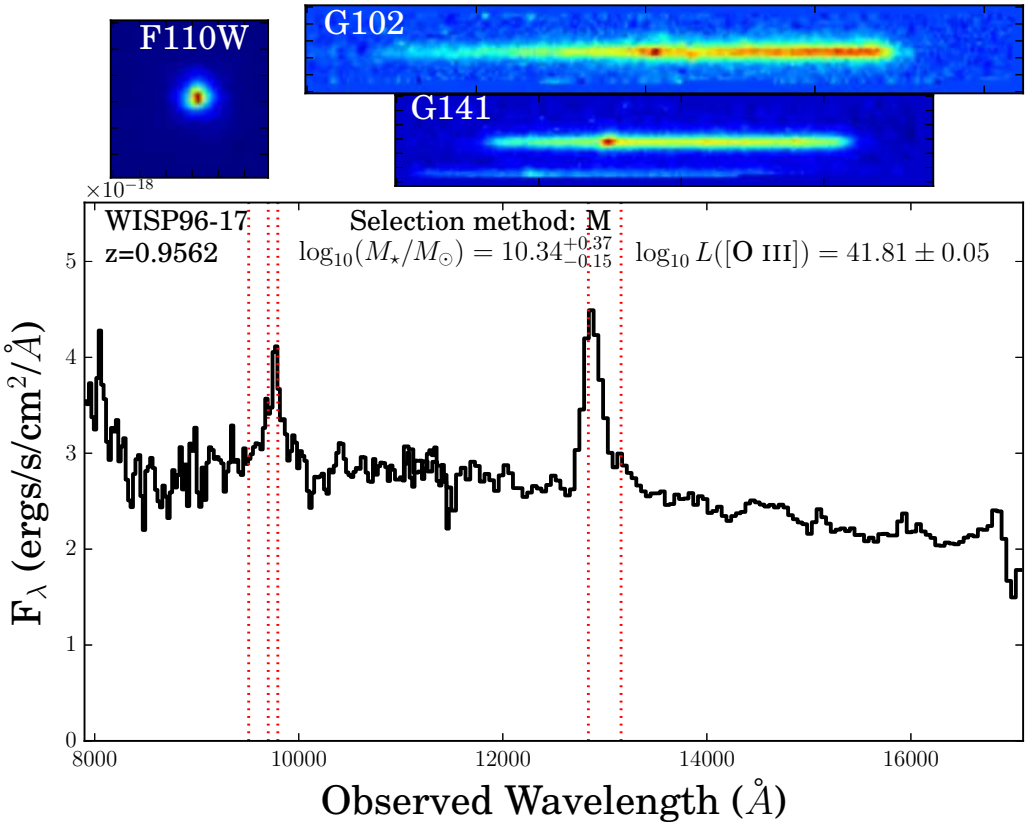

Figure 3.4 Here we show the J_{110} image, 2-d grism spectra and 1-d extracted spectrum for a galaxy selected as an AGN by the MEx selection criterion of Juneau et al. (2014). Vertical red lines mark (from left to right) the positions of Hβ, the [O III] doublet, Hα and [S II].

$$O_{32} \equiv \log_{10}\left(\frac{[\text{O III}]\lambda\lambda 4959, 5007}{[\text{O II}]\lambda\lambda 3726, 3729}\right). \quad (3.2)$$

For selecting AGN using [O III]/Hβ vs. [O II]/Hβ, I use the selection line of Lamareille et al. (2004). An example of an AGN selected by this criterion is shown in Figure 3.7. I investigated using the Lamareille et al. (2004) selection criterion for R_{23} vs. O_{32} (dashed line in Figure 3.6) as well, but this selection line picks up primarily young, low-mass, low-metallicity galaxies which have large [O III]/[O II] ratios driven by an increase in electron temperature in the low-metallicity plasma. Recent studies have found that galaxies at $z \sim 0.8$ (Jones et al., 2015) and $z \sim 2.3$ (Shapley et al., 2015) follow the metal-poor end of the local R_{23}-O_{32} sequence, but both studies are selected down to a rest-frame-optical magnitude limit: $I = 24$ for the DEEP2 survey data used in Jones et al. (2015) and $H = 24.5$ for the MOSDEF survey data of Shapley et al. (2015). The WISP sample extends to somewhat lower masses and, as we showed in Atek et al. (2011, 2014), is particularly sensitive to an extreme class of star-forming dwarf galaxies with specific star formation rates sSFR $\equiv$ SFR/M$_*$ $\gtrsim 10^{-8}$ year^{-1}. Jones et al. (2015) demonstrate that in the low-metallicity galaxy population at $z \sim 0.8$, R_{23} reaches a maximum value of $R_{23} \sim 10$ at $12 + \log_{10}(\text{O/H}) \sim 8.0$, and O_{32} becomes a good measure of metallicity. I therefore suggest that the criterion of Lamareille et al. (2004) is inappropriate at $z \gtrsim 1$. If I instead adopt a selection criterion for AGN $R_{23} > 10$, I remove 90% of the galaxies in our sample that would have been selected using the R_{23}-O_{32} selection line of Lamareille et al. (2004). An example of one of these $R_{23} > 10$ sources is shown in Figure 3.8. I note that three R_{23}-selected galaxies with $10^8 < M_* \lesssim 10^9$ M$_\odot$ remain in our sample, and further note that a quarter of the discarded sources lie above $R_{23} = 10$ with between 90% and 95% confidence, just missing my selection criterion (listed in Table 3.7).

Note that because I have not corrected for dust extinction, I would tend to overestimate O_{32} and underestimate R_{23} and [O II]/Hβ. [O III]/Hβ, as discussed

above should not be strongly effected by dust extinction. As I have opted for a selection on R_{23} independent of O_{32}, I do not expect that any possible overestimate of O_{32} to affect the sample. Underestimation of R_{23} is a possible source of incompleteness for our AGN sample in the sense that a dusty AGN would be observed to have a lower R_{23} compared to its intrinsic value. Finally, the underestimation of [O II]/Hβ is likely a minor source of incompleteness for this selection technique: as can be seen in Lamareille et al. (2004), nearly all of the AGN selected by this diagram have $\log_{10}([\text{O II}]/\text{H}\beta) < 1.3$ where the selection curve flattens off. Neglecting dust absorption would only cause me to miss the most intrinsically [O II]-luminous but highly dust-obscured AGN.

3.3.4 Removal of contaminating sources

In order to examine contaminating sources from our AGN sample, I inspected the 1-dimensional extracted spectra, the 2-dimensional WFC3 Grism spectra, the direct images and the FAST stellar population fits to the WISP photometry. I removed ten sources from my sample because the [O III] emission was seen primarily to be spatially extended, instead of centrally concentrated as expected for an AGN. I removed seven sources from my sample because of contamination in our Grism spectra at the position of [O III] and Hβ from confusion with a nearby source. The redshifts for these galaxies are considered reliable, but the flux uncertainty estimates for these sources are likely underestimated and so I remove them from my analysis. Five sources were selected only by the MEx diagram and were effected by confusion in their photometry which led to an overestimate their stellar mass in my FAST stellar population model fits. I removed these five sources from my sample as well.

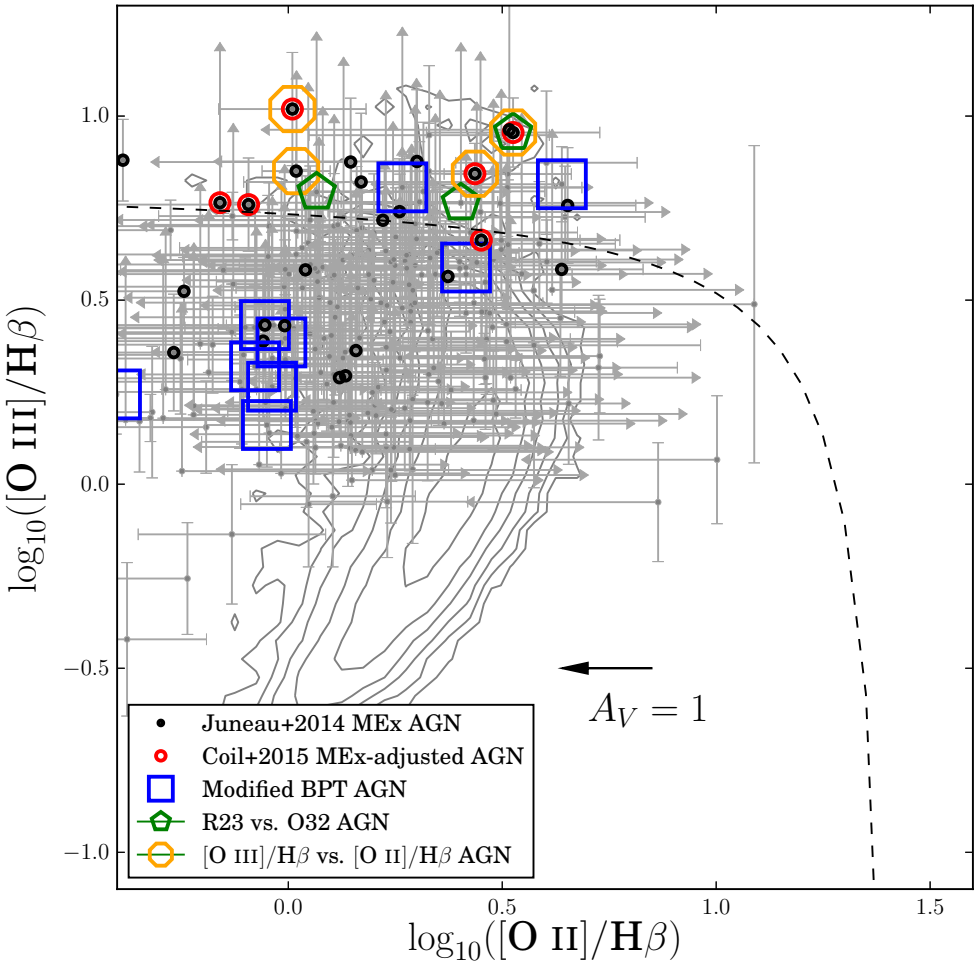

Figure 3.5 Selection of WISP AGN using the [O III]/Hβ vs. [O II]/Hβ selection criterion of Lamareille et al. (2004). The black arrow shows the effect of 1 magnitude of V-band extinction on the intrinsic ratio for [O II]/Hβ, assuming the Cardelli et al. (1989) extinction law with $R_V = 3.1$.

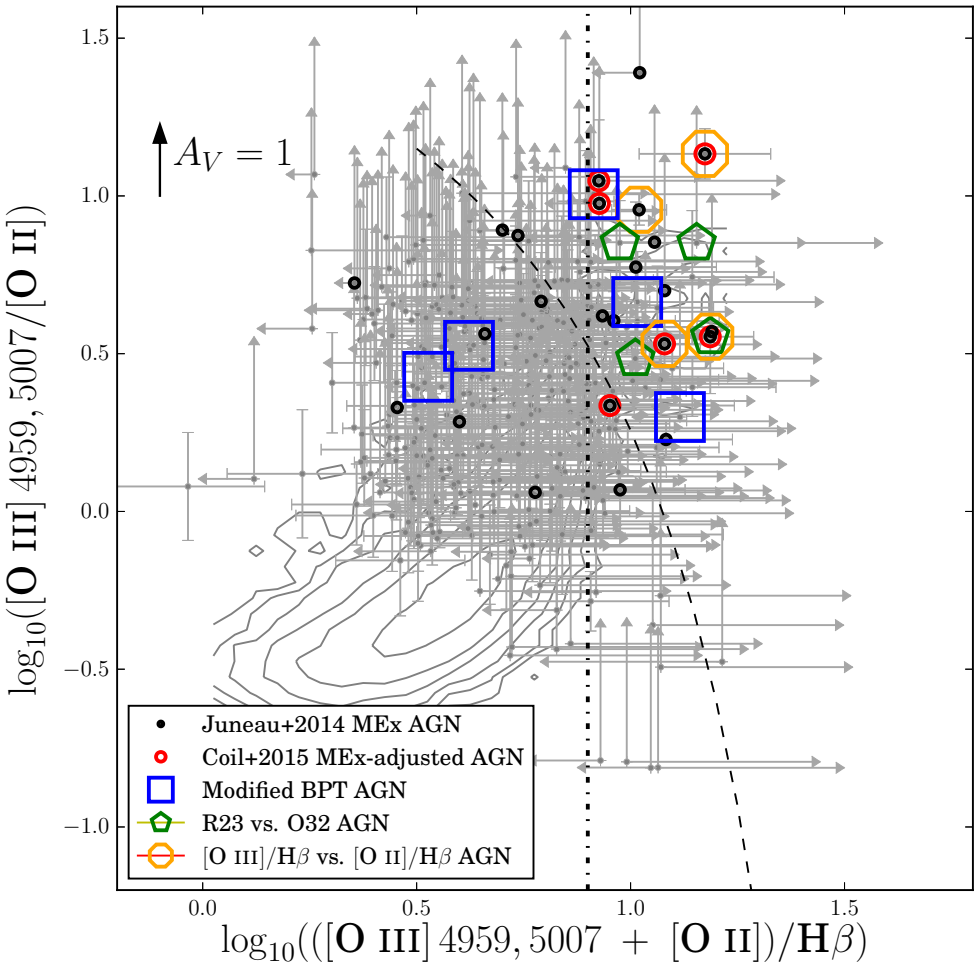

Figure 3.6 Our WISP galaxies have higher ionization parameter than SDSS galaxies, as seen by the high [O III]/[O II] ratios as a function of R23 (a proxy for metallicity). Gray contours are SDSS galaxies; the black dashed line shows the AGN selection criterion of Lamareille et al. (2004). The black dot-dashed line shows the AGN selection criterion, $R_{23} > 10$, adopted here. The black arrow shows the effect of 1 magnitude of V-band extinction on the intrinsic ratio for [O III]/[O II], assuming the Cardelli et al. (1989) extinction law with $R_V = 3.1$. Note that the effect of extinction on R_{23} is dependent on the intrinsic O_{32} ratio.

3.3.5 The WISP AGN sample

From among our sample of 668 [O III] emitters, I find 34 sources selected as AGN (with $P(SF) < 0.05$) using the MEx technique of Juneau et al. (2014). Only

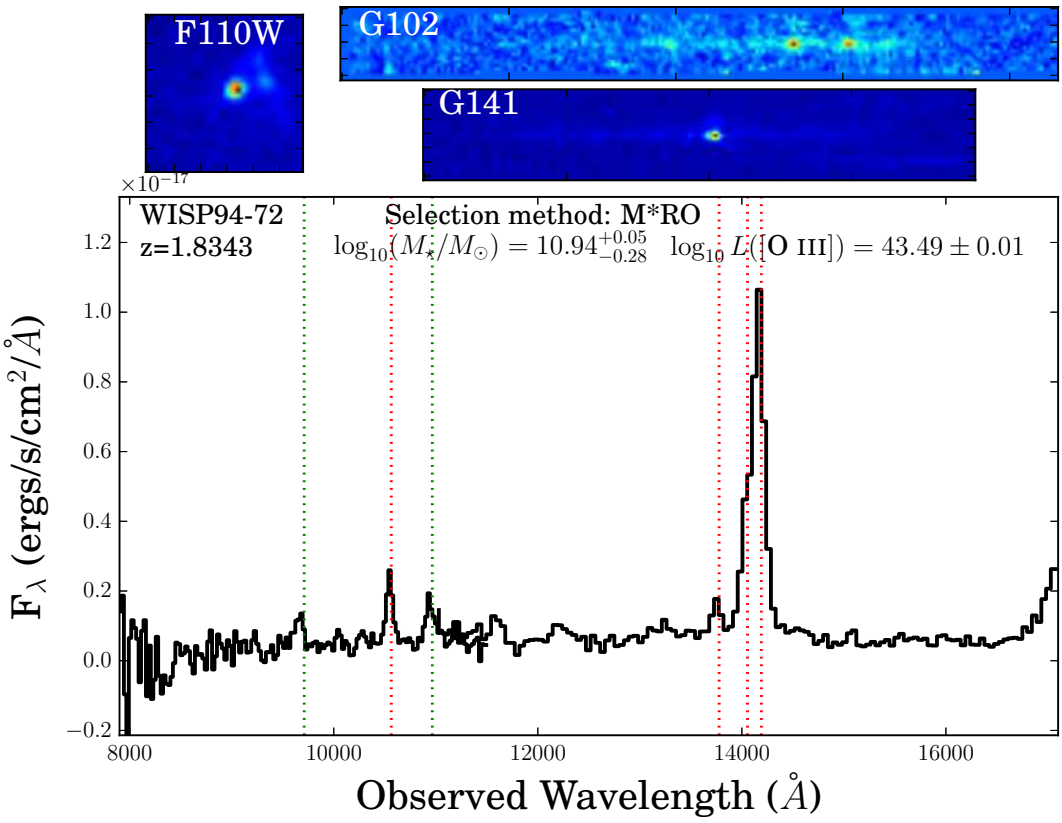

Figure 3.7 Here we show the J_{110} image, 2-d grism spectra and 1-d extracted spectrum for a galaxy selected as an AGN by our [O III]/Hβ vs. [O II]/Hβselection criterion. Vertical red lines mark (from left to right) the positions of [O II], Hβ, and the [O III] doublet. Vertical green lines mark the position of [Ne V]λ3426 and [Ne III]λ3869, blueward and redward of [O II], respectively. This galaxy is also selected as an AGN by the MEx criterion.

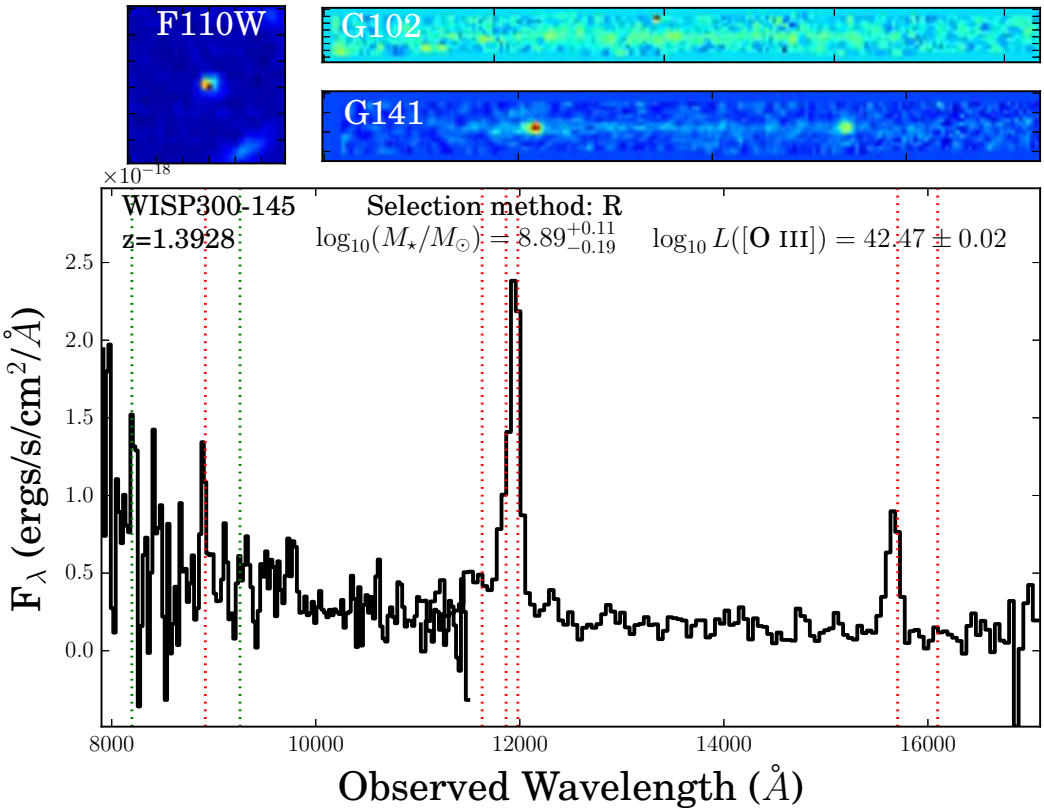

Figure 3.8 Here we show the J_{110} image, 2-d grism spectra and 1-d extracted spectrum for a galaxy selected as an AGN by our $R_{23} > 10$ selection criterion. Vertical red lines mark (from left to right) the positions of [O II], Hβ, the [O III] doublet, Hα and [S II]. Vertical green lines mark the position of [Ne V]λ3426 and [Ne III]λ3869, blueward and redward of [O II], respectively.

6 meet the more restrictive requirements recommended by Coil et al. (2015) for the MEx selection criteria for $z \sim 2$ galaxies. I find 14 galaxies that satisfy my modified-BPT criterion, although I note that this selection method is used only for the 376-galaxy subset of our [O III] sample that is at $z < 1.55$ and has Hα detected at $> 3\sigma$. I find only 4 AGN selected by the $R_{23} > 10$ criterion and 4 selected by the [O III]/Hβ vs. [O II]/Hβ criterion. These latter criteria are only used on the subsample of the galaxies at $z > 1.2$. Several of my sources are selected by multiple criteria (see Table 3.4), so the union of my sample selections is 50 AGN if I adopt the Juneau et al. (2014) MEx method and 24 AGN if I instead require the more restrictive selection criterion of Coil et al. (2015). Note that the 50 [O III]-selected AGN represent 7.5% of the WISP [O III]-emitters, but only 2.7% of the full $0.62 < z < 2.39$ emission-line galaxy sample. This is in line with the fraction of UV-selected AGN found in Lyman Break Galaxies at $z \sim 3$ by Steidel et al. (2002), although I note that my sample is subject to much more uncertain incompleteness due to my varied selection techniques. The redshift histogram of my AGN sample is shown in Figure 3.9. While the number of sources is small, there does not appear to be a strong trend in number of AGN detected with redshift. This is in contrast to the strong decrease in the number of sources at $z > 1.5$ in the full WISP emission-line galaxy sample (Figure 2.3). This is likely due to a selection effect: AGN tend to be the brightest [O III] emitters at any redshift, so at higher redshifts, I am more likely to find the AGN than a more typical, weak-[O III]-emitting, star-forming galaxy.

I plot the distribution of [O III] luminosities and stellar masses for my AGN sample in Figure 3.10. Note that the MEx selection and R_{23}/BPT selection techniques seem to be comlementary: the MEx technique is inherently biased toward selecting AGN in massive galaxies, especially under the suggested more restrictive selection criterion of Coil et al. (2015). The other selection techniques are explicitly agnostic about the mass of a galaxy (although the correlations between

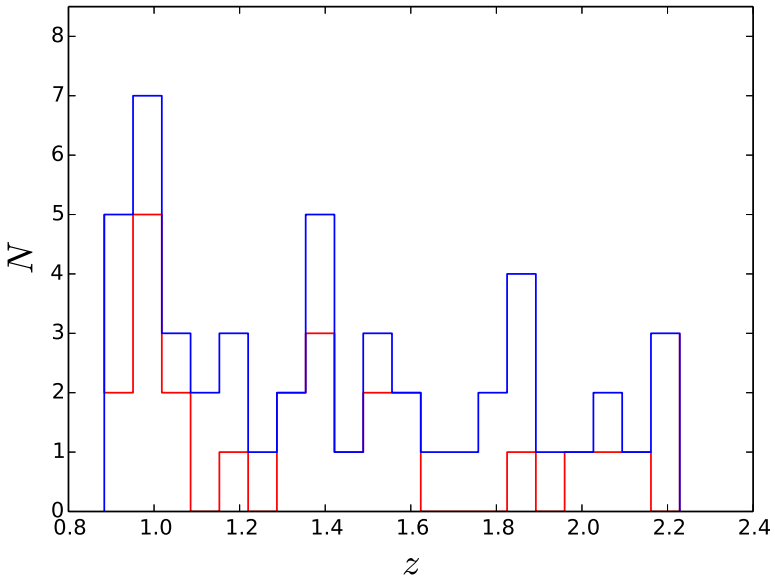

Figure 3.9 The WISP AGN sample appears to have a fairly flat distribution in redshift, especially compared to the overall WISP emission-line galaxy sample distribution shown in Figure 2.3. The blue histogram shows the total AGN sample when we use the Juneau et al. (2014) MEx selection method. The red histogram shows the AGN sample derived when we use the more conservative MEx selection criterion of Coil et al. (2015).

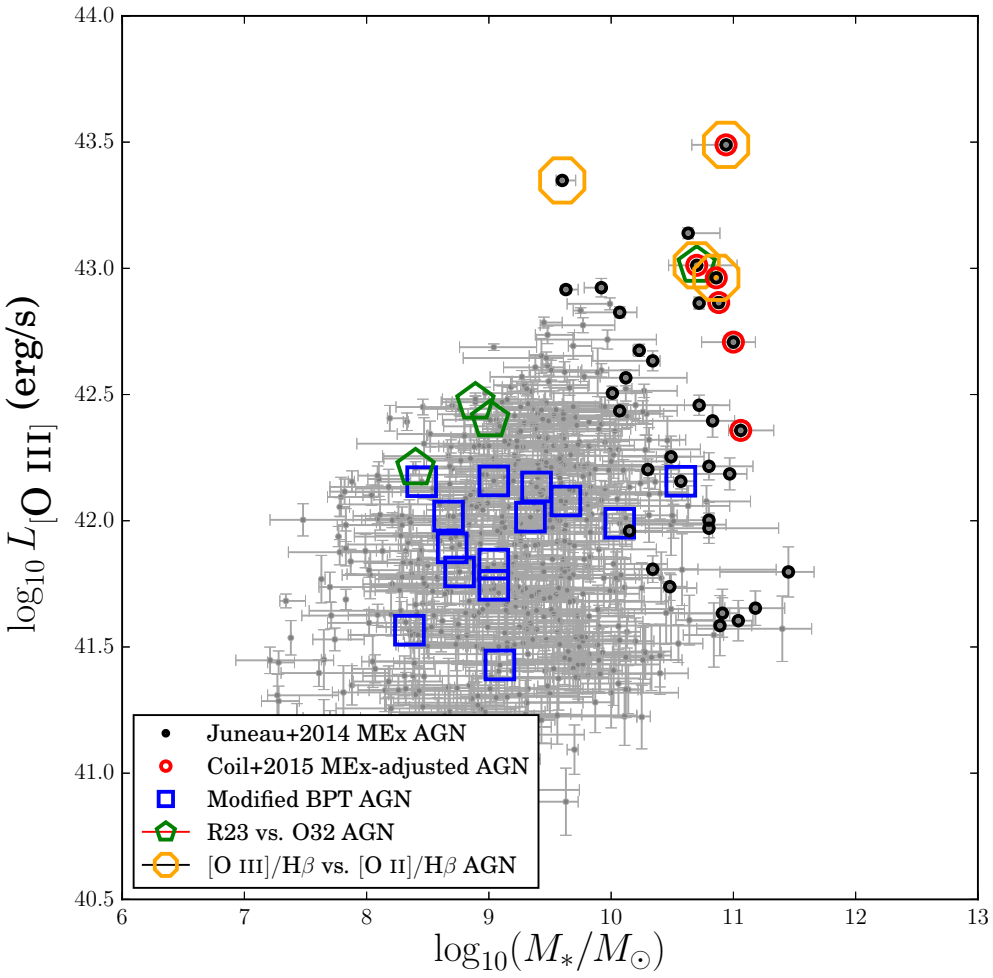

Figure 3.10 Here we show the WISP [O III]-selected emission-line galaxies in the $L([\mathrm{O\ III}])$-M_* space. The WISP R_{23}-selected AGN sample is clearly preferentially selected from the high-$L([\mathrm{O\ III}])$ end of the WISP distribution at $M_* \lesssim 10$.

stellar mass, gas-phase metallicity, and SFR per unit mass complicate this picture; see, e.g. Mannucci et al., 2010; Henry et al., 2013; Maier et al., 2014; Zahid et al., 2014; Sanders et al., 2015; Ly et al., 2015). The R_{23} and BPT selection techniques find AGN candidates with stellar masses as low as $\sim 10^8$ $M_\odot$. Most studies presume that AGN are unlikely to be found in such low-mass galaxies for several reasons: first, if we assume the $M_{bh} - M_*$ relation observed locally is in place at $z \gtrsim 1$ *and* that it can be extrapolated to lower galaxy stellar masses than we have measured locally (i.e. to $M_{bh} \lesssim 10^6$ $M_\odot$), then the expected accretion luminosities are $L_{bol} \lesssim 10^{43}$ erg/s (assuming accretion at $0.1 \times L_{Edd}$). Second, the dwarf galaxies at $z \gtrsim 1$ are found to be forming stars very rapidly compared to local galaxies, so even if an accreting SMBH is present in these dwarf galaxies, the blending of the AGN ionization signature with the ionization signatures produced by all of the newly-formed massive stars would bias us against discovering the AGN (e.g. Trump et al., 2015; Coil et al., 2015). I discuss these assumptions in the context of my $M_* < 10^{10}$ $M_\odot$ AGN candidates in depth below.

3.3.6 Search for confirmation in WISE

While I note that the majority of my AGN candidates are faint, I nonetheless searched the AllWISE catalog (Wright et al., 2010; Mainzer et al., 2011) for mid-IR detections of the AGN candidates. Eleven of my sources are found in the AllWISE source catalog. Of these, WISP311-42, WISP311-59, and WISP291-12 surpass the $W1 - W2 = 0.8$ (Vega) WISE AGN selection criterion of Stern et al. (2012) and Assef et al. (2013), although I caution that most of my sample is fainter in $W2$ than the 15.73 Vega magnitude limit where Assef et al. (2013) show that both the reliability and completeness of their selection are falling steeply. These same three sources were also detected in the 12μm $W3$ band, further confirming their identification as AGN. Only one source, WISP311-42, was detected in the 22μm $W4$ band. The WISE photometry is listed in Table 3.6.

3.4 Discussion

I can estimate the black hole mass of my AGN if I assume a relationship between host-galaxy stellar mass and SMBH mass. I use the Bennert et al. (2011) relation between black hole mass (M_{bh}) and host stellar mass (M_* – both in solar units)

$$\log_{10} M_{bh} - 8 \;=\; 1.12\,[\log_{10} M_* - 10] \;+\; 1.15\,\log_{10}[1+z] \;-\; 0.68 \qquad (3.3)$$

for my AGN candidates. This relation evolves with redshift such that the SMBH mass makes up a larger fraction of the total galaxy mass at higher redshift. Bennert et al. (2011) report an intrinsic scatter of 0.16 dex in their M_{bh}-M_* relation. Other studies have found that the M_{bh}-M_* relation may have no redshift evolution, once observational biases are accounted for (Schramm & Silverman, 2013; Sun et al., 2015). Therefore, I also estimate black hole masses assuming the local M_{bh}-M_* relation of Häring & Rix (2004), which has an intrinsic scatter of $\Delta \lesssim 0.3$ dex.

The luminosity of [O III] has been found to correlate with the total bolometric luminosity of an AGN (e.g. Heckman et al., 2004; Trouille & Barger, 2010). Heckman et al. (2004) found that, in local galaxies from the SDSS, $L_{Bol}/L([\text{O III}]) \sim 3500$ with a scatter of 0.38 dex when $L([\text{O III}])$ is uncorrected for dust extinction. For dust-corrected [O III], Kauffmann & Heckman (2009) find that $L_{Bol}/L([\text{O III}]) \sim 600$. While I could conceivably determine individual extinction corrections for the $z < 1.55$ AGN sample using the Balmer decrement, much of the sample only has weak detections or upper limits for the Hβ line and at $z > 1.55$, the Hα line is redshifted out of our spectral coverage. Furthermore, I would have to apply a large, but highly uncertain, correction to the Hα fluxes to account for the blend with the [N II]$\lambda\lambda$6548,6583Å doublet. I do not attempt to derive extinction corrections from my FAST stellar population parameter results because I do not expect the extinction of the AGN narrow-line region to match

the average extinction of the galaxy stellar light taken as a whole.

Stern & Laor (2012) found that the bolometric correction to $L([\text{O III}])$ for Type 1 AGN is luminosity dependent, with smaller bolometric corrections required for lower-luminosity AGN, of the form

$$\frac{L_{bol}}{10^{43}\,\text{erg/s}} = 4000^{\times 4}_{\div 4} \left(\frac{L([\text{O III}])}{10^{43}\,\text{erg/s}}\right)^{1.39}. \tag{3.4}$$

Although the majority of my sources show no signs of broad Balmer lines, I nonetheless consider the Stern & Laor (2012) luminosity dependent bolometric correction for my sources along with the results of Heckman et al. (2004) and Kauffmann & Heckman (2009).

We can now compare the bolometric luminosity estimates to the Eddington Limit (Eddington, 1926). The resulting Eddington ratio, $\lambda_{Edd} \equiv L_{bol}/L_{Edd}$, is plotted against galaxy stellar mass in Figure 3.11. As can be seen in Figure 3.11, there is a clear trend in the estimate of λ_{Edd} with stellar mass for my AGN candidates if we assume a bolometric correction that is constant with respect to $L([\text{O III}])$. Additionally, for galaxies with stellar mass below $M_* \lesssim 10^{10}$ $\text{M}_\odot$, we would infer an Eddington ratio $\lambda_{Edd} > 1$ for most of the AGN candidates. While there are considerable uncertainties in scaling from the measured quantities ($L([\text{O III}])$ and M_*) to the inferred λ_{Edd}, I do not expect them to be more than 1 dex. I show the inferred Eddington ratios under the assumptions that the (1) bolometric correction increases with luminosity as in Stern & Laor (2012), and (2) the M_{bh}-M_* relation evolves with redshift as in Bennert et al. (2011), as black points in Figure 3.11. These assumptions yield lower Eddington ratios, although 10 of my 50 sources still have inferred $\lambda_{Edd} > 1$. If we assume no evolution of the M_{bh}-M_* relation out to $z \sim 2$ (blue points in Figure 3.11), the fraction of my sources with $\lambda_{Edd} > 1$ increases to 21/50.

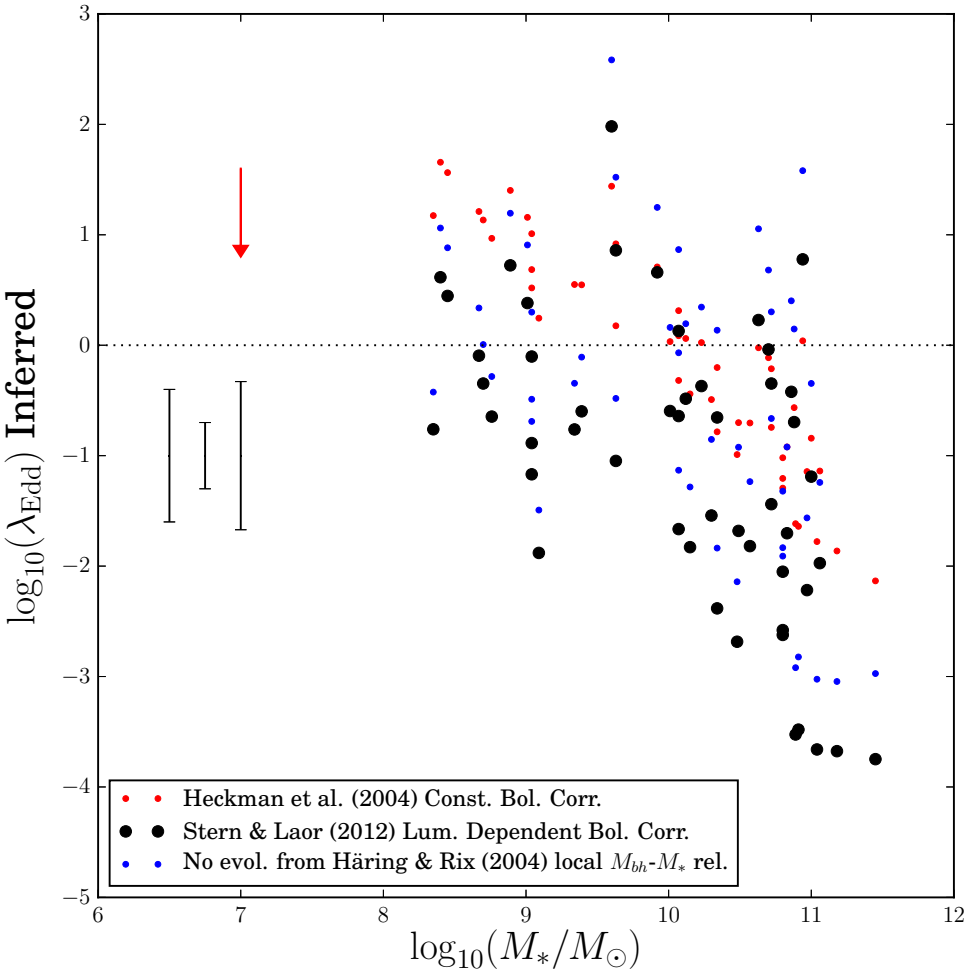

Figure 3.11 Inferred Eddington Ratios for the WISP AGN sample, derived assuming the $M_{bh} - M_*$ relation of Bennert et al. (2011) and either the Stern & Laor (2012; black points) or Heckman et al. (2004; red points) bolometric corrections to L([O III]). Blue points show the inferred eddington ratios if we assume no evolution from the local $M_{bh} - M_*$ relation of Häring & Rix (2004) and the Stern & Laor (2012) bolometric correction. The red arrow shows the effect of using the Kauffmann & Heckman (2009) dust-extinction-corrected bolometric correction of ~ 600 instead of the Heckman et al. (2004) value of ~ 3500. The error bars show, from left to right, the scatter in the Stern & Laor (2012) bolometric correction, the scatter in the local $M_{bh} - M_*$ relation, and the quadrature sum of the two.

3.4.1 Misidentification of extreme star-forming dwarf galaxies as AGN

For the 8 dwarf-galaxy AGN candidates, and the 10 galaxies that just missed my 95%-confidence $R_{23} > 10$ selection cut (Table 3.7), we must consider whether and under what conditions the gas in these galaxies could be entirely photoionized by stars. In order to test this, I ran a suite of *Cloudy* (Ferland et al., 2013)[5] photoionization models for blackbody ionizing spectra at 32,500 K, 40,000 K, and 55,000 K. I varied the gas density from 10^1 cm^{-3} to $10^{2.8}$ cm^{-3} in 0.3 dex steps, the ionization parameter U (defined as the ratio of the number of ionizing photons to the number of hydrogen atoms) from 10^{-4} to $10^{-0.7}$ in 0.3 dex steps, and the metallicity from $10^{-2.5}\times$ to $1\times$ the solar metallicity in 0.5 dex steps. I assume a spherical geometry. I find that even the highest gas densities and ionization parameters allowed in my model grid fail to produce H II regions with the high [O III]/[O II] and [O III]/Hβ ratios seen in the R_{23}-selected AGN sample if the ionizing spectrum can be approximated by a 30,000–40,000 K blackbody. As I show in Figure 3.12, a hotter blackbody can produce the observed high O_{32} line ratios for $R_{23} < 10$, but only if the gas conditions are drastically different from local H II regions. The models that rise above the Lamareille et al. (2004) AGN selection line in R_{23} vs. O_{32} all have ionization parameters $U > 10^{-2.2}$, compared to typical values of $U \sim 10^{-3.5}$ at $z \sim 0.2$ (Shirazi et al., 2014). This is consistent with the findings of Steidel et al. (2014), who used a similar set of models to show that the high [O III]/Hβ ratios of star-forming galaxies at $z \sim 2.3$ could be explained by combination of high ionization parameters and harder ionizing spectra compared to local galaxies. The densities are also consistent with the densities measured directly by Jones et al. (2015) for their sample at $z \sim 0.8$, although my sample extends to higher [O III]/[O II] and [O III]/Hβ.

The 55,000 K blackbody model does not produce [O III]/H$\beta \gtrsim 8$, even for very high ionization parameters ($U \gtrsim 0.1$), nor does it produce the [S II]/(Hα+[N II])

[5]Version 13.03

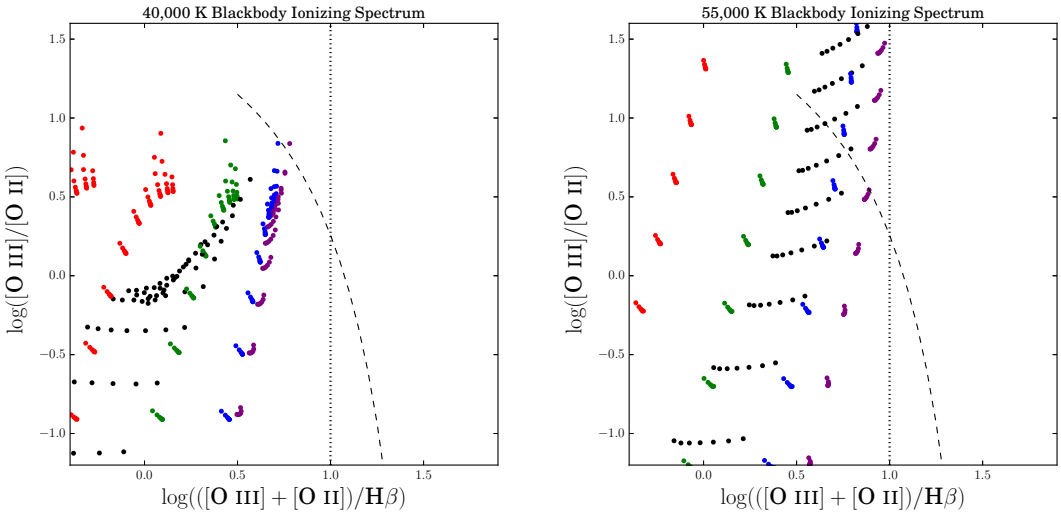

Figure 3.12 *Cloudy* Version 13.03 (Ferland et al., 2013) photoionization models for R_{23} vs. O_{32}, assuming a blackbody ionizing spectrum of 40,000 K (left) and 55,000 K (right). The point colors represent the metallicity of each grid point: red ($\leq 10^{-2}$ $Z_\odot$), green ($10^{-1.5}$ $Z_\odot$), blue (10^{-1} $Z_\odot$), purple ($10^{-0.5}$ $Z_\odot$), black ($Z_\odot$). For the 40,000 K ionizing spectrum, only the highest-density model ($10^{2.8}$ cm^{-3}) with a moderate metallicity ($Z = 0.5\,Z_\odot$) and high ionization parameter ($\log_{10} U = 0.7$) can produce line ratios above the Lamareille et al. (2004) AGN selection line (black dashed). None of the models produce $R_{23} > 10$, the adopted AGN selection criterion in this work.

ratios seen in my modified-BPT-selected AGN (see Figure 3.13). None of the models predict $R_{23} > 10$, my adopted R_{23} AGN selection criterion in this work. One further prediction of the photoionization models is a high [Ne III] 3869Å/[O II] ratio ($\gtrsim 1/3$; see Figure 3.14), especially for low gas-phase metallicities. Several of our sources do show strong [Ne III] (WISP303-324, WISP309-157, WISP64-213, WISP304-304), but the majority do not. I suggest that deep rest-frame UV spectoscopy could help determine whether these $M_* < 10^9$ $M_\odot$ AGN candidates are true AGN or extreme star-forming galaxies. If these candidates are truly AGN, we might expect to find high-ionization lines such as N V in the far-UV.

In order to predict the UV emission-line spectra of my galaxies, I ran an additional *Cloudy* model for an AGN ionizing spectrum. The AGN is assumed to follow a power law with an exponential cutoff (forming the "Blue Bump")

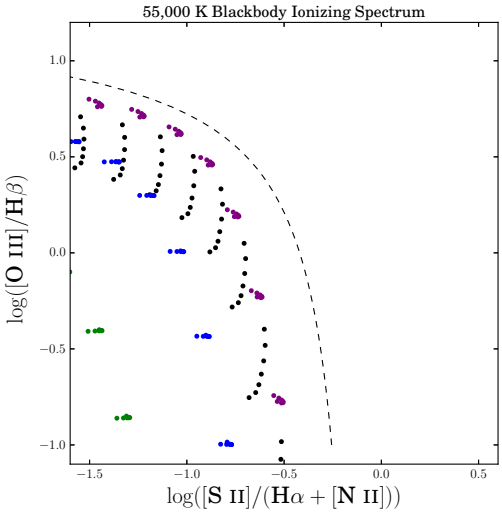

Figure 3.13 *Cloudy* (Ferland et al., 2013) photoionization models assuming a 55,000 K blackbody ionizing spectrum and high ionization parameters can produce emission-line ratios for H II regions with [O III]/H$\beta \lesssim 8$. Colored points indicate the metallicity, as in Figure 3.12. Even for high ionization parameters and gas densities, the models do not produce line ratios seen in the modified-BPT-selected AGN.

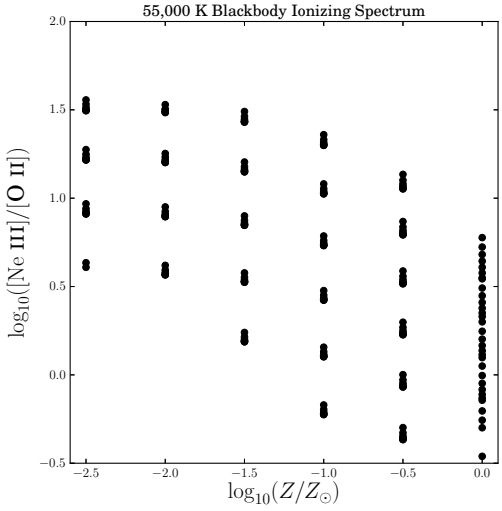

Figure 3.14 *Cloudy* (Ferland et al., 2013) photoionization models for which a 55,000 K blackbody spectrum and high ionization parameter can produce emission-line ratios for H II regions that lie above the R_{23} vs. O_{32} AGN selection line of Lamareille et al. (2004) also predict strong [Ne III] 3869Å emission.

in the UV with a break to a second power law in the X-ray. The X-ray power law is normalized to match the Optical-to-X-ray ratios observed for local AGN, $\alpha_{ox} \sim -1.4$. The exponential cutoff of the "Blue Bump" is assumed to occur at a characteristic temperature T_{BB} =100,000 K. I assume a hydrogen gas density of 10^3 cm^{-3} and an ionization parameter of $\log_{10} U = -2$. Both the models with the AGN ionizing spectrum and the 55,000 K blackbody ionizing spectrum generically predict that the strongest UV emission line would be Lyα. However, this line is resonantly scattered by neutral hydrogen gas and dust grains, producing a widespread array of Lyα emission and absorption strengths in $z \sim 2$ galaxies (see e.g. Steidel et al., 2004; Erb et al., 2014). The next strongest predicted emission-line strength for both models is the C III] $\lambda\lambda$1907,1909Å doublet. Note that Stark et al. (2014) saw exactly this strong C III] emission in their study of gravitationally-lensed low-mass ($M \sim 10^6 - 10^9$ M$_\odot$) galaxies at $z \sim 2$. Both the mass and redshift ranges of the Stark et al. (2014) study match the galaxies considered here, and the large [O III]+Hβ equivalent widths they infer from stellar population model fits to their photometry likewise match the WISP sample. Stark et al. (2014) suggest that their extreme star-forming dwarf galaxies at $z \sim 2$ represent analogs to the young galaxies forming at $z \sim 6$, and that the C III] line represents the best current prospect of obtaining spectroscopic redshifts for photometrically-selected $z \gtrsim 6$ galaxy candidates (this was confirmed by the discovery of strong C III] emission in two $z \sim 6$ galaxies by Stark et al., 2015).

I find that the distinguishing rest-frame-UV line ratios between the AGN and 55,000 K blackbody models are: He II λ1640/C III] and C IV $\lambda\lambda$1548,1551Å/C III]. For the AGN model, I predict He II λ1640/C III] $\sim$ 40% and C IV/C III] $\sim$ 50%, compared to 3% and 6%, respectively, for the 55,000 K blackbody model, although I note that in actual galaxy spectra, the He II λ1640 may be boosted by contributions from stellar winds. Both models predict O III] $\lambda\lambda$1661, 1666Å/C III] $\sim$ 10%. The AGN model does not predict particularly strong emission for N V $\lambda\lambda$1239, 1243Å

or N IV λ1485, each roughly 2% of C III]. I note that the stack of $z \sim 2.5$ Seyfert 2 UV spectra of Hainline et al. (2011) shows much stronger N V/C III] ~ 0.4 and C IV/C III] ~ 1.2, implying an even harder ionizing spectrum than I assumed for my AGN model. The Lyman Break Galaxies from which the Hainline et al. (2011) sample are drawn have stellar masses $M_* > 10^{10}$ M$_\odot$ (Hainline et al., 2012), overlapping only with the massive end of my sample, and are thus likely to have higher metallicities than my low-stellar-mass AGN candidates.

For the 5 sources for which Stark et al. (2014) detect UV emission lines in addition to C III] and Lyα, three show C IV $\lambda\lambda$1548,1551Å/C III] $\sim 0.4 - 0.8$ and a fourth shows He II λ1640/C III] ~ 0.5 (C IV happened to fall on a sky line for this source). Motivated by their observed high O III] $\lambda\lambda$1661, 1666Å/C III] $\sim 0.5 - 0.8$ ratios, Stark et al. (2014) explain their high observed C IV $\lambda\lambda$1548,1551Å/C III] ratios with photoionization models for which they allowed the C/O abundance ratio to decrease relative to what is seen in local galaxies. Their photoionization models failed to reproduce their one high He II λ1640/C III] detection (limits on He II in their other C IV emitters are not very stringent). Their rest-frame-optical spectroscopy of this source (MACS 0451-1.1) shows $\log_{10} O_{32} > 0.95$ and $\log_{10} R_{23} > 0.91$, likely placing it in the AGN-selection region used in this work. I suggest that at least one of the Stark et al. (2014) dwarf galaxies is a candidate low-stellar-mass AGN host at $z = 2.060$. Given the results of Stark et al. (2014), I do not conclusively rule out the possibility that some of our $M_* \lesssim 10^9$ M$_\odot$ R_{23}-selected AGN candidates are true AGN at $z > 1.5$.

3.4.2 Bolometric correction overestimate or black hole mass underestimate

In deriving the Eddington ratios shown in Figure 3.11, we examined various assumptions about the bolometric correction, $L_{bol}/L_{[\mathrm{O\ III}]}$. However, the bolometric corrections I used (from Heckman et al., 2004; Kauffmann & Heckman, 2009;

Stern & Laor, 2012) were derived for local AGN which reside in more massive, metal-rich galaxies than the low-mass, $z \sim 1-2$ host galaxies considered here. If a greater fraction of the total AGN flux is emitted in [O III] for low-mass black holes, or in low-metallicity environments, then the adopted bolometric corrections would overestimate the bolometric luminosity, and therefore the Eddington ratio. One possible scenario in which more of the bolometric luminosity would be emitted in [O III] is if there is a lack of dust around the AGN. Without a dusty 'torus' around the AGN, the hot accretion disk would be exposed to a greater fraction of the galaxy, and ionize a greater volume of gas to produce a larger Narrow-Line Region extending into the host galaxy. In this scenario, we would expect to find the UV emission-line strengths discussed above and a high X-ray luminosity, but no evidence of the mid-IR hot dust emission characteristic of most AGN. We do not have any deep X-ray observations of the WISP fields, and the current available mid-IR facilities are not sensitive enough to rule out significant mid-IR emission from a dusty torus. I suggest that the combination of future JWST mid-IR photometry with deep X-ray observations of my sources may reveal that some of them are in a class of previously-unstudied dust-free (perhaps due to low-metallicity gas) AGN. Note that X-ray measurements for the Stark et al. (2014) sample will be difficult to obtain: their sources are lensed by massive galaxy clusters for which the extended X-ray emission from hot intracluster gas will likely overwhelm any possible signal from their AGN candidates.

An alternative way to reduce the inferred Eddington ratios for the low-stellar-mass AGN candidates is to reject the assumption that these galaxies lie on a low-mass extrapolation of the local M_{bh}-M_* relation. If these galaxies contain SMBH more massive than we would expect from the M_{bh}-M_* relation, then the Eddington ratios would be overestimated. As noted in the introduction, there are considerable theoretical uncertainties in determining how dark matter halos are populated with massive black holes. The most likely source of SMBH seeds

seems to be the remnants of the first generation of stars. However, it remains possible that some could form by the direct collapse of a primordial gas mass in excess of 10^3 $M_\odot$ with molecular hydrogen depletion due to a UV Lyman-Warner band background radiation. Agarwal et al. (2013) postulate the existence of these "obese black hole" galaxies[6] at $z \sim 6$ with $M_{bh} > M_*$ for SMBH seeds produced by the direct-collapse scenario. In this scenario, the SMBH is the first compact object to form in its dark matter halo. If the galaxy ISM remains un-enriched by either stars or galaxy mergers, it may be possible to delay star formation in these halos, even after the black hole growth rate has significantly slowed (Agarwal et al., 2013). If this scenario holds true, then there may be a dark matter halos with the right conditions to form SMBH seeds at early times, but which are delayed in forming its first generations of stars until we begin to see them as low-mass, low-metallicity, young star forming galaxies at $z \sim 2$. I note, however, that Agarwal et al. (2014) predict that the direct-collapse black holes will form in halos within ~ 15 kpc of more massive star-forming galaxies. I did not find spectroscopic companions to our low-stellar-mass AGN candidates within a projected separation of 30 kpc and velocity $\Delta v < 1000$ km/s. Note, however, that I would miss recently quenched star-forming galaxies in this search.

3.5 The WISP AGN Luminosity Function

I use the sample of 44 AGN selected above to derive an AGN luminosity function using the V_{max} method outlined by Felten (1977). The V_{max} method is used for flux-limited surveys and assigns an effective survey volume to each source based of the source luminosity and survey flux limit. For a measured luminosity L([O III]) and flux limit f_{lim}, the maximum (luminosity) distance at which the source could

[6]Their term.

be found in the survey is

$$D_{lum,max} = \sqrt{\frac{L([\text{O III}])}{4\pi f_{lim}}}, \tag{3.5}$$

corresponding to a redshift z_{max} for which $D_{lum}(z_{max}) = D_{lum,max}$. The effective volume for each source is then

$$V_{max} = \int_{z_{min}}^{z_{max}} \frac{dV_{comoving}}{dz} dz. \tag{3.6}$$

Due to the non-uniform survey depth of the WISP fields, and the strong variations in sensitivity of the grism spectra as a function of observed wavelength, we must calculate an effective volume for the depth of each WISP field. For each source, then, its effective density δ_i is taken to be

$$\delta_i = C(S/N_i, EW_i, z_i) \sum_j \frac{1}{V_{max,i,j}}, \tag{3.7}$$

where $C(S/N, EW, z)$ is a completeness correction, as described in Chapter 2.

I next bin the galaxies according to their [O III] luminosities in order to produce a luminosity function. The result is shown in Figure 3.15 in two redshift divisions. For comparison, I show the Seyfert 2 [O III] luminosity functions of Malkan et al. (in preparation) for local ($z \sim 0$) galaxies, of Hao et al. (2005) at $z \sim 0.1$ from the SDSS, and of Bongiorno et al. (2010) at $z \sim 0.5$ from COSMOS. As can be seen in Figure 3.15, there appears to be a strong evolution in the [O III] luminosity function from $z = 0.5-2.4$, which is broadly consistent with the overall increase in the cosmic star formation rate (see the review by Madau & Dickinson, 2014) and black hole accretion rate inferred from X-rays (Hopkins et al., 2007; Aird et al., 2010).

For comparison with the X-ray, in Figure 3.15 I also plot the 'Luminosity and

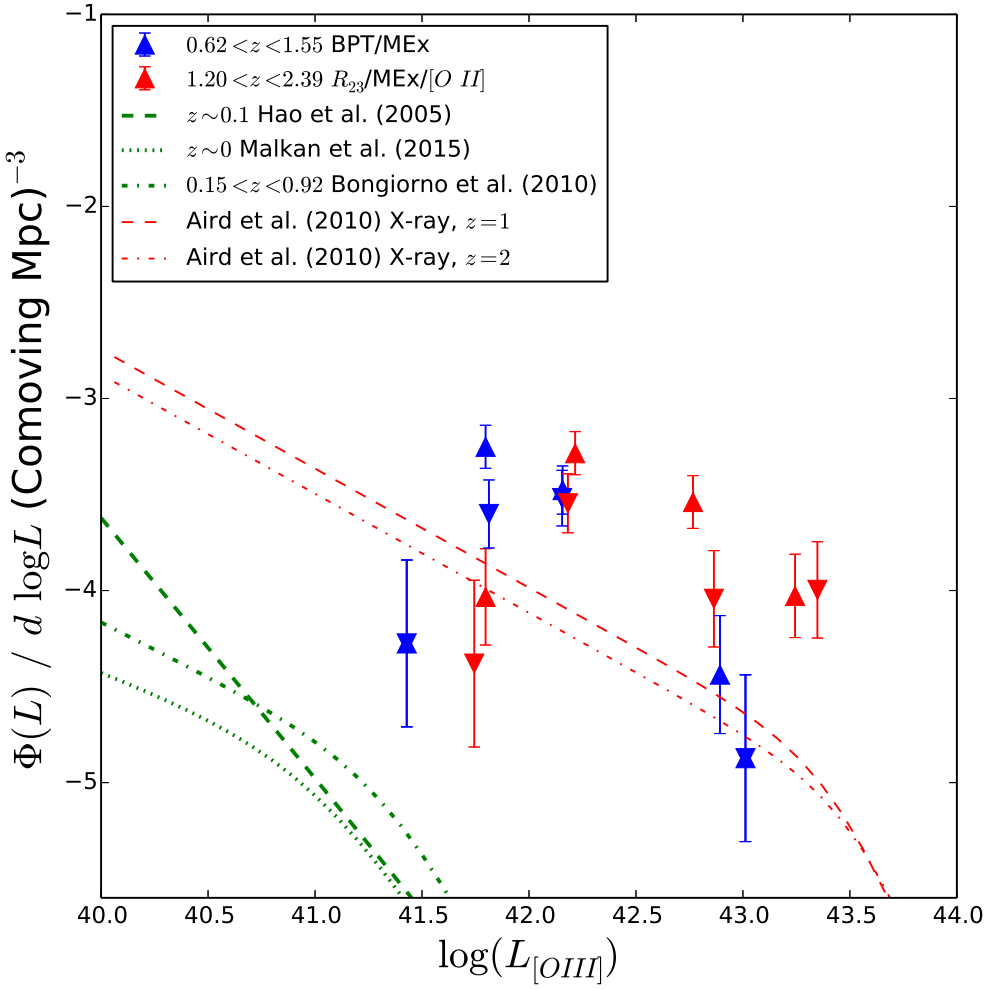

Figure 3.15 The WISP AGN [O III] luminosity function at $0.62 < z < 1.55$ (blue) and $1.20 < z < 2.39$ (red). Upward triangles include all optically-selected AGN. Downward triangles show the effect of using the Coil et al. (2015) adjustment to the MEx selection diagram instead of the Juneau et al. (2014) method. Green lines show the Seyfert 2 luminosity function at lower redshifts from Malkan et al. (in prep) at $z \sim 0$, Hao et al. (2005) at $z \sim 0.1$ using SDSS galaxies, and at $z \sim 0.5$ from Bongiorno et al. (2010). For comparison with the $z = 1 - 2$ X-ray luminosity function, we show the results of Aird et al. (2010), shifted by the X-ray-to-[O III] relation, $L_X/L_{[\mathrm{O\ III}]} \sim 13$, of Lamastra et al. (2009).

Density Evolution' X-ray luminosity function of Aird et al. (2010), shifted by 1.11 dex following the $L_X/L_{[\mathrm{O\ III}]}$ scaling relation of Lamastra et al. (2009). While it appears that the WISP AGN [O III] luminosity function finds a somewhat higher density of AGN than would be expected from the X-rays, note that there is an intrinsic scatter of 0.6 dex in scaling from the X-ray to [O III] luminosity using Lamastra et al. (2009). This is somewhat reduced if I use the adjustment to the MEx selection suggested by Coil et al. (2015) (downward triangles in Figure 3.15). This may suggest that my sample remains somewhat contaminated by star-forming galaxies, in spite of the care taken here to select a pure sample of AGN. Finally, I do not probe the characteristic luminosity 'knee' inferred from the X-ray luminosity function of Aird et al. (2010). I would likely need a $> 10\times$ larger survey volume in order to place meaningful constraints on the AGN [O III] luminosity function.

3.6 Conclusions

I have selected a sample of AGN at $0.62 < z < 2.93$ from the WISP Survey. Of the 668 [O III] emitters in the 52 WISP survey fields (200 square arcminutes) considered here, I find that roughly 7% have emission-line ratios consistent with ionization by a harder ionizing spectrum than is produced by stars in the local universe. I find in particular a class of dwarf galaxies ($M_* < 10^9$ $\mathrm{M}_\odot$ with extremely high ionization parameters, as measured by O_{32} and $R_{23} > 10$. I argue that these galaxies are similar to the gravitationally-lensed dwarf galaxy sample of Stark et al. (2014), roughly one third of which have UV spectral characteristics of AGN activity. Using the local correlation between host galaxy and stellar mass along with the correlation between [O III] luminosity and AGN bolometric luminosity, I argue that these galaxies, if truly AGN, represent extreme outliers from the local black hole population, as I require either that the black holes comprise a much

greater fraction of their host galaxies' masses or that they are accreting at several times the Eddington limit in order to explain their high [O III] luminosities. Finally, I find that the [O III]-selected AGN luminosity function at $0.62 < z < 2.39$ is marginally higher than the results of X-ray studies, suggesting that my sample may remain $\sim 50\%$ contaminated by star-forming galaxies.

Table 3.1. Photometric filters used for Stellar Population Fitting

Field ID	Filters
17	*g*, *i*, F110W, F140W, Ch1
55	F110W, F140W, Ch1
62	F110W, F140W, Ch1
64	*g*, *i*, F475X, F600LP, F110W, F160W, Ch1
68	F475X, F600LP, F110W, F160W, Ch1
69	F475X, F600LP, F110W, F160W, Ch1
73	F475X, F600LP, F110W, F160W, Ch1
74	*g*, *i*, F475X, F600LP, F110W, F160W, Ch1
76	F475X, F600LP, F110W, F160W, Ch1
78	F110W, F160W, Ch1
79	F475X, F600LP, F110W, F160W, Ch1, Ch2
81	F475X, F600LP, F110W, F160W, Ch1
87	*i*, F475X, F600LP, F110W, F160W, Ch1
94	F475X, F600LP, F110W, F160W, Ch1
96	F606W, F814W, F110W, F160W, Ch1
97	F475X, F600LP, F110W, F160W, Ch1
114	F475X, F600LP, F110W, F160W, Ch1
115	F475X, F600LP, F110W, F160W, Ch1
120	F475X, F600LP, F110W, F160W, Ch1, Ch2
124	F110W, F160W, Ch1
129	F110W, F160W, Ch1
131	F475X, F600LP, F110W, F160W, Ch1

Table 3.1 (cont'd)

Field ID	Filters
132	*g*, *i*, F110W, F160W, Ch1
135	F475X, F600LP, F110W, F160W, Ch1
136	F606W, F814W, F110W, F160W, Ch1
143	F475X, F600LP, F110W, F160W, Ch1
146	F110W, F160W, Ch1
147	F475X, F600LP, F110W, F160W, Ch1
167	F110W, F160W, Ch1
258	F814W, F110W, F160W, Ch1
283	F606W, F814W, F110W, F160W, Ch1
288	*g*, F814W, F110W, F160W, Ch1
291	*g*, F814W, F110W, F160W, Ch1
294	F814W, F110W, F160W, Ch1
295	*g*, F814W, F110W, F160W, Ch1
296	F606W, F814W, F110W, F160W, Ch1
297	*g*, F814W, F110W, F160W, Ch1
298	F606W, F814W, F110W, F160W, Ch1
300	F814W, F110W, F160W, Ch1
302	F606W, F814W, F110W, F160W, Ch1
303	F606W, F814W, F110W, F160W, Ch1
304	F606W, F814W, F110W, F160W, Ch1
307	F606W, F814W, F110W, F160W, Ch1
308	*g*, F814W, F110W, F160W, Ch1

Table 3.1 (cont'd)

Field ID	Filters
309	F606W, F814W, F110W, F160W, Ch1
311	*g*, F814W, F110W, F160W, Ch1
312	F814W, F110W, F160W, Ch1
313	F814W, F110W, F160W, Ch1
314	F606W, F814W, F110W, F160W, Ch1
315	F814W, F110W, F160W, Ch1
317	F814W, F110W, F160W, Ch1
319	F606W, F814W, F110W, F160W

Note. — Imaging in *g* *i* comes from Palomar and WIYN, as described above. The F475X, F600LP, F606W, and F814W filters are from *HST*/WFC3/UVIS. The F110W, F140W and F160W filters are from *HST*/WFC3/IR. The Ch1 and Ch2 filters are from the *Spitzer*/IRAC 3.6μmand 4.5μmchannels.

Table 3.2. Ground-based Optical Follow-up of WISP Fields

Field	Date	Facility	Filters	Seeing
17	2010/10/14	Palomar	g,i	1.2″,1.2″
64	2011/03/05	WIYN	g,i	0.8″, 0.6″
74	2011/03/05	WIYN	g,i	1.0″, 1.0″
87	2011/03/06	WIYN	i	0.8″
132	2013/04/11	Palomar	g,i	1.4″,1.5″
	2013/04/12	Palomar	i	1.4″
288	2014/01/28	Palomar	g	1.2″
291	2014/01/28	Palomar	g	1.5″
295	2014/01/28	Palomar	g	1.4″
296	2014/02/26	Palomar	g	1.6″
308	2014/01/29	Palomar	g	1.3″
311	2013/09/02	Palomar	g	1.5″

Table 3.3. Stellar Population Parameters used by FAST

Parameter	Min. Value	Max. Value	Step Size
$\log \tau$[a]	6.5	10.0	0.5
$\log(age)$[a]	7.6	10.0	0.2
A_V[b]	0.0	3.0	0.1
Z[c]	$[0.0008, 0.0031, 0.0096, 0.019, 0.03]$		

[a]In years

[b]Magnitudes

[c]Metallicity

Table 3.4. The WISP AGN Sample

Galaxy ID	z	$\log_{10} L_{[\mathrm{O\ III}]}$	$\log_{10}(M_*/\mathrm{M}_\odot)$	Selection Method
WISPS64-19	0.896	41.65 ± 0.07	$11.18^{+0.24}_{-0.25}$	M
WISPS64-213	1.322	42.02 ± 0.08	$8.67^{+0.39}_{-0.20}$	B
WISPS73-142	0.970	41.89 ± 0.08	$8.70^{+0.20}_{-0.07}$	B
WISPS76-23	1.355	42.92 ± 0.04	$9.92^{+0.00}_{-0.14}$	M
WISPS78-46	0.880	41.74 ± 0.05	$10.48^{+0.14}_{-0.05}$	M
WISPS79-106	1.925	42.92 ± 0.02	$9.63^{+0.10}_{-0.00}$	M
WISPS87-64	1.538	43.01 ± 0.01	$10.70^{+0.33}_{-0.23}$	M*,R,O
WISPS87-108	2.032	42.71 ± 0.02	$11.00^{+0.18}_{-0.26}$	M*
WISPS94-37	1.133	41.63 ± 0.10	$10.91^{+0.14}_{-1.00}$	M
WISPS94-72	1.834	43.49 ± 0.01	$10.94^{+0.05}_{-0.28}$	M*,O
WISPS96-17	0.956	41.81 ± 0.05	$10.34^{+0.37}_{-0.15}$	M
WISPS96-247	1.341	41.74 ± 0.06	$9.04^{+0.20}_{-0.18}$	B
WISPS96-1014	0.923	41.43 ± 0.04	$9.09^{+0.29}_{-0.30}$	B
WISPS97-19	1.033	41.99 ± 0.06	$10.07^{+0.75}_{-0.11}$	B
WISPS115-19	1.086	42.19 ± 0.06	$10.97^{+0.14}_{-0.72}$	M
WISPS120-59	0.986	41.83 ± 0.05	$9.04^{+0.77}_{-0.06}$	B
WISPS120-349	2.057	42.83 ± 0.02	$10.07^{+0.14}_{-0.32}$	M
WISPS135-22	1.042	41.96 ± 0.04	$10.15^{+0.27}_{-0.04}$	M
WISPS136-48	1.818	42.68 ± 0.02	$10.23^{+0.00}_{-0.05}$	M
WISPS136-236	1.074	41.57 ± 0.05	$8.35^{+0.11}_{-0.15}$	B
WISPS143-14	0.981	41.60 ± 0.08	$11.04^{+0.12}_{-0.41}$	M
WISPS143-56	1.617	43.35 ± 0.01	$9.60^{+0.11}_{-0.05}$	M,O

Table 3.4 (cont'd)

Galaxy ID	z	$\log_{10}\ L_{[\mathrm{O\ III}]}$	$\log_{10}(M_*/\mathrm{M}_\odot)$	Selection Method
WISPS143-97	2.116	42.86 ± 0.02	$10.88^{+0.04}_{-0.05}$	M*
WISPS146-28	1.781	42.40 ± 0.06	$10.83^{+0.18}_{-0.66}$	M
WISPS146-33	1.206	42.44 ± 0.02	$10.07^{+0.47}_{-0.69}$	M
WISPS147-72	2.196	43.14 ± 0.02	$10.63^{+0.26}_{-0.03}$	M
WISPS167-13	0.926	41.58 ± 0.12	$10.89^{+0.26}_{-1.01}$	M
WISPS288-48	0.927	42.01 ± 0.03	$9.34^{+0.16}_{-0.08}$	B
WISPS291-12	1.194	42.86 ± 0.02	$10.72^{+0.00}_{-0.04}$	M
WISPS291-26	1.249	41.97 ± 0.06	$10.80^{+0.57}_{-0.52}$	M
WISPS297-17	0.998	42.16 ± 0.03	$10.57^{+0.11}_{-0.13}$	M,B
WISPS297-112	1.696	42.57 ± 0.03	$10.12^{+0.50}_{-0.37}$	M
WISPS298-154	0.984	41.80 ± 0.02	$8.76^{+0.31}_{-0.39}$	B
WISPS300-76	1.828	42.46 ± 0.04	$10.72^{+0.25}_{-0.12}$	M
WISPS300-145	1.393	42.47 ± 0.02	$8.89^{+0.11}_{-0.19}$	R
WISPS304-79	1.858	42.00 ± 0.07	$10.80^{+0.04}_{-0.79}$	M
WISPS304-101	1.416	42.08 ± 0.02	$9.63^{+0.04}_{-0.05}$	B
WISPS304-349	1.470	42.15 ± 0.03	$8.45^{+0.49}_{-0.38}$	B
WISPS309-157	1.554	42.21 ± 0.02	$8.40^{+0.00}_{-0.02}$	R
WISPS311-25	1.382	42.36 ± 0.04	$11.06^{+0.27}_{-0.10}$	M*
WISPS311-42	1.372	41.80 ± 0.10	$11.45^{+0.21}_{-0.56}$	M
WISPS311-59	1.524	42.22 ± 0.05	$10.80^{+0.36}_{-0.34}$	M
WISPS313-112	1.004	42.16 ± 0.01	$9.04^{+0.13}_{-0.22}$	B
WISPS314-100	2.011	42.96 ± 0.01	$10.86^{+0.04}_{-0.05}$	M*,O

Table 3.4 (cont'd)

Galaxy ID	z	$\log_{10}$ $L_{[\mathrm{O\ III}]}$	$\log_{10}(M_*/\mathrm{M}_\odot)$	Selection Method
WISPS314-268	2.229	42.51 ± 0.03	$10.01^{+0.26}_{-0.50}$	M
WISPS315-57	1.632	42.20 ± 0.04	$10.30^{+0.25}_{-0.58}$	M
WISPS315-146	1.587	42.40 ± 0.02	$9.01^{+0.05}_{-0.39}$	R
WISPS315-154	1.204	42.13 ± 0.02	$9.39^{+0.36}_{-0.28}$	B
WISPS317-36	1.885	42.25 ± 0.08	$10.49^{+0.16}_{-0.12}$	M
WISPS319-122	2.189	42.63 ± 0.04	$10.34^{+0.06}_{-0.50}$	M

Note. — The WISP AGN sample is selected using: The MEx technique (M) of Juneau et al. (2014); (*) denotes that this galaxy is also selected as an AGN under the modification to the MEx technique advocated by Coil et al. (2015); the modified BPT diagram (B); using $R23 > 10$ (R) and the selection criterion of Lamareille et al. (2004); the [O II]/Hβ vs [O III]/Hβ (O) selection criterion of Lamareille et al. (2004).

Table 3.5. The WISP AGN Sample Coordinates

Galaxy ID	RA	Dec	J_{110}	$\log_{10}(M_*/\mathrm{M}_\odot)$
WISP64-19	14:37:30.05	−01:49:09.3	20.61 ± 0.01	$11.18^{0.24}_{0.25}$
WISP64-213	14:37:27.04	−01:49:39.9	24.58 ± 0.08	$8.67^{0.39}_{0.20}$
WISP73-142	14:05:14.99	+46:59:08.3	23.72 ± 0.04	$8.70^{0.20}_{0.07}$
WISP76-23	13:27:20.22	+44:31:11.1	21.16 ± 0.02	$9.92^{0.00}_{0.14}$
WISP78-46	23:28:37.84	+05:10:15.3	21.54 ± 0.01	$10.48^{0.14}_{0.05}$
WISP79-106	01:10:07.01	−02:25:58.5	22.89 ± 0.02	$9.63^{0.10}_{0.00}$
WISP87-64	09:46:47.03	+47:14:54.0	22.24 ± 0.02	$10.70^{0.33}_{0.23}$
WISP87-108	09:46:48.33	+47:14:30.1	23.00 ± 0.03	$11.00^{0.18}_{0.26}$
WISP94-37	22:05:27.11	−00:17:04.6	21.95 ± 0.01	$10.91^{0.14}_{1.00}$
WISP94-72	22:05:23.82	−00:17:11.5	22.87 ± 0.04	$10.94^{0.05}_{0.28}$
WISP96-17	02:09:28.59	−04:43:16.9	21.19 ± 0.01	$10.34^{0.37}_{0.15}$
WISP96-247	02:09:20.34	−04:44:00.6	24.24 ± 0.04	$9.04^{0.20}_{0.18}$
WISP96-1014	02:09:23.25	−04:43:08.2	25.01 ± 0.06	$9.09^{0.29}_{0.30}$
WISP97-19	01:10:03.36	−02:23:32.2	20.77 ± 0.01	$10.07^{0.75}_{0.11}$
WISP115-19	11:18:52.50	+02:17:12.0	20.83 ± 0.02	$10.97^{0.14}_{0.72}$
WISP120-59	13:56:50.97	+17:02:38.2	22.59 ± 0.02	$9.04^{0.77}_{0.06}$
WISP120-349	13:56:52.13	+17:03:24.8	25.47 ± 0.14	$10.07^{0.14}_{0.32}$
WISP135-22	11:22:26.99	+57:51:14.1	21.70 ± 0.01	$10.15^{0.27}_{0.04}$
WISP136-48	12:26:28.50	+05:22:18.2	22.05 ± 0.01	$10.23^{0.00}_{0.05}$
WISP136-236	12:26:27.93	+05:23:23.8	25.01 ± 0.08	$8.35^{0.11}_{0.15}$
WISP143-14	14:02:24.37	+09:46:30.0	20.86 ± 0.01	$11.04^{0.12}_{0.41}$
WISP143-56	14:02:25.84	+09:45:23.7	22.27 ± 0.02	$9.60^{0.11}_{0.05}$

Table 3.5 (cont'd)

Galaxy ID	RA	Dec	J_{110}	$\log_{10}(M_*/\mathrm{M}_\odot)$
WISP143-97	14:02:19.86	+09:46:03.3	23.35 ± 0.03	$10.88^{0.04}_{0.05}$
WISP146-28	02:12:24.12	−07:32:07.0	21.96 ± 0.01	$10.83^{0.18}_{0.66}$
WISP146-33	02:12:27.18	−07:33:11.3	22.21 ± 0.01	$10.07^{0.47}_{0.69}$
WISP147-72	23:58:22.06	−10:14:48.7	22.89 ± 0.03	$10.63^{0.26}_{0.03}$
WISP288-48	09:38:26.10	+07:09:56.1	22.42 ± 0.04	$9.34^{0.16}_{0.08}$
WISP291-12	10:35:22.20	+05:46:43.0	20.21 ± 0.01	$10.72^{0.00}_{0.04}$
WISP291-26	10:35:25.02	+05:48:00.1	21.67 ± 0.03	$10.80^{0.57}_{0.52}$
WISP297-17	11:37:04.72	+01:47:32.7	20.76 ± 0.01	$10.57^{0.11}_{0.13}$
WISP297-112	11:36:58.81	+01:47:36.7	23.35 ± 0.03	$10.12^{0.50}_{0.37}$
WISP298-154	09:21:25.98	+45:07:15.2	23.77 ± 0.09	$8.76^{0.31}_{0.39}$
WISP300-76	08:50:35.76	+44:48:01.4	23.05 ± 0.05	$10.72^{0.25}_{0.12}$
WISP300-145	08:50:24.54	+44:48:08.8	23.91 ± 0.07	$8.89^{0.11}_{0.19}$
WISP304-79	14:28:46.03	+52:39:59.7	23.13 ± 0.06	$10.80^{0.04}_{0.79}$
WISP304-101	14:28:48.51	+52:39:10.8	23.13 ± 0.02	$9.63^{0.04}_{0.05}$
WISP304-349	14:28:57.07	+52:39:57.6	25.36 ± 0.09	$8.45^{0.49}_{0.38}$
WISP309-157	21:39:09.65	−38:26:00.5	24.02 ± 0.05	$8.40^{0.00}_{0.02}$
WISP311-25	16:03:24.52	+57:29:14.5	20.90 ± 0.03	$11.06^{0.27}_{0.10}$
WISP311-42	16:03:20.16	+57:28:58.2	21.85 ± 0.03	$11.45^{0.21}_{0.56}$
WISP311-59	16:03:21.38	+57:29:25.7	22.24 ± 0.05	$10.80^{0.36}_{0.34}$
WISP313-112	02:48:37.05	−30:32:54.6	23.26 ± 0.02	$9.04^{0.13}_{0.22}$
WISP314-100	14:10:21.20	+23:01:15.6	22.97 ± 0.05	$10.86^{0.04}_{0.05}$
WISP314-268	14:10:21.62	+23:00:26.3	24.84 ± 0.12	$10.01^{0.26}_{0.50}$

Table 3.5 (cont'd)

Galaxy ID	RA	Dec	J_{110}	$\log_{10}(M_*/\mathrm{M}_\odot)$
WISP315-57	23:22:52.57	−70:29:46.0	22.49 ± 0.02	$10.30^{0.25}_{0.58}$
WISP315-146	23:23:02.19	−70:28:19.2	23.99 ± 0.04	$9.01^{0.05}_{0.39}$
WISP315-154	23:22:45.04	−70:27:52.0	24.13 ± 0.05	$9.39^{0.36}_{0.28}$
WISP317-36	01:37:17.56	−09:08:19.3	21.75 ± 0.02	$10.49^{0.16}_{0.12}$
WISP319-122	08:53:59.60	+43:53:05.4	23.88 ± 0.06	$10.34^{0.06}_{0.50}$

Note. — Object coordinates and *HST*/WFC3-IR F110W magnitudes for the WISP AGN sample.

Table 3.6. WISE Photometry of WISP AGN Candidates

Source	W1 Vega	W2 Vega	W3 Vega	W4 Vega
WISP311-42	16.400 ± 0.043	14.929 ± 0.040	11.768 ± 0.115	9.112 ± 0.258
WISP64-19	16.024 ± 0.053	15.442 ± 0.108	> 12.148	> 9.005
WISP311-25	16.796 ± 0.052	16.420 ± 0.113	> 13.124	> 9.795
WISP143-14	16.544 ± 0.072	16.720 ± 0.286	> 12.125	> 8.556
WISP167-13	16.839 ± 0.093	16.398 ± 0.242	> 12.023	> 8.926
WISP311-59	17.494 ± 0.085	16.294 ± 0.104	12.688 ± 0.264	> 9.544
WISP291-26	16.907 ± 0.135	16.142 ± 0.250	> 11.909	> 8.800
WISP291-12	15.515 ± 0.047	14.292 ± 0.055	11.258 ± 0.183	> 8.669
WISP297-17	17.235 ± 0.154	> 16.479	> 12.338	> 8.889
WISP317-36	17.252 ± 0.129	16.664 ± 0.290	> 12.647	> 8.980
WISP78-46	16.798 ± 0.104	16.219 ± 0.221	> 11.854	> 8.954

Note. — WISE detections of WISP AGN candidates.

Table 3.7. The WISP $R_{23} > 10$ Galaxy Coordinates

Galaxy ID	RA	Dec	J_{110}	$\log_{10}(M_*/\mathrm{M}_\odot)$
WISP69-260	15:24:08.32	+09:55:50.3	24.60 ± 0.08	$8.70^{0.55}_{0.32}$
WISP79-297	01:10:08.11	−02:24:18.1	25.04 ± 0.08	$8.96^{0.30}_{0.37}$
WISP131-88	10:48:25.87	+13:03:54.5	23.18 ± 0.03	$10.27^{0.27}_{0.28}$
WISP288-78	09:38:29.15	+07:09:37.6	23.26 ± 0.04	$9.26^{0.09}_{0.24}$
WISP302-170	02:44:56.53	−30:02:47.9	24.17 ± 0.05	$8.88^{0.49}_{0.35}$
WISP304-253	14:28:49.69	+52:40:48.5	25.06 ± 0.09	$9.49^{0.15}_{0.30}$
WISP304-304	14:28:49.82	+52:40:44.7	25.22 ± 0.09	$8.89^{0.35}_{0.27}$
WISP307-160	23:59:20.77	−30:34:03.5	24.07 ± 0.05	$9.55^{0.15}_{0.43}$
WISP311-145	16:03:17.59	+57:29:33.3	23.72 ± 0.07	$9.16^{0.08}_{0.14}$
WISP314-242	14:10:20.21	+23:02:07.5	24.53 ± 0.09	$9.66^{0.15}_{0.15}$

Note. — Object coordinates and *HST*/WFC3-IR F110W magnitudes for the WISP galaxies with $R_{23} > 10$ that fell below our 95%-confidence selection cut.

APPENDIX A

The WISP Emission-Line Galaxy Fluxes

Table A.1. Emission Line Fluxes of the WISP Emission-line Galaxies

Galaxy ID	Redshift	[O II] 3726+3729 Flux	Hβ Flux	[O III] 4959+5007 Flux	Hα Flux	[S II] 6717+6731 Flux	Quality Flag
WISP17-17	0.643	···	···	< 70.96	33.46 ± 2.81	13.46 ± 2.51	0
WISP17-22	1.035	···	< 7.64	16.13 ± 4.22	30.16 ± 3.28	< 7.87	0
WISP17-23	0.685	···	< 31.80	< 37.28	33.05 ± 4.88	< 8.37	4
WISP17-25	0.900	···	< 7.82	< 9.61	12.13 ± 2.44	< 5.09	4
WISP17-27	0.642	···	···	< 34.85	28.81 ± 3.61	8.91 ± 2.97	2
WISP17-28	1.042	···	< 5.54	< 6.32	10.93 ± 1.75	< 3.82	4
WISP17-30	1.144	···	< 5.04	< 4.50	33.64 ± 2.85	< 7.27	13
WISP17-37	1.401	< 11.85	< 13.03	< 12.75	30.94 ± 3.58	< 10.30	4
WISP17-40	1.239	< 20.19	6.23 ± 1.87	18.14 ± 3.30	23.55 ± 2.05	< 6.47	0
WISP17-43	1.253	44.77 ± 7.32	···	< 21.93	27.75 ± 1.77	< 3.99	0
WISP17-54	1.227	< 12.01	< 4.63	< 5.41	5.40 ± 1.15	< 1.20	4
WISP17-62	0.668	···	< 25.80	< 19.61	10.02 ± 1.82	< 5.00	4
WISP17-65	0.915	···	< 8.05	< 8.92	13.16 ± 3.36	< 6.89	4
WISP17-66	0.984	···	< 23.16	24.27 ± 8.79	9.47 ± 1.77	< 3.83	9
WISP17-74	1.261	< 12.88	< 7.59	< 7.42	7.91 ± 1.61	6.01 ± 1.53	10
WISP17-84	1.247	< 6.74	···	< 5.67	8.69 ± 0.99	< 2.85	4
WISP17-106	1.251	10.46 ± 3.09	···	< 9.43	12.74 ± 1.50	3.02 ± 1.17	0
WISP17-133	1.163	< 23.65	< 4.51	< 7.03	10.83 ± 1.06	< 3.39	5
WISP17-156	0.992	···	< 3.90	< 5.38	5.27 ± 0.87	< 1.99	4
WISP17-160	0.467	···	···	···	11.44 ± 1.38	3.82 ± 1.00	3
WISP17-186	1.180	< 18.40	···	···	8.60 ± 1.37	3.35 ± 1.13	10
WISP17-1007	1.097	···	2.07 ± 0.76	5.12 ± 1.08	22.59 ± 1.71	2.98 ± 1.28	1
WISP17-2010	1.226	< 7.33	< 2.23	< 3.43	4.18 ± 0.83	< 1.59	4
WISP17-2021	0.667	···	< 10.17	< 19.75	9.71 ± 1.53	< 1.86	12
WISP17-2056	1.105	···	···	< 3.08	3.86 ± 0.98	< 1.41	12
WISP17-2066	1.177	< 9.18	< 3.85	< 2.33	5.57 ± 1.11	< 2.66	12
WISP17-2083	0.495	···	···	···	8.96 ± 1.78	2.71 ± 1.24	2
WISP17-2102	0.629	···	···	< 17.65	7.92 ± 1.80	< 2.88	12
WISP17-2106	1.059	···	< 3.31	3.58 ± 1.56	5.43 ± 1.45	< 6.78	8
WISP55-11	0.371	···	···	···	68.37 ± 10.30	< 26.94	12
WISP55-13	0.352	···	···	···	14.65 ± 4.64	< 4.55	4
WISP55-17	0.536	···	···	···	26.37 ± 4.37	5.49 ± 2.54	2
WISP55-25	0.547	···	···	···	22.82 ± 2.90	< 4.87	4
WISP55-44	0.650	···	< 17.48	< 23.06	9.40 ± 1.41	2.55 ± 0.91	2
WISP55-46	0.608	···	···	···	13.65 ± 1.86	< 3.67	5
WISP55-49	0.510	···	···	···	40.99 ± 2.23	< 4.02	12
WISP55-56	1.114	···	< 4.30	···	11.75 ± 1.48	< 2.51	4
WISP55-59	1.299	< 6.55	< 2.23	< 20.99	9.91 ± 2.14	5.32 ± 2.03	2
WISP55-67	1.062	···	< 4.48	< 3.94	8.59 ± 1.31	< 2.86	12
WISP55-74	1.107	···	< 2.30	< 3.39	8.80 ± 1.42	< 2.79	4
WISP55-138	1.168	< 10.17	< 2.49	< 3.12	26.61 ± 1.77	< 4.52	4
WISP55-178	0.482	···	···	···	13.66 ± 2.19	< 4.52	5
WISP55-220	0.655	···	< 27.45	< 39.39	5.35 ± 1.11	< 2.29	12
WISP55-233	0.475	···	···	···	6.41 ± 1.01	< 2.02	12
WISP55-2035	0.606	···	···	···	10.22 ± 1.11	< 2.62	12
WISP62-10	0.458	···	···	···	57.65 ± 6.62	< 13.52	5
WISP62-11	0.386	···	···	···	20.91 ± 6.07	< 8.83	4
WISP62-14	0.383	···	···	···	60.46 ± 13.29	< 26.05	4

Table A.1 (cont'd)

Galaxy ID	Redshift	[O II] 3726+3729 Flux	Hβ Flux	[O III] 4959+5007 Flux	Hα Flux	[S II] 6717+6731 Flux	Quality Flag
WISP62-20	0.867	···	< 8.20	11.70 ± 4.28	46.69 ± 10.17	< 21.75	0
WISP62-21	0.865	···	< 20.32	< 15.41	52.63 ± 10.55	< 19.95	4
WISP62-22	1.078	···	< 8.38	< 59.60	19.78 ± 5.83	< 12.62	5
WISP62-47	0.559	···	···	···	15.45 ± 1.69	4.08 ± 1.31	2
WISP62-49	0.503	···	···	···	14.19 ± 1.81	< 3.60	4
WISP62-63	0.506	···	···	···	19.41 ± 2.16	< 5.56	4
WISP62-81	0.619	···	···	< 42.30	11.74 ± 1.93	< 1.92	4
WISP62-117	1.321	< 9.53	< 2.19	< 13.35	11.41 ± 2.92	< 5.77	4
WISP62-129	1.306	< 9.29	< 3.97	< 21.07	13.09 ± 2.01	< 3.64	12
WISP62-182	1.093	···	< 9.79	4.09 ± 1.50	15.78 ± 4.11	< 13.41	8
WISP62-204	0.571	···	···	···	15.56 ± 3.14	< 7.69	4
WISP62-217	0.359	···	···	···	17.39 ± 5.34	< 7.25	12
WISP62-236	0.682	···	< 10.33	< 11.22	5.33 ± 1.42	< 4.06	4
WISP62-257	0.714	···	< 12.62	< 63.12	26.54 ± 1.81	< 20.03	12
WISP62-278	0.827	···	< 3.06	< 3.70	26.02 ± 1.34	< 3.05	12
WISP62-2029	1.433	< 7.95	< 8.32	< 8.09	14.65 ± 2.95	< 11.86	4
WISP62-2035	1.218	< 8.69	···	< 3.98	8.48 ± 1.88	< 3.97	12
WISP64-19	0.901	···	< 3.86	15.08 ± 2.37	42.39 ± 5.30	< 8.04	0
WISP64-22	0.676	···	< 73.38	< 354.37	34.77 ± 6.08	< 33.04	5
WISP64-34	1.350	< 5.41	< 3.67	11.82 ± 3.34	20.08 ± 1.88	< 7.27	1
WISP64-35	0.688	···	< 42.40	< 280.52	37.38 ± 4.27	< 35.31	4
WISP64-37	0.618	···	···	···	6.39 ± 1.14	< 2.92	4
WISP64-38	0.993	···	< 3.82	4.84 ± 1.89	6.95 ± 1.93	< 5.36	0
WISP64-41	0.551	···	···	···	30.94 ± 1.71	4.33 ± 1.25	2
WISP64-44	0.906	···	< 4.81	10.85 ± 2.32	< 4.07	< 5.23	12
WISP64-54	0.673	···	< 25.52	49.52 ± 3.74	33.71 ± 3.22	< 8.24	1
WISP64-61	0.946	···	< 12.91	29.45 ± 6.69	15.36 ± 2.19	6.04 ± 2.59	0
WISP64-62	1.286	< 9.36	< 4.67	8.04 ± 2.24	18.69 ± 1.96	7.46 ± 2.01	1
WISP64-63	0.549	···	···	···	10.49 ± 1.87	3.74 ± 1.45	2
WISP64-70	1.439	12.28 ± 3.87	< 7.14	< 9.12	13.89 ± 2.60	< 11.33	1
WISP64-77	1.523	< 3.69	< 4.92	< 7.01	16.59 ± 3.99	···	5
WISP64-78	1.198	< 9.90	···	···	14.46 ± 2.93	4.74 ± 2.17	2
WISP64-91	1.426	4.97 ± 2.05	< 7.42	< 14.12	13.11 ± 2.72	< 6.08	8
WISP64-114	0.966	···	< 6.20	···	19.15 ± 1.95	< 3.46	4
WISP64-143	1.145	···	< 2.76	< 1.31	36.22 ± 5.42	< 10.16	13
WISP64-148	0.488	···	···	···	4.77 ± 1.07	1.89 ± 0.71	2
WISP64-168	0.631	···	···	< 15.25	3.12 ± 0.77	< 2.22	4
WISP64-179	0.677	···	< 9.50	< 7.80	9.25 ± 1.31	< 2.80	5
WISP64-195	1.139	···	···	···	12.02 ± 1.80	< 5.31	4
WISP64-203	1.446	< 3.29	< 2.53	20.40 ± 3.47	4.66 ± 1.71	< 4.80	1
WISP64-206	0.659	···	< 22.23	< 23.66	7.10 ± 1.39	< 2.21	13
WISP64-210	2.183	< 5.39	4.23 ± 1.55	19.45 ± 1.70	···	···	3
WISP64-213	1.323	4.98 ± 1.78	< 4.18	13.35 ± 2.42	4.31 ± 0.81	3.35 ± 1.11	1
WISP64-239	0.936	···	< 5.01	< 8.20	10.03 ± 1.86	< 3.81	5
WISP64-261	1.942	2.19 ± 0.99	1.98 ± 0.97	11.91 ± 1.31	···	···	0
WISP64-1029	1.060	···	< 1.90	9.31 ± 1.12	3.33 ± 1.18	< 1.38	0
WISP64-1031	0.905	···	< 4.12	< 5.79	7.05 ± 2.07	< 2.50	13
WISP64-2021	1.122	···	< 2.42	< 3.02	5.23 ± 1.28	< 3.03	12

Table A.1 (cont'd)

Galaxy ID	Redshift	[O II] 3726+3729 Flux	Hβ Flux	[O III] 4959+5007 Flux	Hα Flux	[S II] 6717+6731 Flux	Quality Flag
WISP64-2051	1.246	< 6.37	< 1.36	< 3.11	4.50 ± 0.82	< 1.99	4
WISP64-2056	1.613	2.72 ± 1.08	< 2.25	20.22 ± 3.78	···	···	1
WISP68-26	0.265	···	···	···	< 28.35	< 15.35	0
WISP68-37	1.255	< 13.65	< 11.68	< 47.04	66.51 ± 6.51	< 22.90	4
WISP68-39	0.564	···	···	···	13.78 ± 4.18	< 2.72	5
WISP68-40	1.090	···	< 2.68	< 3.25	15.48 ± 1.64	3.70 ± 1.51	2
WISP68-42	0.613	···	···	< 46.55	15.82 ± 1.50	3.65 ± 1.19	2
WISP68-43	0.569	···	···	···	5.50 ± 1.36	< 3.79	5
WISP68-48	1.215	< 19.59	6.33 ± 1.69	6.76 ± 1.82	40.40 ± 1.96	144.78 ± 33.29	1
WISP68-50	0.571	···	···	···	9.73 ± 0.53	< 1.00	4
WISP68-52	0.776	···	< 5.85	11.33 ± 2.47	17.33 ± 8.34	< 5.39	1
WISP68-53	1.102	···	< 5.12	< 2.80	10.68 ± 1.64	< 3.24	4
WISP68-54	0.869	···	< 5.17	< 5.84	21.25 ± 2.90	< 3.30	5
WISP68-55	0.707	···	< 7.30	9.66 ± 3.33	6.92 ± 1.78	< 25.62	1
WISP68-63	0.347	···	···	···	12.58 ± 1.42	2.72 ± 1.18	2
WISP68-66	0.920	···	< 11.48	< 14.44	17.79 ± 2.73	< 11.02	4
WISP68-67	0.505	···	···	···	7.78 ± 1.61	< 2.94	12
WISP68-68	1.140	···	< 5.07	11.49 ± 1.85	8.32 ± 2.04	< 2.96	8
WISP68-76	1.099	···	< 3.06	< 6.35	8.16 ± 1.50	< 2.47	4
WISP68-93	0.958	···	< 3.93	< 4.68	10.63 ± 1.55	< 3.48	5
WISP68-96	1.271	< 6.63	< 2.50	< 6.39	8.77 ± 2.45	< 5.66	4
WISP68-108	0.982	···	3.22 ± 1.36	18.07 ± 2.44	11.21 ± 1.22	3.12 ± 1.50	0
WISP68-124	0.968	···	< 1.82	< 1.85	5.39 ± 1.37	< 2.51	5
WISP68-126	1.312	< 4.75	< 6.95	13.77 ± 6.75	6.08 ± 1.24	< 2.12	1
WISP68-147	1.017	···	< 1.49	< 4.03	6.64 ± 1.50	< 3.83	4
WISP68-167	1.131	···	3.72 ± 1.36	15.50 ± 1.25	5.52 ± 0.57	< 1.07	8
WISP68-172	2.140	< 2.41	< 1.98	4.14 ± 1.06	···	···	12
WISP68-175	0.615	···	···	< 19.40	4.52 ± 0.77	< 2.56	4
WISP68-187	0.483	···	···	···	7.48 ± 2.23	< 2.92	4
WISP68-217	1.252	< 4.27	< 1.04	< 8.01	3.12 ± 0.76	< 1.83	4
WISP68-237	0.667	···	< 9.45	< 5.23	10.07 ± 0.94	< 1.94	12
WISP68-252	1.353	< 4.81	3.48 ± 1.05	10.78 ± 1.96	3.46 ± 0.67	< 1.42	1
WISP68-254	0.378	···	···	···	36.46 ± 1.11	< 1.51	5
WISP68-1027	1.056	···	< 1.34	16.80 ± 1.93	5.68 ± 0.69	< 1.56	1
WISP68-1046	0.463	···	···	···	5.31 ± 1.29	< 3.23	12
WISP68-1060	0.465	···	···	···	24.13 ± 0.95	< 1.73	4
WISP68-2037	1.759	···	4.50 ± 1.15	20.57 ± 1.38	···	···	2
WISP68-2041	0.679	···	< 6.77	···	38.61 ± 1.86	< 7.44	4
WISP68-2145	0.687	···	< 8.61	< 6.09	2.88 ± 0.66	< 3.77	4
WISP69-5	0.529	···	···	···	45.31 ± 6.10	< 11.71	4
WISP69-9	0.619	···	···	< 51.57	17.94 ± 2.91	< 5.98	4
WISP69-10	0.521	···	···	···	18.77 ± 3.63	< 6.72	12
WISP69-12	0.615	···	···	< 152.45	58.09 ± 5.88	21.18 ± 4.95	2
WISP69-15	0.523	···	···	···	32.96 ± 3.28	9.06 ± 4.14	2
WISP69-17	0.868	···	···	···	15.08 ± 7.49	···	1
WISP69-19	0.406	···	···	···	55.09 ± 8.91	< 22.57	5
WISP69-35	0.912	···	< 3.27	···	7.58 ± 2.26	< 4.92	12
WISP69-43	1.066	···	< 10.86	< 6.24	26.15 ± 3.20	< 6.82	4

Table A.1 (cont'd)

Galaxy ID	Redshift	[O II] 3726+3729 Flux	Hβ Flux	[O III] 4959+5007 Flux	Hα Flux	[S II] 6717+6731 Flux	Quality Flag
WISP69-61	1.082	···	< 3.63	< 4.58	7.03 ± 1.59	< 2.28	12
WISP69-65	0.379	···	···	···	18.10 ± 2.70	< 2.62	0
WISP69-66	0.955	···	< 6.39	< 7.76	20.13 ± 5.15	< 9.12	12
WISP69-73	1.447	12.92 ± 4.33	< 6.46	15.46 ± 4.12	10.07 ± 3.25	< 11.53	8
WISP69-79	0.632	···	···	< 28.61	11.16 ± 2.31	< 4.53	5
WISP69-84	0.483	···	···	···	13.88 ± 2.04	< 3.27	5
WISP69-91	0.967	···	< 2.36	4.85 ± 1.62	16.71 ± 3.09	3.84 ± 1.30	0
WISP69-94	1.441	7.85 ± 1.82	18.19 ± 6.71	9.44 ± 3.01	13.73 ± 3.99	< 18.12	1
WISP69-97	0.498	···	···	···	18.81 ± 1.60	< 3.00	4
WISP69-98	0.771	···	< 20.03	< 18.86	26.94 ± 6.17	< 8.70	5
WISP69-102	1.664	5.24 ± 1.78	4.25 ± 1.19	23.09 ± 1.25	···	···	1
WISP69-105	0.370	···	···	···	8.08 ± 2.68	< 4.63	12
WISP69-119	0.864	···	< 7.04	9.52 ± 2.11	9.90 ± 1.86	< 2.17	1
WISP69-136	1.499	< 3.35	< 4.52	< 4.36	9.95 ± 2.13	15.90 ± 4.76	3
WISP69-148	1.905	3.61 ± 1.05	< 2.06	12.23 ± 0.95	···	···	0
WISP69-172	0.619	···	···	< 30.37	6.01 ± 1.24	< 2.44	4
WISP69-177	0.327	···	···	···	17.38 ± 3.00	< 5.02	4
WISP69-187	0.969	···	< 7.39	5.84 ± 2.69	13.09 ± 2.94	< 7.03	8
WISP69-193	1.473	< 4.69	< 2.88	< 3.93	6.34 ± 1.64	···	5
WISP69-224	1.130	···	< 5.11	< 8.79	8.94 ± 1.92	< 3.74	5
WISP69-253	1.135	···	< 2.27	12.46 ± 2.01	5.40 ± 1.38	< 3.73	1
WISP69-260	1.723	4.24 ± 1.78	< 1.89	10.78 ± 0.83	···	···	0
WISP69-300	0.617	···	···	···	4.45 ± 1.04	< 2.73	13
WISP69-328	0.401	···	···	···	4.66 ± 1.40	< 3.39	12
WISP69-331	1.973	< 3.72	< 5.51	9.85 ± 1.34	···	···	4
WISP69-2022	1.280	< 5.09	< 2.69	< 2.56	4.76 ± 0.86	< 1.47	4
WISP69-2051	0.437	···	···	···	7.67 ± 1.62	< 3.06	4
WISP73-16	0.392	···	···	···	69.50 ± 11.35	< 20.29	5
WISP73-24	0.322	···	···	···	48.96 ± 8.20	< 14.84	5
WISP73-27	0.597	···	···	···	72.06 ± 4.98	11.34 ± 4.61	2
WISP73-29	1.103	···	< 5.96	< 4.53	9.18 ± 2.02	< 4.60	4
WISP73-30	1.024	···	< 6.60	< 7.14	10.29 ± 2.54	< 4.49	4
WISP73-32	0.606	···	···	< 61.68	10.96 ± 2.29	11.79 ± 3.77	0
WISP73-33	0.607	···	···	< 14.91	39.22 ± 2.16	7.84 ± 1.66	2
WISP73-37	0.361	···	···	···	11.78 ± 3.60	< 17.45	12
WISP73-40	1.019	···	< 3.11	4.49 ± 1.96	16.86 ± 3.48	< 4.18	8
WISP73-42	0.884	···	< 19.04	27.04 ± 8.17	40.30 ± 6.28	< 9.08	1
WISP73-44	0.917	···	< 3.12	< 4.87	18.00 ± 3.76	< 2.65	5
WISP73-45	1.324	27.51 ± 7.26	< 12.22	< 5.63	38.87 ± 1.53	3.97 ± 1.34	0
WISP73-49	0.482	···	···	···	9.23 ± 1.71	< 2.03	4
WISP73-51	0.790	···	< 5.10	8.73 ± 2.42	16.31 ± 8.11	< 4.91	1
WISP73-53	0.300	···	···	···	44.98 ± 8.91	< 12.56	13
WISP73-59	1.091	···	< 6.74	10.45 ± 2.54	26.51 ± 2.45	3.50 ± 1.54	1
WISP73-65	0.898	···	< 6.09	12.31 ± 2.82	20.13 ± 9.67	< 5.31	1
WISP73-67	1.230	< 40.01	···	< 74.28	20.94 ± 3.51	< 5.17	5
WISP73-69	0.886	···	< 5.92	34.66 ± 7.11	18.52 ± 5.76	< 3.44	0
WISP73-70	1.415	< 5.28	< 7.83	21.48 ± 5.00	8.69 ± 1.25	< 7.72	0
WISP73-72	0.655	···	< 729.42	< 959.54	17.74 ± 5.06	< 8.23	4

Table A.1 (cont'd)

Galaxy ID	Redshift	[O II] 3726+3729 Flux	Hβ Flux	[O III] 4959+5007 Flux	Hα Flux	[S II] 6717+6731 Flux	Quality Flag
WISP73-75	0.662	···	< 18.09	< 17.24	15.38 ± 2.81	< 3.75	5
WISP73-86	1.088	···	< 3.59	< 3.21	10.54 ± 2.38	< 4.26	4
WISP73-88	1.747	7.66 ± 1.67	5.80 ± 2.33	7.45 ± 1.59	···	···	0
WISP73-94	1.694	6.55 ± 1.10	< 3.61	8.46 ± 2.08	···	···	0
WISP73-101	1.352	< 7.51	< 39.50	< 5.32	8.41 ± 1.21	< 2.53	4
WISP73-108	1.221	< 5.98	< 2.58	< 3.17	6.89 ± 0.94	2.59 ± 0.88	2
WISP73-121	0.344	···	···	···	15.17 ± 4.24	< 8.05	5
WISP73-124	1.311	< 8.40	< 4.33	< 51.35	7.27 ± 1.31	< 2.16	4
WISP73-125	0.498	···	···	···	7.23 ± 1.66	< 4.06	5
WISP73-129	1.502	< 4.01	< 6.40	< 4.38	15.21 ± 3.24	···	13
WISP73-133	0.369	···	···	···	10.26 ± 2.87	< 5.14	12
WISP73-139	1.094	···	< 3.62	< 4.85	8.61 ± 1.47	< 2.49	1
WISP73-140	0.605	···	···	< 47.93	12.86 ± 2.60	9.66 ± 3.46	3
WISP73-142	0.970	···	< 2.97	21.47 ± 3.79	7.87 ± 1.16	3.74 ± 1.05	0
WISP73-144	1.328	< 4.02	< 5.85	< 5.07	5.66 ± 1.16	< 2.21	4
WISP73-148	1.811	3.55 ± 1.35	< 4.57	10.15 ± 1.87	···	···	0
WISP73-154	1.310	8.10 ± 3.54	< 11.29	30.91 ± 13.06	8.54 ± 1.54	< 3.27	1
WISP73-162	1.092	···	···	< 3.50	6.34 ± 1.20	< 13.54	12
WISP73-192	0.457	···	···	···	16.09 ± 3.70	< 5.06	12
WISP73-248	0.925	···	< 3.19	11.82 ± 1.58	6.45 ± 1.18	< 3.54	0
WISP73-249	0.611	···	···	···	11.88 ± 1.19	< 1.43	5
WISP73-251	1.098	···	< 2.57	< 3.13	8.36 ± 2.11	< 8.11	4
WISP73-264	1.332	< 8.40	< 6.16	< 15.94	20.94 ± 1.76	< 6.42	4
WISP73-269	2.216	< 3.03	< 1.53	16.16 ± 2.57	···	···	4
WISP73-276	0.872	···	< 4.02	21.99 ± 2.94	< 4.77	< 4.67	5
WISP73-283	1.382	< 3.71	< 5.70	< 5.30	20.75 ± 1.37	< 4.06	5
WISP73-350	1.917	< 1.78	< 1.59	5.94 ± 1.05	···	···	4
WISP73-367	1.328	< 5.27	< 3.30	< 16.66	4.68 ± 0.88	< 2.12	4
WISP73-1012	1.770	< 1.50	< 1.90	6.35 ± 1.10	···	···	4
WISP73-1017	1.004	···	< 3.18	< 2.48	5.58 ± 1.63	< 2.25	13
WISP73-2018	1.307	< 11.01	< 15.22	< 1473.78	6.91 ± 2.30	< 5.18	12
WISP73-2073	0.868	···	< 3.23	< 2.85	5.08 ± 1.67	< 2.78	13
WISP74-19	0.291	···	···	···	41.08 ± 9.00	< 8.51	13
WISP74-22	0.664	···	< 427.16	< 419.80	40.36 ± 7.22	< 16.86	4
WISP74-23	0.458	···	···	···	38.70 ± 3.59	15.33 ± 6.65	2
WISP74-26	0.305	···	···	···	29.01 ± 7.13	< 10.97	5
WISP74-28	0.996	···	< 7.77	< 10.59	52.58 ± 4.00	< 11.22	4
WISP74-29	0.458	···	···	···	14.80 ± 4.90	< 5.54	4
WISP74-31	0.618	···	···	< 93.53	29.11 ± 2.08	26.82 ± 7.48	2
WISP74-32	0.662	···	< 46.52	< 44.34	20.60 ± 2.12	< 5.74	5
WISP74-36	0.988	···	< 11.98	< 12.81	39.43 ± 4.82	< 8.17	4
WISP74-41	0.695	···	< 23.21	< 19.85	15.26 ± 3.78	< 43.53	5
WISP74-42	0.662	···	< 33.59	< 41.22	20.12 ± 3.33	< 7.02	4
WISP74-43	0.665	···	< 15.17	< 13.76	11.22 ± 2.21	< 3.39	5
WISP74-49	1.274	18.77 ± 7.54	< 10.56	43.26 ± 17.18	15.90 ± 2.28	< 7.42	1
WISP74-55	0.542	···	···	···	9.47 ± 2.70	< 6.63	4
WISP74-56	1.310	< 8.76	< 5.45	< 37.56	9.06 ± 1.95	< 3.55	4
WISP74-59	0.665	···	< 54.57	< 184.64	19.04 ± 4.78	< 10.76	12

Table A.1 (cont'd)

Galaxy ID	Redshift	[O II] 3726+3729 Flux	Hβ Flux	[O III] 4959+5007 Flux	Hα Flux	[S II] 6717+6731 Flux	Quality Flag
WISP74-72	1.096	···	< 9.00	< 15.69	15.69 ± 3.06	< 6.26	4
WISP74-74	1.254	< 10.05	< 2.84	< 3.98	20.74 ± 2.62	< 2.49	4
WISP74-103	1.001	···	< 3.35	6.95 ± 2.72	8.35 ± 2.12	< 5.46	8
WISP74-111	0.592	···	···	···	10.35 ± 1.85	< 3.11	4
WISP74-130	1.083	···	< 4.58	< 7.08	11.22 ± 2.88	< 5.34	4
WISP74-134	1.164	< 14.82	< 3.90	< 7.28	13.74 ± 2.27	< 4.05	4
WISP74-135	1.173	< 35.93	< 6.82	< 4.11	15.31 ± 2.45	< 4.73	4
WISP74-153	0.646	···	···	< 138.82	10.59 ± 2.93	< 6.07	5
WISP74-176	0.563	···	···	···	4.91 ± 1.44	< 2.89	4
WISP74-177	0.623	···	···	···	16.48 ± 1.26	< 2.04	4
WISP74-185	0.851	···	< 2.67	< 5.74	9.46 ± 2.21	< 3.29	4
WISP74-191	0.394	···	···	···	18.81 ± 1.60	< 2.97	4
WISP74-196	0.614	···	···	···	5.86 ± 1.39	< 2.21	4
WISP74-205	1.263	< 7.73	< 3.33	< 4.92	12.49 ± 1.78	< 4.31	5
WISP74-208	1.303	< 4.42	< 1.65	< 33.69	6.79 ± 1.32	< 2.30	4
WISP74-1028	0.648	···	···	< 17.70	5.41 ± 1.46	< 9.88	12
WISP74-1031	1.325	< 4.70	< 2.03	< 7.80	7.41 ± 1.96	< 4.16	12
WISP74-2039	1.924	< 2.96	< 7.55	13.45 ± 2.61	···	···	4
WISP74-2047	1.488	5.00 ± 2.43	< 5.93	< 10.30	12.61 ± 2.08	···	0
WISP74-2052	1.912	8.98 ± 3.45	< 7.38	14.31 ± 3.47	···	···	1
WISP74-2113	1.092	···	< 2.96	< 4.87	11.55 ± 2.59	< 4.68	4
WISP76-15	0.709	···	< 25.57	< 47.10	17.17 ± 2.70	< 11.98	4
WISP76-16	0.323	···	···	···	72.02 ± 4.37	20.33 ± 3.01	0
WISP76-17	0.694	···	< 59.91	< 50.42	19.49 ± 5.49	< 12.16	0
WISP76-20	1.329	< 10.78	< 31.99	< 36.67	36.89 ± 3.24	10.17 ± 3.20	2
WISP76-22	0.705	···	< 15.30	10.14 ± 4.35	12.19 ± 3.55	< 57.61	9
WISP76-23	1.355	59.51 ± 6.22	12.14 ± 4.65	100.87 ± 8.51	77.32 ± 2.75	14.72 ± 3.62	1
WISP76-39	1.203	< 20.58	< 5.67	< 6.29	18.30 ± 4.24	< 8.06	5
WISP76-42	0.893	···	< 4.24	< 9.12	7.97 ± 1.96	< 3.55	4
WISP76-53	0.518	···	···	···	8.51 ± 1.57	< 3.39	12
WISP76-58	0.726	···	< 9.71	57.81 ± 13.80	17.83 ± 2.52	< 7.57	8
WISP76-72	0.840	···	< 10.47	14.35 ± 5.18	15.39 ± 2.79	< 6.21	0
WISP76-73	0.302	···	···	···	8.18 ± 2.32	< 4.64	5
WISP76-75	1.000	···	< 4.83	···	4.58 ± 1.47	< 4.07	4
WISP76-76	1.268	< 8.25	< 5.19	< 12.12	11.31 ± 2.00	< 4.22	12
WISP76-78	0.948	···	< 4.33	9.92 ± 2.26	7.64 ± 1.90	2.53 ± 0.80	1
WISP76-86	0.376	···	···	···	8.43 ± 2.12	< 5.05	8
WISP76-101	0.716	···	< 12.49	< 16.09	8.78 ± 2.55	< 7.64	4
WISP76-106	0.703	···	< 11.37	10.41 ± 2.45	15.43 ± 4.40	< 95.09	9
WISP76-114	1.325	7.10 ± 1.77	< 2.45	< 12.09	7.45 ± 1.37	< 2.84	1
WISP76-132	1.163	< 34.77	< 2.53	5.61 ± 1.83	3.36 ± 0.90	< 1.87	8
WISP76-208	1.538	< 2.82	3.17 ± 1.49	10.53 ± 2.06	···	···	10
WISP76-209	0.308	···	···	···	15.99 ± 3.40	3.78 ± 1.27	3
WISP76-213	0.456	···	···	···	10.56 ± 1.61	3.75 ± 1.44	2
WISP76-232	1.042	···	···	< 8.21	7.85 ± 1.68	< 2.99	12
WISP76-234	0.677	···	< 9.87	9.45 ± 3.46	7.30 ± 0.99	< 3.12	9
WISP76-260	1.493	< 2.71	< 4.76	< 4.66	9.78 ± 2.94	···	5
WISP76-283	0.449	···	···	···	8.61 ± 2.05	< 2.57	5

Table A.1 (cont'd)

Galaxy ID	Redshift	[O II] 3726+3729 Flux	Hβ Flux	[O III] 4959+5007 Flux	Hα Flux	[S II] 6717+6731 Flux	Quality Flag
WISP76-296	1.908	< 1.45	< 2.29	14.87 ± 1.79	···	···	5
WISP76-311	0.290	···	···	···	16.03 ± 3.21	< 5.70	5
WISP76-312	1.360	< 2.71	< 6.17	< 7.48	13.77 ± 1.26	1.45 ± 0.68	2
WISP76-1008	1.051	···	< 2.43	< 4.01	6.73 ± 1.77	< 3.26	4
WISP76-2001	0.385	···	···	···	54.42 ± 4.41	15.44 ± 3.84	11
WISP76-2073	1.167	< 25.01	< 1.65	< 2.50	5.34 ± 1.22	< 2.81	12
WISP78-7	0.365	···	···	···	71.31 ± 9.22	< 21.70	12
WISP78-8	0.595	···	···	···	46.81 ± 3.95	< 6.60	4
WISP78-30	0.563	···	···	···	14.16 ± 1.62	< 2.90	4
WISP78-31	1.114	···	< 7.52	< 11.52	36.17 ± 5.74	< 5.61	4
WISP78-37	0.574	···	···	···	34.45 ± 4.82	< 9.13	4
WISP78-38	0.596	···	···	···	24.28 ± 2.83	9.30 ± 2.89	2
WISP78-41	0.510	···	···	···	17.56 ± 1.97	< 3.97	5
WISP78-43	0.586	···	···	···	11.96 ± 1.57	< 4.02	12
WISP78-46	0.884	···	< 4.79	19.17 ± 2.40	22.53 ± 2.19	< 4.81	0
WISP78-49	0.569	···	···	···	15.48 ± 2.32	6.64 ± 3.08	0
WISP78-50	0.569	···	···	···	16.37 ± 1.37	< 3.26	4
WISP78-52	0.796	···	< 9.42	< 22.45	36.11 ± 5.14	< 13.96	13
WISP78-58	0.713	···	< 5.21	< 4.19	10.55 ± 0.95	< 38.81	12
WISP78-67	0.557	···	···	···	29.23 ± 1.61	4.20 ± 1.13	0
WISP78-71	1.226	< 13.55	< 3.20	18.14 ± 2.00	19.77 ± 1.48	< 4.92	0
WISP78-81	1.227	< 7.01	< 3.56	< 5.69	18.35 ± 1.48	< 3.00	4
WISP78-85	0.650	···	< 312.13	< 861.77	28.81 ± 5.06	< 9.56	12
WISP78-88	1.099	···	4.56 ± 1.29	< 2.60	19.70 ± 1.76	< 3.62	0
WISP78-90	0.987	···	5.44 ± 1.12	45.12 ± 2.23	44.61 ± 1.82	5.60 ± 1.29	0
WISP78-99	0.648	···	···	< 21.48	8.84 ± 1.23	< 1.69	13
WISP78-109	1.232	< 5.52	< 2.72	< 4.21	6.50 ± 1.43	< 3.19	4
WISP78-112	0.679	···	< 21.48	< 20.06	7.59 ± 1.42	< 3.53	12
WISP78-113	1.069	···	< 7.87	< 6.04	17.69 ± 2.54	< 18.14	4
WISP78-124	0.675	···	< 23.88	< 61.41	16.67 ± 2.76	< 33.74	12
WISP78-129	1.049	···	< 3.07	< 2.32	6.18 ± 1.46	< 2.37	4
WISP78-150	1.474	13.58 ± 2.82	< 6.15	12.58 ± 3.84	15.66 ± 2.10	···	0
WISP78-153	0.544	···	···	···	19.27 ± 2.62	< 2.62	13
WISP78-167	1.488	7.07 ± 3.34	7.78 ± 1.67	···	···	···	0
WISP78-268	1.227	< 3.76	< 1.10	< 1.71	3.81 ± 0.44	< 1.95	12
WISP78-2091	0.677	···	< 17.32	< 28.35	13.57 ± 1.24	6.02 ± 2.18	2
WISP78-2092	0.680	···	< 17.77	< 13.15	4.35 ± 0.99	< 3.77	12
WISP79-8	1.072	···	81.57 ± 11.48	72.12 ± 8.16	395.36 ± 8.45	25.42 ± 8.23	0
WISP79-11	0.310	···	···	···	27.99 ± 6.04	< 9.01	5
WISP79-14	0.403	···	···	···	42.80 ± 10.21	< 15.19	4
WISP79-15	0.441	···	···	···	51.94 ± 4.47	15.20 ± 5.81	2
WISP79-17	0.822	···	< 4.01	< 4.89	50.72 ± 14.63	< 5.09	4
WISP79-18	0.755	···	11.78 ± 5.48	17.62 ± 4.91	71.88 ± 18.91	< 11.61	1
WISP79-27	1.077	···	< 5.55	···	19.06 ± 2.43	< 2.88	4
WISP79-28	0.828	···	< 4.44	9.94 ± 1.52	18.47 ± 1.74	< 3.14	0
WISP79-32	1.086	···	< 3.17	< 4.87	14.56 ± 2.08	< 4.82	4
WISP79-35	0.972	···	< 4.92	< 4.13	9.08 ± 1.65	7.06 ± 3.50	2
WISP79-36	1.133	···	< 3.98	< 3.22	9.48 ± 1.33	···	4

Table A.1 (cont'd)

Galaxy ID	Redshift	[O II] 3726+3729 Flux	Hβ Flux	[O III] 4959+5007 Flux	Hα Flux	[S II] 6717+6731 Flux	Quality Flag
WISP79-38	1.071	···	< 3.86	< 5.09	15.06 ± 1.58	< 3.64	4
WISP79-44	1.093	···	< 5.48	< 13.88	30.93 ± 3.50	< 5.47	4
WISP79-48	0.621	···	···	< 10.30	20.84 ± 1.45	5.08 ± 1.44	2
WISP79-49	0.959	···	< 3.62	< 3.57	13.84 ± 3.19	< 5.44	5
WISP79-51	1.217	< 13.35	···	< 76.91	13.98 ± 2.23	< 3.64	4
WISP79-55	1.187	< 12.32	< 21.15	···	26.49 ± 1.81	< 8.91	5
WISP79-60	0.655	···	< 13.56	< 11.22	15.50 ± 2.03	< 2.09	4
WISP79-79	0.660	···	< 9.16	< 10.29	9.35 ± 0.77	4.04 ± 0.97	0
WISP79-82	1.069	···	< 6.94	14.48 ± 1.73	13.47 ± 2.00	4.78 ± 2.02	0
WISP79-90	1.233	< 4.83	< 1.42	< 2.09	11.56 ± 1.03	3.12 ± 1.16	0
WISP79-94	0.988	···	< 2.70	< 4.70	43.40 ± 2.41	< 7.20	4
WISP79-98	1.407	< 3.19	< 6.36	< 4.79	9.80 ± 3.17	< 2.07	12
WISP79-104	0.581	···	···	···	5.49 ± 1.13	< 2.65	4
WISP79-106	1.925	< 1.69	3.88 ± 1.04	41.73 ± 1.45	···	···	2
WISP79-108	0.406	···	···	···	18.68 ± 1.02	< 2.09	0
WISP79-118	1.086	···	5.04 ± 1.99	10.78 ± 1.82	7.36 ± 2.22	< 2.28	1
WISP79-121	1.150	···	< 1.94	< 4.29	9.23 ± 1.48	< 3.40	5
WISP79-122	0.552	···	···	···	6.28 ± 1.00	< 2.52	13
WISP79-123	0.661	···	< 8.25	< 8.07	7.37 ± 1.18	< 2.09	4
WISP79-124	1.608	5.42 ± 1.20	1.68 ± 0.78	7.30 ± 1.11	···	···	0
WISP79-125	1.911	3.45 ± 0.68	< 2.18	6.99 ± 1.16	···	···	0
WISP79-129	1.543	3.29 ± 0.93	< 6.43	< 7.32	···	···	0
WISP79-133	1.600	5.00 ± 0.91	4.32 ± 1.42	5.27 ± 1.22	···	···	0
WISP79-136	1.106	···	···	< 19.51	6.01 ± 0.96	35.71 ± 16.10	2
WISP79-138	1.613	4.14 ± 1.53	< 2.42	9.40 ± 1.25	···	···	0
WISP79-149	1.179	< 5.73	< 2.09	< 3.75	7.33 ± 1.11	< 1.56	4
WISP79-154	1.414	< 4.41	< 4.36	16.07 ± 1.65	4.95 ± 0.97	< 3.08	1
WISP79-162	1.060	···	< 2.78	< 2.81	4.48 ± 1.09	< 2.09	4
WISP79-168	0.492	···	···	···	9.59 ± 1.35	< 2.91	5
WISP79-178	0.408	···	···	···	6.75 ± 1.07	< 1.77	4
WISP79-190	1.620	4.62 ± 0.89	< 6.60	< 7.02	···	···	0
WISP79-193	0.600	···	···	···	10.72 ± 0.79	< 1.79	5
WISP79-211	1.197	< 4.98	< 1.55	< 1.55	2.98 ± 0.75	< 1.98	4
WISP79-215	1.299	< 9.55	< 5.06	< 829.22	19.61 ± 2.65	< 6.04	13
WISP79-225	1.028	···	< 1.35	< 1.44	3.78 ± 0.62	< 0.94	4
WISP79-226	0.940	···	< 1.21	< 2.05	4.76 ± 0.90	< 1.41	12
WISP79-297	1.911	1.88 ± 0.39	< 1.36	10.16 ± 0.75	···	···	0
WISP79-317	0.982	···	< 1.70	< 2.64	11.46 ± 1.20	< 2.07	4
WISP79-319	1.258	< 2.91	< 2.69	< 9.51	3.81 ± 1.00	< 2.13	12
WISP79-1017	1.255	< 2.47	< 1.85	8.66 ± 2.12	3.14 ± 0.83	< 1.24	0
WISP79-1042	1.017	···	< 1.86	< 2.58	4.56 ± 0.97	< 2.08	4
WISP79-1047	0.605	···	···	···	2.14 ± 0.56	< 1.05	13
WISP79-2001	1.003	···	< 5.38	< 10.96	11.99 ± 2.31	< 2.98	4
WISP79-2021	0.451	···	···	···	4.37 ± 0.81	< 1.44	4
WISP79-2028	2.071	< 0.55	< 1.21	7.21 ± 0.61	···	···	4
WISP81-16	0.852	···	< 5.45	< 8.93	11.19 ± 2.16	< 3.36	12
WISP81-22	0.798	···	< 9.28	< 21.04	41.76 ± 6.31	< 6.31	5
WISP81-30	1.363	< 2.66	< 5.86	< 6.38	7.45 ± 1.35	2.32 ± 0.96	2

Table A.1 (cont'd)

Galaxy ID	Redshift	[O II] 3726+3729 Flux	Hβ Flux	[O III] 4959+5007 Flux	Hα Flux	[S II] 6717+6731 Flux	Quality Flag
WISP81-31	0.704	···	< 15.58	< 14.30	9.71 ± 2.26	< 110.13	4
WISP81-32	1.065	···	< 12.47	< 2.54	11.54 ± 2.05	< 5.06	4
WISP81-34	0.644	···	···	< 19.13	8.15 ± 1.54	3.81 ± 1.77	3
WISP81-38	0.979	···	< 4.27	< 5.82	21.97 ± 2.04	5.07 ± 1.54	3
WISP81-40	1.095	···	< 4.03	< 7.33	11.66 ± 1.50	< 3.02	4
WISP81-41	1.330	< 4.69	< 6.62	< 7.97	6.61 ± 1.65	< 3.50	4
WISP81-42	1.167	< 518.70	< 72.55	< 84.22	13.44 ± 3.04	51.23 ± 22.48	2
WISP81-43	0.957	···	< 5.48	< 6.08	11.19 ± 3.22	< 6.53	4
WISP81-44	1.072	···	7.77 ± 1.47	8.61 ± 3.35	8.64 ± 1.91	< 3.68	8
WISP81-46	0.748	···	< 5.93	6.25 ± 3.10	20.83 ± 4.87	< 12.03	8
WISP81-53	0.533	···	···	···	15.64 ± 0.96	4.93 ± 1.04	2
WISP81-54	1.181	< 12.88	< 4.25	< 3.18	7.13 ± 1.34	< 0.73	4
WISP81-55	0.827	···	< 3.32	< 4.66	11.75 ± 1.52	< 2.63	4
WISP81-58	0.308	···	···	···	27.49 ± 1.17	4.85 ± 1.09	1
WISP81-62	0.523	···	···	···	9.86 ± 2.34	< 4.19	4
WISP81-63	1.064	···	< 4.38	6.07 ± 2.09	10.98 ± 2.68	< 5.44	8
WISP81-73	1.360	< 3.89	< 17.27	< 12.63	11.21 ± 1.06	< 2.86	4
WISP81-75	1.246	< 7.98	< 3.27	8.44 ± 3.58	8.56 ± 1.34	< 2.61	0
WISP81-76	1.333	< 3.94	< 1.95	< 5.21	8.53 ± 1.22	< 2.68	4
WISP81-77	1.354	6.31 ± 1.87	< 8.11	< 7.00	8.03 ± 1.46	< 2.90	0
WISP81-83	1.693	···	6.48 ± 1.95	28.59 ± 1.69	···	···	2
WISP81-88	1.309	< 4.27	< 2.09	4.12 ± 1.54	11.14 ± 2.79	< 5.97	9
WISP81-90	0.502	···	···	···	15.76 ± 1.20	6.66 ± 3.18	10
WISP81-97	0.627	···	···	···	4.18 ± 0.55	< 1.50	4
WISP81-103	0.772	···	< 5.67	< 5.10	14.29 ± 3.13	< 5.08	5
WISP81-108	1.313	< 4.69	< 24.19	18.32 ± 2.76	13.65 ± 3.25	< 4.68	9
WISP81-113	1.713	6.04 ± 0.69	3.67 ± 1.37	16.44 ± 1.40	···	···	0
WISP81-120	1.331	< 4.14	< 3.36	27.89 ± 7.91	3.71 ± 1.13	< 3.36	9
WISP81-135	1.331	3.18 ± 0.89	< 3.57	10.15 ± 1.54	4.38 ± 0.59	< 2.48	1
WISP81-137	0.330	···	···	···	13.02 ± 1.98	< 2.58	4
WISP81-138	1.041	···	< 2.54	< 2.83	4.89 ± 0.92	6.21 ± 1.07	1
WISP81-145	1.687	3.68 ± 1.31	6.58 ± 1.63	< 5.96	···	···	0
WISP81-149	0.854	···	< 2.75	< 5.03	5.46 ± 1.24	< 2.74	4
WISP81-177	1.152	···	< 1.77	15.17 ± 2.33	4.96 ± 1.33	< 3.00	0
WISP81-178	1.225	< 5.37	< 2.53	< 7.64	6.92 ± 1.13	< 2.63	4
WISP81-185	0.931	···	< 2.16	10.93 ± 1.37	2.93 ± 0.82	< 1.47	1
WISP81-254	2.258	< 2.06	1.55 ± 0.73	6.05 ± 0.96	···	···	2
WISP81-1023	0.374	···	···	···	6.66 ± 1.14	< 1.32	5
WISP81-1044	1.069	···	< 2.95	< 2.91	5.03 ± 0.75	< 1.73	4
WISP81-1045	1.303	< 2.91	< 2.65	< 10.12	3.10 ± 0.71	< 1.48	12
WISP81-2032	0.943	···	< 2.60	< 2.16	5.07 ± 0.91	3.40 ± 1.55	10
WISP87-8	0.290	···	···	···	36.13 ± 7.54	< 11.88	5
WISP87-13	0.480	···	···	···	54.04 ± 4.56	< 12.95	4
WISP87-16	0.561	···	···	···	41.46 ± 2.12	7.18 ± 1.55	2
WISP87-23	0.564	···	···	···	26.95 ± 2.86	6.27 ± 2.24	11
WISP87-34	0.727	···	< 32.45	< 89.28	23.21 ± 3.34	< 9.11	5
WISP87-35	0.564	···	···	···	12.70 ± 1.95	< 2.77	4
WISP87-36	0.484	···	···	···	21.63 ± 1.78	4.42 ± 1.62	2

Table A.1 (cont'd)

Galaxy ID	Redshift	[O II] 3726+3729 Flux	Hβ Flux	[O III] 4959+5007 Flux	Hα Flux	[S II] 6717+6731 Flux	Quality Flag
WISP87-40	1.316	15.67 ± 2.86	12.48 ± 1.57	< 33.29	53.12 ± 3.29	15.23 ± 5.90	1
WISP87-43	1.104	···	< 7.78	< 4.97	7.37 ± 2.01	< 4.35	12
WISP87-48	0.440	···	···	···	17.32 ± 2.94	4.76 ± 1.80	2
WISP87-49	0.521	···	···	···	14.24 ± 1.77	< 3.29	4
WISP87-50	0.477	···	···	···	22.26 ± 1.49	5.79 ± 1.33	2
WISP87-52	1.051	···	< 4.15	6.32 ± 2.35	17.20 ± 1.38	3.03 ± 1.00	8
WISP87-53	0.517	···	···	···	12.66 ± 1.90	3.27 ± 1.10	2
WISP87-55	0.486	···	···	···	12.08 ± 1.48	2.31 ± 0.99	0
WISP87-58	0.672	···	< 19.24	34.87 ± 13.35	21.40 ± 1.18	2.70 ± 0.94	9
WISP87-64	1.536	25.21 ± 10.44	4.74 ± 1.62	90.45 ± 2.24	69.10 ± 7.09	···	1
WISP87-72	0.496	···	···	···	7.84 ± 1.71	< 4.23	0
WISP87-74	1.526	11.51 ± 3.13	< 21.57	< 6.37	23.76 ± 4.00	···	1
WISP87-77	1.021	···	···	< 3.76	5.64 ± 1.14	3.33 ± 1.02	2
WISP87-78	1.165	< 24.07	< 3.14	< 3.03	14.30 ± 3.35	< 7.85	12
WISP87-81	1.032	···	< 2.72	< 2.68	8.79 ± 1.96	< 4.37	4
WISP87-96	1.053	···	< 3.32	< 2.96	11.78 ± 1.87	< 4.08	5
WISP87-99	0.571	···	···	···	4.26 ± 0.74	< 2.48	12
WISP87-108	2.029	2.02 ± 0.89	< 4.01	22.63 ± 1.30	···	···	1
WISP87-121	1.007	···	< 8.13	···	7.20 ± 1.79	< 3.05	5
WISP87-139	1.019	···	< 2.77	11.19 ± 1.35	7.10 ± 1.27	< 1.97	1
WISP87-149	1.088	···	< 2.35	< 2.11	5.77 ± 0.90	< 1.63	4
WISP87-151	0.452	···	···	···	6.82 ± 1.49	< 2.61	12
WISP87-164	1.964	3.68 ± 0.80	< 2.32	7.86 ± 1.13	···	···	0
WISP87-217	1.091	···	< 1.76	< 2.49	4.02 ± 0.50	< 1.23	12
WISP87-318	1.197	< 4.59	< 0.78	< 1.59	4.42 ± 0.80	< 1.83	4
WISP87-339	0.967	···	1.64 ± 0.66	9.19 ± 0.95	8.43 ± 1.10	< 2.18	8
WISP87-344	0.584	···	···	···	14.07 ± 1.01	< 1.70	12
WISP87-2057	1.147	···	< 2.22	< 2.97	3.27 ± 0.88	< 2.41	12
WISP87-2080	0.674	···	< 7.01	< 4.77	6.86 ± 0.62	< 2.74	13
WISP94-13	0.294	···	···	···	43.76 ± 9.96	11.46 ± 3.70	3
WISP94-14	0.561	···	···	···	73.13 ± 2.97	22.81 ± 3.70	0
WISP94-16	0.542	···	···	···	28.89 ± 2.15	< 5.73	4
WISP94-17	0.374	···	···	···	42.43 ± 6.97	< 8.38	4
WISP94-19	0.561	···	···	···	43.43 ± 2.53	10.63 ± 2.57	0
WISP94-21	0.562	···	···	···	51.47 ± 2.43	17.25 ± 2.61	0
WISP94-25	0.366	···	···	···	19.13 ± 3.83	8.08 ± 3.31	2
WISP94-26	0.672	···	< 19.60	< 15.25	26.77 ± 2.48	< 14.37	5
WISP94-31	0.968	···	< 11.27	21.55 ± 4.31	57.84 ± 6.56	< 19.35	1
WISP94-33	0.723	···	< 9.23	< 10.43	8.70 ± 2.43	< 54.80	4
WISP94-36	0.697	···	< 11.83	< 17.39	17.12 ± 5.27	< 7.13	4
WISP94-37	1.134	···	< 3.31	8.06 ± 1.77	52.90 ± 3.11	16.31 ± 6.44	0
WISP94-38	0.556	···	···	···	24.35 ± 2.06	7.32 ± 2.64	2
WISP94-43	0.471	···	···	···	5.57 ± 1.26	< 0.27	4
WISP94-44	0.968	···	< 2.43	3.54 ± 1.30	16.24 ± 2.94	< 5.52	0
WISP94-46	0.644	···	···	< 24.09	17.66 ± 3.19	< 5.71	4
WISP94-47	0.542	···	···	···	9.82 ± 2.67	···	4
WISP94-51	0.324	···	···	···	17.52 ± 5.37	< 12.28	5
WISP94-53	0.551	···	···	···	3.76 ± 1.12	< 2.09	4

Table A.1 (cont'd)

Galaxy ID	Redshift	[O II] 3726+3729 Flux	Hβ Flux	[O III] 4959+5007 Flux	Hα Flux	[S II] 6717+6731 Flux	Quality Flag
WISP94-56	1.147	···	< 2.41	27.11 ± 3.66	26.79 ± 1.86	4.63 ± 1.93	0
WISP94-60	0.592	···	···	···	9.76 ± 1.25	3.46 ± 1.37	2
WISP94-67	0.375	···	···	···	12.08 ± 2.04	< 3.45	4
WISP94-71	0.341	···	···	···	8.54 ± 1.96	< 2.70	4
WISP94-72	1.834	12.91 ± 2.34	11.99 ± 4.46	175.97 ± 5.15	···	···	0
WISP94-75	1.171	< 7.72	< 1.68	< 3.09	15.77 ± 1.07	< 2.21	4
WISP94-79	0.602	···	···	< 541.59	25.43 ± 2.38	< 6.77	4
WISP94-81	0.470	···	···	···	11.08 ± 2.10	< 3.70	4
WISP94-87	0.522	···	···	···	11.36 ± 3.17	< 9.44	4
WISP94-88	0.334	···	···	···	29.27 ± 3.01	< 7.75	4
WISP94-90	1.043	···	< 5.15	< 6.13	10.90 ± 1.33	< 3.58	4
WISP94-92	0.659	···	< 45.44	< 38.17	8.91 ± 1.75	< 4.01	4
WISP94-95	1.227	< 8.38	< 2.90	6.80 ± 3.01	9.95 ± 1.25	< 3.27	0
WISP94-112	0.847	···	< 8.10	9.41 ± 4.43	8.17 ± 2.23	< 4.67	0
WISP94-119	0.493	···	···	···	5.11 ± 1.14	< 2.72	4
WISP94-146	1.827	5.35 ± 1.41	< 3.87	8.02 ± 1.81	···	···	0
WISP94-148	1.332	< 3.31	< 2.48	···	4.60 ± 0.85	< 2.04	4
WISP94-158	0.624	···	···	< 237.76	12.88 ± 2.66	< 6.18	4
WISP94-175	0.432	···	···	···	4.92 ± 0.67	< 1.81	4
WISP94-181	0.491	···	···	···	5.45 ± 1.23	< 1.82	5
WISP94-190	0.931	···	< 4.58	< 3.60	6.87 ± 1.79	< 3.15	4
WISP94-196	1.155	< 28.20	< 2.50	< 3.75	7.00 ± 1.24	< 2.29	4
WISP94-221	0.470	···	···	···	6.24 ± 0.66	2.34 ± 1.03	2
WISP94-228	1.185	< 8.28	3.27 ± 0.96	16.92 ± 1.15	6.98 ± 0.85	< 1.70	0
WISP94-239	1.104	···	···	< 1.84	7.75 ± 1.27	< 2.73	0
WISP94-263	1.168	< 12.16	< 1.75	7.60 ± 1.67	3.56 ± 1.18	< 2.73	0
WISP94-268	1.305	10.70 ± 3.29	< 26.72	< 204.00	6.01 ± 2.45	< 4.62	0
WISP94-271	1.046	···	< 4.08	< 3.25	5.38 ± 1.39	< 2.98	4
WISP94-1008	1.140	···	2.99 ± 0.68	19.37 ± 0.96	15.30 ± 1.66	< 3.65	0
WISP94-1034	0.575	···	···	···	5.66 ± 0.91	< 1.73	4
WISP94-1041	1.302	< 1.67	< 2.34	< 13.54	7.97 ± 0.94	< 1.13	4
WISP94-1042	0.278	···	···	···	19.16 ± 2.00	< 3.75	5
WISP94-2031	1.158	< 8.31	< 1.01	< 2.04	5.55 ± 1.11	< 1.87	4
WISP94-2036	0.674	···	< 4.36	< 5.53	4.42 ± 1.30	< 4.36	4
WISP94-2084	0.896	···	< 14.20	< 29.35	21.21 ± 3.18	< 12.34	4
WISP96-7	0.339	···	···	···	64.56 ± 2.80	12.55 ± 2.75	2
WISP96-8	0.597	···	···	···	62.13 ± 9.11	< 12.63	4
WISP96-13	1.139	···	< 2.03	< 3.37	78.01 ± 2.53	14.08 ± 1.81	0
WISP96-14	0.500	···	···	···	30.55 ± 1.93	15.15 ± 1.58	0
WISP96-16	0.533	···	···	···	11.52 ± 3.37	< 23.42	12
WISP96-17	0.961	···	< 4.08	18.33 ± 2.22	40.92 ± 1.72	8.45 ± 1.83	1
WISP96-20	1.126	···	2.96 ± 0.97	8.01 ± 1.18	21.80 ± 1.49	8.10 ± 1.79	0
WISP96-24	0.647	···	···	< 9.53	3.56 ± 0.52	< 1.71	12
WISP96-28	0.842	···	< 7.46	11.46 ± 4.04	22.30 ± 1.14	7.35 ± 1.18	0
WISP96-29	0.704	···	< 36.60	< 83.29	18.41 ± 2.33	< 59.93	5
WISP96-31	0.559	···	···	···	17.77 ± 0.70	5.22 ± 1.05	0
WISP96-33	1.337	< 16.03	< 6.14	< 120.73	17.39 ± 1.60	4.55 ± 1.02	2
WISP96-34	1.124	···	2.00 ± 0.64	4.76 ± 0.85	21.70 ± 1.26	8.32 ± 1.38	8

Table A.1 (cont'd)

Galaxy ID	Redshift	[O II] 3726+3729 Flux	Hβ Flux	[O III] 4959+5007 Flux	Hα Flux	[S II] 6717+6731 Flux	Quality Flag
WISP96-35	0.528	···	···	···	12.20 ± 1.32	10.93 ± 2.95	1
WISP96-37	1.251	< 2.86	1.09 ± 0.35	< 1.90	9.55 ± 1.33	< 5.03	0
WISP96-38	0.950	···	< 2.75	< 6.19	5.62 ± 1.08	< 2.12	4
WISP96-42	1.917	7.05 ± 0.67	3.59 ± 0.87	10.63 ± 1.18	···	···	0
WISP96-43	1.019	···	< 2.11	< 2.91	13.09 ± 1.52	< 1.97	5
WISP96-44	0.962	···	< 2.90	5.83 ± 1.29	11.40 ± 2.28	< 2.67	1
WISP96-45	1.140	···	2.56 ± 0.88	6.18 ± 1.05	21.34 ± 1.53	4.73 ± 1.65	8
WISP96-47	0.857	···	< 3.35	< 3.58	50.90 ± 9.46	< 6.72	5
WISP96-49	1.147	···	< 3.01	< 5.09	8.14 ± 1.66	6.10 ± 1.30	3
WISP96-59	0.484	···	···	···	8.30 ± 1.12	< 4.21	12
WISP96-65	1.114	···	< 1.64	7.15 ± 2.06	10.19 ± 0.97	3.06 ± 1.18	9
WISP96-67	0.956	···	< 1.86	4.08 ± 0.87	18.08 ± 1.17	4.28 ± 1.32	9
WISP96-68	1.349	6.70 ± 1.36	< 7.81	11.81 ± 3.48	9.06 ± 0.94	< 2.73	1
WISP96-69	1.135	···	3.98 ± 1.78	21.30 ± 2.59	22.72 ± 0.80	3.82 ± 0.70	1
WISP96-75	0.650	···	< 6.38	< 6.89	5.82 ± 0.63	1.35 ± 0.54	0
WISP96-83	0.921	···	< 1.40	< 2.23	3.17 ± 0.84	< 1.73	12
WISP96-87	1.143	···	< 2.63	< 30.03	9.15 ± 1.24	< 2.86	5
WISP96-90	1.113	···	1.16 ± 0.53	7.72 ± 0.77	11.47 ± 1.00	< 2.26	1
WISP96-95	1.280	< 3.90	< 2.33	< 3.68	5.74 ± 0.91	< 1.61	4
WISP96-96	0.673	···	< 12.55	14.75 ± 2.43	11.22 ± 1.90	< 5.99	9
WISP96-101	0.852	···	< 1.58	< 2.75	6.07 ± 0.51	1.29 ± 0.38	10
WISP96-107	1.012	···	···	3.98 ± 0.84	4.97 ± 0.87	1.61 ± 0.68	8
WISP96-111	1.329	< 2.28	< 3.34	9.32 ± 3.96	6.13 ± 0.70	< 2.89	9
WISP96-119	0.366	···	···	···	9.92 ± 2.25	< 8.84	12
WISP96-120	1.350	< 2.54	< 18.33	< 2.75	4.05 ± 0.72	< 1.68	13
WISP96-121	0.906	···	< 135.69	< 214.31	7.76 ± 1.02	< 1.80	5
WISP96-129	0.962	···	< 1.51	5.11 ± 0.84	7.41 ± 0.87	< 1.47	1
WISP96-137	0.651	···	< 6.87	< 4.04	2.88 ± 0.69	< 0.77	1
WISP96-141	0.555	···	···	···	4.42 ± 0.79	< 4.55	5
WISP96-144	0.687	···	< 5.10	10.08 ± 1.52	4.01 ± 0.51	< 5.56	1
WISP96-154	1.144	···	< 1.90	2.28 ± 0.92	3.58 ± 0.67	1.23 ± 0.40	9
WISP96-162	0.625	···	···	< 28.96	3.48 ± 0.77	1.34 ± 0.66	10
WISP96-164	0.582	···	···	···	3.16 ± 0.40	< 3.76	12
WISP96-169	1.383	3.41 ± 0.68	2.57 ± 0.78	13.02 ± 0.91	7.05 ± 0.52	1.47 ± 0.52	1
WISP96-175	1.139	···	< 5.33	< 54.87	3.27 ± 0.49	< 1.01	5
WISP96-178	1.771	5.29 ± 0.46	1.24 ± 0.33	7.06 ± 0.47	···	···	0
WISP96-188	1.336	< 2.25	< 3.02	< 3.39	3.11 ± 0.88	< 1.79	12
WISP96-194	1.043	···	< 1.37	< 1.40	3.71 ± 0.61	< 1.11	4
WISP96-199	1.348	2.18 ± 0.64	< 11.64	5.78 ± 2.43	2.81 ± 0.66	< 1.64	9
WISP96-200	1.101	···	< 1.18	4.23 ± 0.49	4.00 ± 0.62	1.69 ± 0.49	0
WISP96-201	1.291	< 1.91	< 1.12	< 1.34	2.16 ± 0.37	< 0.87	12
WISP96-210	1.118	···	< 1.11	3.36 ± 1.12	1.83 ± 0.43	< 0.80	1
WISP96-212	0.506	···	···	···	2.78 ± 0.65	1.12 ± 0.37	3
WISP96-214	1.340	2.67 ± 0.80	< 1.69	4.57 ± 1.02	3.46 ± 0.63	< 1.67	1
WISP96-215	1.458	< 1.47	< 1.99	< 2.67	2.60 ± 0.36	< 1.83	4
WISP96-216	1.258	< 2.53	< 1.37	< 2.54	7.14 ± 0.85	1.35 ± 0.65	11
WISP96-217	0.619	···	···	< 6.90	2.44 ± 0.48	< 0.95	12
WISP96-220	0.634	···	···	< 7.26	4.21 ± 1.17	< 0.28	12

Table A.1 (cont'd)

Galaxy ID	Redshift	[O II] 3726+3729 Flux	Hβ Flux	[O III] 4959+5007 Flux	Hα Flux	[S II] 6717+6731 Flux	Quality Flag
WISP96-225	1.128	···	< 1.10	< 3.34	2.67 ± 0.46	< 0.86	4
WISP96-236	0.535	···	···	···	2.18 ± 0.48	1.02 ± 0.41	2
WISP96-238	0.698	···	< 5.55	< 5.23	2.66 ± 0.62	< 4.58	4
WISP96-245	0.588	···	···	···	2.21 ± 0.59	< 1.01	5
WISP96-247	1.335	2.04 ± 0.94	< 3.54	6.85 ± 0.94	2.99 ± 0.72	1.31 ± 0.56	9
WISP96-272	0.567	···	···	···	2.70 ± 0.51	< 0.81	12
WISP96-273	1.136	···	< 2.17	3.49 ± 0.94	1.67 ± 0.29	< 0.63	0
WISP96-292	0.988	···	< 1.12	3.74 ± 0.48	3.01 ± 0.41	< 1.11	1
WISP96-297	1.134	···	< 0.78	< 1.07	2.43 ± 0.45	0.80 ± 0.35	10
WISP96-309	1.134	···	1.05 ± 0.31	4.00 ± 0.78	2.29 ± 0.43	< 0.87	1
WISP96-317	0.578	···	···	···	2.43 ± 0.43	···	5
WISP96-322	1.137	···	< 1.87	< 1.78	3.69 ± 0.50	2.38 ± 0.43	1
WISP96-332	0.353	···	···	···	4.50 ± 0.93	< 1.45	12
WISP96-334	0.541	···	···	···	1.77 ± 0.52	1.43 ± 0.44	10
WISP96-341	0.457	···	···	···	3.07 ± 0.60	0.96 ± 0.45	10
WISP96-345	1.252	< 1.94	< 0.80	< 3.39	1.89 ± 0.52	< 0.96	4
WISP96-361	1.337	< 1.93	< 1.43	< 1.68	2.16 ± 0.45	< 0.58	5
WISP96-393	1.485	2.85 ± 0.60	< 0.95	< 1.33	2.68 ± 0.54	···	1
WISP96-396	1.209	< 9.78	< 1.16	< 1.13	4.52 ± 0.52	1.99 ± 0.42	3
WISP96-399	0.918	···	< 1.83	< 2.26	2.39 ± 0.52	< 1.04	12
WISP96-408	1.241	< 5.88	< 1.42	< 1.06	2.68 ± 0.54	< 1.14	12
WISP96-427	1.691	1.23 ± 0.23	< 1.79	4.21 ± 0.91	···	···	0
WISP96-430	0.997	···	···	···	1.86 ± 0.36	< 0.72	4
WISP96-437	0.993	···	< 1.05	< 2.56	3.00 ± 0.47	< 0.99	12
WISP96-438	0.330	···	···	···	10.74 ± 0.87	< 1.40	4
WISP96-441	1.342	< 1.60	< 0.75	2.05 ± 0.72	1.75 ± 0.27	< 0.69	8
WISP96-477	0.925	···	< 1.48	< 1.86	2.69 ± 0.69	< 1.79	4
WISP96-479	0.586	···	···	···	3.10 ± 0.53	< 1.24	13
WISP96-488	1.469	< 0.62	< 1.81	< 1.53	2.35 ± 0.21	···	13
WISP96-492	1.267	< 2.85	< 1.10	< 6.74	4.11 ± 0.51	< 1.12	4
WISP96-493	0.465	···	···	···	11.35 ± 0.63	< 2.26	12
WISP96-504	0.705	···	< 2.70	3.66 ± 1.10	2.08 ± 0.30	< 2.82	1
WISP96-519	1.082	···	< 0.83	< 1.32	1.59 ± 0.33	< 0.62	12
WISP96-530	1.405	< 0.90	< 2.00	< 3.55	3.08 ± 0.51	< 0.94	5
WISP96-1006	0.508	···	···	···	2.57 ± 0.41	< 0.60	12
WISP96-1014	0.924	···	< 0.72	8.35 ± 0.86	2.28 ± 0.51	0.87 ± 0.36	1
WISP96-1020	0.522	···	···	···	3.11 ± 0.40	< 4.83	13
WISP96-1021	0.934	···	< 0.79	< 1.27	3.63 ± 0.28	< 0.63	4
WISP96-2063	0.528	···	···	···	1.27 ± 0.34	< 0.57	4
WISP96-2093	0.957	···	< 0.91	< 0.91	3.22 ± 0.48	< 1.01	12
WISP96-2119	0.882	···	< 2.00	< 1.58	2.54 ± 0.57	< 0.95	12
WISP97-7	0.577	···	···	···	57.70 ± 9.69	< 15.32	4
WISP97-11	0.582	···	···	···	35.59 ± 4.07	< 10.40	4
WISP97-17	0.399	···	···	···	36.92 ± 5.34	< 10.67	5
WISP97-19	1.034	···	< 7.45	23.02 ± 2.99	70.99 ± 3.52	40.82 ± 11.16	0
WISP97-23	0.403	···	···	···	35.53 ± 3.89	< 8.50	4
WISP97-29	0.791	···	< 15.14	< 22.71	23.57 ± 3.12	< 4.13	5
WISP97-33	0.909	···	< 9.57	< 21.96	36.01 ± 7.47	< 8.07	5

Table A.1 (cont'd)

Galaxy ID	Redshift	[O II] 3726+3729 Flux	Hβ Flux	[O III] 4959+5007 Flux	Hα Flux	[S II] 6717+6731 Flux	Quality Flag
WISP97-36	0.530	···	···	···	28.07 ± 2.74	5.26 ± 2.15	2
WISP97-37	0.853	···	< 3.96	< 4.60	26.52 ± 2.66	< 4.15	4
WISP97-38	0.575	···	···	···	12.70 ± 1.55	3.78 ± 1.37	2
WISP97-40	0.642	···	···	< 35.44	12.45 ± 1.34	< 3.20	4
WISP97-41	0.827	···	< 2.58	< 6.00	23.93 ± 2.28	5.17 ± 1.83	2
WISP97-43	1.397	14.57 ± 2.38	< 12.37	21.60 ± 6.73	···	···	1
WISP97-67	0.825	···	< 4.23	< 5.30	14.40 ± 3.57	5.66 ± 2.15	2
WISP97-72	0.422	···	···	···	9.82 ± 2.89	< 5.28	5
WISP97-75	0.638	···	···	< 38.66	14.78 ± 1.40	< 3.18	4
WISP97-76	0.304	···	···	···	24.86 ± 2.49	< 4.63	0
WISP97-77	0.660	···	< 28.40	< 17.49	5.37 ± 1.04	< 2.09	4
WISP97-78	1.043	···	< 2.26	< 3.45	14.74 ± 2.16	4.37 ± 2.00	2
WISP97-94	1.036	···	< 8.83	< 7.86	16.72 ± 2.80	< 6.23	4
WISP97-96	1.352	< 12.09	< 6.29	< 8.07	11.31 ± 1.98	< 3.82	4
WISP97-99	1.033	···	< 8.29	11.42 ± 3.72	12.20 ± 1.72	···	0
WISP97-102	1.424	6.56 ± 1.62	< 5.95	23.68 ± 4.84	7.92 ± 1.10	< 5.21	9
WISP97-105	0.449	···	···	···	10.82 ± 2.23	< 5.56	12
WISP97-107	1.683	10.27 ± 1.51	8.05 ± 2.33	20.80 ± 1.95	···	···	0
WISP97-111	1.392	6.79 ± 2.37	6.75 ± 2.80	27.53 ± 4.25	5.99 ± 1.28	< 4.59	1
WISP97-125	1.073	···	< 3.87	13.24 ± 1.86	7.71 ± 1.76	< 3.09	0
WISP97-136	0.658	···	< 27.88	< 26.69	25.37 ± 1.52	< 2.31	4
WISP97-159	1.050	···	< 1.63	< 3.24	7.59 ± 1.62	1.65 ± 0.62	2
WISP97-161	0.490	···	···	···	4.91 ± 1.49	< 4.10	4
WISP97-167	0.550	···	···	···	4.59 ± 1.05	···	4
WISP97-173	0.393	···	···	···	14.75 ± 1.30	< 3.01	4
WISP97-186	1.335	< 5.06	< 5.40	24.03 ± 5.61	6.85 ± 1.40	< 8.81	9
WISP97-192	1.002	···	3.21 ± 1.54	< 3.11	7.24 ± 1.28	< 3.35	9
WISP97-202	1.915	4.30 ± 2.14	1.87 ± 0.88	17.29 ± 1.56	···	···	0
WISP97-215	1.480	3.94 ± 1.62	3.20 ± 1.20	15.93 ± 2.50	6.68 ± 1.73	···	1
WISP97-233	1.488	3.10 ± 1.35	< 7.97	14.45 ± 2.67	6.27 ± 2.78	···	0
WISP97-238	0.673	···	< 9.11	< 16.36	9.98 ± 1.41	< 2.52	5
WISP97-245	0.809	···	< 2.90	< 3.29	6.48 ± 1.36	4.80 ± 1.23	3
WISP97-299	1.909	< 1.36	< 2.40	11.41 ± 1.35	···	···	4
WISP97-1023	0.900	···	< 1.32	< 3.20	8.18 ± 1.28	< 2.03	4
WISP114-4	0.311	···	···	···	239.08 ± 52.27	< 52.26	5
WISP114-7	0.353	···	···	···	127.51 ± 27.15	< 46.06	5
WISP114-11	0.468	···	···	···	147.38 ± 7.03	27.45 ± 6.84	0
WISP114-20	0.319	···	···	···	41.93 ± 3.59	< 4.62	0
WISP114-30	0.705	···	< 11.06	< 6.87	5.17 ± 1.26	< 11.17	12
WISP114-31	1.287	< 3.61	< 23.52	< 29.22	20.58 ± 3.55	< 7.69	4
WISP114-33	1.305	< 5.15	< 7.31	< 30.44	10.78 ± 1.58	< 6.56	5
WISP114-34	0.456	···	···	···	13.76 ± 3.17	< 7.07	4
WISP114-39	0.843	···	< 4.50	< 5.07	16.68 ± 3.66	< 4.54	5
WISP114-48	1.339	< 6.26	< 5.10	< 6.24	8.83 ± 1.48	4.58 ± 2.08	2
WISP114-49	1.148	···	< 3.19	< 2.83	13.88 ± 1.53	< 2.63	5
WISP114-52	0.846	···	< 6.46	< 9.41	15.82 ± 3.03	< 5.14	4
WISP114-61	1.019	···	< 3.15	< 4.06	7.84 ± 2.58	< 3.56	4
WISP114-63	1.232	< 13.66	< 3.55	11.58 ± 5.14	9.24 ± 2.34	< 4.19	1

Table A.1 (cont'd)

Galaxy ID	Redshift	[O II] 3726+3729 Flux	Hβ Flux	[O III] 4959+5007 Flux	Hα Flux	[S II] 6717+6731 Flux	Quality Flag
WISP114-66	1.791	3.70 ± 1.08	4.33 ± 1.50	11.49 ± 1.55	···	···	1
WISP114-67	0.839	···	···	< 6.28	10.92 ± 2.44	< 9.51	4
WISP114-71	1.042	···	< 2.43	< 4.58	6.68 ± 1.81	< 4.25	4
WISP114-97	0.836	···	< 3.46	6.77 ± 2.02	5.96 ± 1.54	< 3.12	1
WISP114-101	0.983	···	< 3.01	23.90 ± 2.98	10.75 ± 1.04	< 1.62	0
WISP114-102	0.723	···	< 5.65	< 8.62	3.96 ± 0.96	< 15.39	4
WISP114-103	0.808	···	< 6.97	< 6.27	10.89 ± 2.19	4.76 ± 1.04	10
WISP114-107	0.449	···	···	···	7.16 ± 1.96	< 7.47	4
WISP114-111	1.216	< 6.87	< 1.12	< 2.47	4.76 ± 1.46	< 2.25	4
WISP114-113	1.231	< 9.12	< 1.65	< 2.27	4.82 ± 0.95	< 2.30	4
WISP114-116	2.035	4.53 ± 1.65	< 3.16	17.45 ± 1.57	···	···	0
WISP114-117	0.857	···	< 2.35	< 3.05	6.90 ± 2.21	< 3.13	12
WISP114-120	1.223	< 10.28	< 4.51	< 3.79	5.16 ± 1.31	< 3.45	4
WISP114-123	0.355	···	···	···	9.18 ± 2.78	< 3.40	4
WISP114-130	1.727	4.44 ± 0.99	3.11 ± 1.00	8.75 ± 1.38	···	···	0
WISP114-142	1.189	< 7.46	< 1.44	13.78 ± 4.17	3.87 ± 0.70	< 2.10	0
WISP114-146	1.347	< 7.08	< 21.00	< 6.58	14.88 ± 3.31	< 3.44	5
WISP114-185	0.455	···	···	···	17.37 ± 1.98	< 4.87	13
WISP114-190	1.497	< 2.61	< 3.98	11.57 ± 4.43	7.67 ± 1.89	···	1
WISP114-192	0.479	···	···	···	10.30 ± 3.38	< 4.82	5
WISP114-202	1.182	< 8.89	< 1.66	< 2.08	8.11 ± 1.31	< 3.83	13
WISP114-208	0.391	···	···	···	6.07 ± 1.93	< 2.38	12
WISP114-228	0.588	···	···	···	2.42 ± 0.78	< 1.69	12
WISP114-230	0.595	···	···	···	2.36 ± 0.61	< 1.80	12
WISP114-238	0.508	···	···	···	5.99 ± 1.04	4.62 ± 1.32	10
WISP114-241	0.569	···	···	···	6.51 ± 0.94	< 1.73	12
WISP114-1020	1.170	< 9.50	< 1.57	< 1.41	4.96 ± 1.05	< 2.15	4
WISP114-2043	0.986	···	< 1.37	< 1.55	3.80 ± 0.90	< 1.37	12
WISP114-2050	0.448	···	···	···	7.69 ± 2.00	< 3.39	4
WISP114-2082	0.330	···	···	···	16.11 ± 1.81	< 3.58	0
WISP114-2099	0.678	···	< 11.78	< 11.88	8.06 ± 1.39	< 8.25	12
WISP115-8	0.937	···	< 25.18	< 55.27	291.16 ± 11.70	< 29.97	4
WISP115-15	0.937	···	< 42.76	···	25.49 ± 4.92	11.76 ± 4.37	2
WISP115-19	1.089	···	13.62 ± 4.17	31.89 ± 4.65	118.03 ± 4.78	37.16 ± 8.21	0
WISP115-21	0.571	···	···	···	14.43 ± 2.41	< 5.14	4
WISP115-26	0.858	···	< 7.50	< 27.97	29.68 ± 5.98	< 7.46	5
WISP115-29	1.277	< 9.60	< 4.62	< 15.69	15.04 ± 2.15	< 3.47	4
WISP115-38	0.519	···	···	···	17.81 ± 2.45	< 6.78	0
WISP115-43	1.099	···	< 3.82	< 7.90	27.16 ± 2.26	< 5.87	4
WISP115-48	1.076	···	< 6.91	< 9.20	24.99 ± 4.55	< 13.22	4
WISP115-55	1.336	< 10.16	< 8.08	< 11.62	18.88 ± 4.15	< 10.67	4
WISP115-61	1.242	< 10.25	< 2.47	< 5.93	8.22 ± 1.81	< 3.73	4
WISP115-62	0.460	···	···	···	27.35 ± 2.87	< 6.58	12
WISP115-68	0.992	···	< 2.26	< 3.17	4.31 ± 1.38	< 3.47	12
WISP115-83	1.224	< 7.74	< 3.33	< 5.35	7.28 ± 1.92	< 4.70	4
WISP115-93	1.345	16.29 ± 3.35	< 6.91	12.79 ± 2.19	13.16 ± 2.22	< 5.99	0
WISP115-97	1.336	14.50 ± 3.40	< 42.52	16.83 ± 3.30	16.72 ± 2.36	< 4.87	9
WISP115-101	1.337	< 5.03	< 3.80	< 6.98	7.69 ± 1.80	< 7.55	12

Table A.1 (cont'd)

Galaxy ID	Redshift	[O II] 3726+3729 Flux	Hβ Flux	[O III] 4959+5007 Flux	Hα Flux	[S II] 6717+6731 Flux	Quality Flag
WISP115-104	1.149	···	< 3.06	< 6.61	13.34 ± 1.68	< 6.01	12
WISP115-114	0.589	···	···	···	10.26 ± 2.69	< 3.66	5
WISP115-121	1.717	4.03 ± 0.90	< 2.18	13.44 ± 2.14	···	···	0
WISP115-129	1.085	···	4.84 ± 2.08	11.29 ± 2.09	3.74 ± 1.54	< 2.81	0
WISP115-135	0.371	···	···	···	15.82 ± 3.65	< 7.02	12
WISP115-146	1.415	< 2.51	< 8.22	< 12.56	6.70 ± 1.26	2.57 ± 1.11	3
WISP115-150	0.529	···	···	···	8.65 ± 1.45	< 2.45	12
WISP115-155	0.360	···	···	···	12.42 ± 2.58	< 4.92	5
WISP115-162	0.932	···	< 3.31	< 3.40	7.63 ± 1.73	< 4.75	4
WISP115-174	0.535	···	···	···	5.80 ± 1.31	< 2.79	12
WISP115-198	0.511	···	···	···	9.59 ± 2.24	< 5.86	5
WISP115-201	1.284	< 4.37	< 2.88	12.22 ± 5.11	7.60 ± 2.28	< 2.61	9
WISP115-212	0.486	···	···	···	10.79 ± 1.57	< 3.85	12
WISP115-213	1.365	< 3.65	< 4.28	< 4.67	5.43 ± 1.03	< 1.95	5
WISP115-264	1.290	< 5.58	< 5.19	< 7.43	4.63 ± 1.23	< 2.67	4
WISP115-1037	0.968	···	6.72 ± 2.82	16.28 ± 2.71	9.23 ± 2.03	< 5.86	9
WISP115-1045	1.289	< 3.55	< 2.26	< 12.79	5.60 ± 1.08	< 2.15	13
WISP115-2025	1.136	···	< 4.06	12.98 ± 4.44	11.46 ± 2.04	< 4.13	1
WISP115-2103	0.376	···	···	···	7.11 ± 0.97	2.02 ± 0.76	10
WISP120-16	0.551	···	···	···	77.87 ± 2.50	24.25 ± 2.67	0
WISP120-22	1.105	···	7.83 ± 2.18	27.40 ± 11.89	63.69 ± 5.69	18.88 ± 8.30	8
WISP120-23	1.179	< 91.50	< 13.30	< 2.94	67.19 ± 14.16	< 19.56	5
WISP120-25	0.405	···	···	···	22.06 ± 2.18	8.41 ± 2.12	2
WISP120-26	0.692	···	< 8.77	< 11.02	8.58 ± 1.77	< 11.07	4
WISP120-27	0.560	···	···	···	9.27 ± 1.80	···	5
WISP120-30	0.846	···	< 4.97	5.97 ± 2.47	8.80 ± 1.69	< 3.39	0
WISP120-36	1.155	< 1256.07	< 14.00	18.09 ± 3.81	21.78 ± 1.95	4.51 ± 1.81	8
WISP120-37	0.609	···	···	< 41.46	16.17 ± 2.24	< 4.57	4
WISP120-39	0.994	···	< 4.87	< 6.34	15.69 ± 2.15	< 5.45	4
WISP120-40	1.022	···	< 4.60	10.31 ± 1.48	26.73 ± 3.36	< 2.72	8
WISP120-42	1.103	···	< 3.17	7.61 ± 1.49	36.28 ± 2.50	15.53 ± 5.05	0
WISP120-43	0.562	···	···	···	31.53 ± 3.19	30.36 ± 5.30	1
WISP120-45	0.943	···	5.78 ± 2.52	19.61 ± 2.39	16.22 ± 2.58	< 4.99	0
WISP120-46	0.676	···	< 9.20	< 8.20	9.65 ± 0.99	< 6.10	4
WISP120-58	1.362	< 5.16	< 6.81	< 10.23	19.39 ± 2.30	< 4.54	4
WISP120-59	0.987	···	2.23 ± 0.91	17.82 ± 2.02	14.11 ± 1.29	5.24 ± 2.09	1
WISP120-61	1.509	9.32 ± 2.10	6.83 ± 1.93	24.97 ± 2.52	21.20 ± 3.85	···	1
WISP120-63	1.156	< 22.64	< 10.59	< 6.41	7.88 ± 1.62	< 3.60	4
WISP120-68	0.676	···	< 11.67	< 15.91	6.38 ± 1.29	< 3.60	4
WISP120-69	1.210	< 9.50	< 3.35	< 3.05	10.44 ± 1.64	< 3.15	4
WISP120-94	1.476	8.55 ± 1.85	< 4.43	19.25 ± 3.19	12.07 ± 2.81	···	0
WISP120-97	1.893	7.51 ± 0.74	< 3.64	9.00 ± 1.90	···	···	1
WISP120-98	1.309	< 5.45	< 1.86	< 66.37	10.64 ± 1.61	4.28 ± 1.84	2
WISP120-105	0.377	···	···	···	45.34 ± 5.67	46.62 ± 15.08	3
WISP120-111	1.093	···	< 1.83	5.24 ± 0.96	8.60 ± 1.40	< 295.04	0
WISP120-117	1.236	···	< 5.88	< 8.16	10.33 ± 1.40	< 2.11	4
WISP120-118	1.110	···	2.93 ± 1.18	9.55 ± 1.37	7.73 ± 1.64	< 2.22	1
WISP120-124	1.353	< 12.33	5.56 ± 2.35	20.23 ± 3.27	11.88 ± 2.77	< 7.97	1

Table A.1 (cont'd)

Galaxy ID	Redshift	[O II] 3726+3729 Flux	Hβ Flux	[O III] 4959+5007 Flux	Hα Flux	[S II] 6717+6731 Flux	Quality Flag
WISP120-133	1.023	···	< 1.99	< 2.39	8.48 ± 1.65	< 4.01	4
WISP120-135	1.055	···	< 3.25	11.14 ± 2.21	7.46 ± 1.60	< 2.65	1
WISP120-136	0.645	···	···	< 85.36	11.79 ± 2.09	< 3.28	4
WISP120-176	0.535	···	···	···	4.35 ± 1.09	< 2.13	12
WISP120-189	0.452	···	···	···	8.88 ± 1.18	< 0.91	5
WISP120-205	1.468	11.59 ± 1.94	< 2.96	11.21 ± 2.26	4.25 ± 1.39	···	0
WISP120-215	0.380	···	···	···	7.95 ± 1.65	< 1.94	4
WISP120-234	1.464	< 2.72	3.35 ± 1.41	12.19 ± 1.72	< 3.81	···	3
WISP120-277	0.704	···	< 20.07	< 14.47	6.43 ± 1.59	< 20.33	12
WISP120-295	1.896	···	< 2.28	8.37 ± 1.02	···	···	0
WISP120-324	0.986	···	< 1.81	< 2.13	4.78 ± 1.19	< 2.22	4
WISP120-330	0.600	···	···	···	3.93 ± 1.11	< 1.72	4
WISP120-349	2.057	< 5.74	2.81 ± 1.28	28.81 ± 1.45	···	···	3
WISP120-1009	0.942	···	< 1.59	11.29 ± 0.76	2.93 ± 1.21	< 1.67	0
WISP124-31	0.561	···	···	···	13.09 ± 1.79	3.27 ± 1.35	2
WISP124-45	0.696	···	< 11.65	< 30.22	8.24 ± 2.15	< 9.36	12
WISP124-49	0.309	···	···	···	15.63 ± 3.29	< 5.13	5
WISP124-51	0.435	···	···	···	14.22 ± 2.25	5.98 ± 1.73	2
WISP124-52	1.149	···	< 7.20	< 9.52	41.51 ± 8.67	< 21.36	5
WISP124-55	1.286	11.16 ± 2.19	< 2.57	< 28.19	8.91 ± 2.09	4.61 ± 1.84	1
WISP124-57	1.305	< 6.56	< 2.07	< 25.03	14.32 ± 1.63	3.97 ± 1.20	2
WISP124-62	0.475	···	···	···	10.42 ± 1.21	< 4.62	12
WISP124-65	1.464	4.39 ± 1.15	< 4.34	8.92 ± 2.16	21.68 ± 1.77	···	8
WISP124-70	1.459	7.93 ± 1.54	< 4.43	12.76 ± 1.93	17.52 ± 2.07	< 14.28	0
WISP124-74	0.694	···	< 6.42	< 5.83	6.88 ± 1.06	< 9.33	4
WISP124-88	0.414	···	···	···	8.65 ± 1.74	< 2.86	4
WISP124-95	1.140	···	< 3.09	< 4.36	7.28 ± 1.49	< 2.65	4
WISP124-97	1.227	< 5.33	< 3.24	< 2.78	6.37 ± 1.38	< 2.96	4
WISP124-107	1.145	···	< 3.40	< 3.53	6.30 ± 1.21	3.95 ± 0.90	2
WISP124-110	1.974	4.07 ± 0.66	< 2.72	6.13 ± 1.43	···	···	8
WISP124-113	0.618	···	···	< 13.53	7.25 ± 0.92	< 2.04	0
WISP124-114	1.214	< 5.87	< 4.48	< 5.09	5.36 ± 0.74	< 1.40	4
WISP124-117	0.354	···	···	···	14.25 ± 2.83	< 5.79	4
WISP124-123	1.239	< 8.63	···	< 15.09	8.11 ± 1.65	< 3.08	13
WISP124-128	1.147	···	< 1.35	< 1.09	4.98 ± 0.95	3.39 ± 0.82	2
WISP124-153	1.522	5.37 ± 2.17	···	···	···	···	0
WISP124-160	1.811	5.73 ± 0.71	< 4.26	7.22 ± 1.16	···	···	1
WISP124-178	0.518	···	···	···	15.30 ± 4.34	< 6.11	5
WISP124-180	1.224	< 5.15	< 2.87	< 2.36	3.88 ± 1.08	···	12
WISP124-182	0.979	···	< 1.93	< 2.59	13.08 ± 1.44	< 2.46	13
WISP124-186	0.641	···	···	< 6.58	3.51 ± 0.76	< 1.28	4
WISP124-195	0.851	···	< 4.20	< 8.77	6.96 ± 1.58	< 3.24	4
WISP124-244	1.239	< 22.25	< 4.43	< 6.57	11.37 ± 2.08	< 3.27	12
WISP124-247	0.769	···	< 3.26	< 7.76	11.60 ± 3.26	< 3.68	5
WISP124-258	0.829	···	< 3.20	< 1.84	4.49 ± 0.72	< 1.39	5
WISP124-269	1.210	< 3.73	< 2.70	< 1.94	3.55 ± 0.76	< 1.80	5
WISP124-280	1.132	···	< 0.99	< 1.43	3.90 ± 0.66	< 1.74	4
WISP124-285	1.014	···	< 1.64	< 4.86	5.77 ± 0.99	< 0.75	4

Table A.1 (cont'd)

Galaxy ID	Redshift	[O II] 3726+3729 Flux	Hβ Flux	[O III] 4959+5007 Flux	Hα Flux	[S II] 6717+6731 Flux	Quality Flag
WISP124-298	1.270	< 4.56	< 1.37	< 2.34	8.37 ± 0.78	< 1.73	5
WISP124-300	1.110	···	< 1.23	< 2.06	3.33 ± 0.64	1.90 ± 0.55	3
WISP124-327	1.038	···	< 2.44	< 3.57	5.11 ± 0.93	< 2.45	5
WISP124-1011	1.242	< 4.59	< 2.65	< 6.16	4.29 ± 1.42	< 2.90	12
WISP124-1014	0.926	···	< 8.11	10.57 ± 2.62	5.75 ± 0.99	< 2.46	8
WISP124-2062	1.344	< 3.66	< 8.93	< 3.21	5.85 ± 0.91	< 2.03	5
WISP124-2088	0.983	···	< 3.89	< 4.91	6.10 ± 1.57	< 2.92	4
WISP129-5	0.598	···	···	···	66.85 ± 5.46	7.93 ± 3.73	2
WISP129-8	0.690	···	< 119.30	< 238.16	88.84 ± 13.87	< 37.63	5
WISP129-15	0.317	···	···	···	66.82 ± 14.52	< 7.35	5
WISP129-17	0.569	···	···	···	38.15 ± 4.33	11.13 ± 3.24	2
WISP129-23	0.722	···	< 17.79	< 13.36	27.90 ± 4.29	< 77.43	5
WISP129-25	0.985	···	< 4.52	< 8.34	10.71 ± 1.67	< 3.75	5
WISP129-34	0.525	···	···	···	9.05 ± 1.93	< 2.99	12
WISP129-35	0.828	···	< 7.12	···	14.79 ± 2.75	< 5.51	12
WISP129-36	1.386	< 13.07	···	< 32.42	32.34 ± 4.25	13.72 ± 3.62	2
WISP129-38	1.367	12.16 ± 4.97	< 10.04	< 13.44	24.82 ± 2.74	6.47 ± 2.54	1
WISP129-41	0.921	···	< 7.10	< 8.30	16.30 ± 5.29	< 8.51	12
WISP129-42	0.888	···	7.00 ± 2.21	23.11 ± 2.59	24.44 ± 2.06	7.86 ± 1.57	0
WISP129-47	0.370	···	···	···	13.57 ± 2.88	< 5.26	12
WISP129-48	1.278	< 9.07	< 14.74	< 18.52	18.92 ± 2.52	8.29 ± 2.06	2
WISP129-52	0.678	···	< 35.89	< 30.15	46.47 ± 3.62	< 7.42	5
WISP129-58	1.091	···	< 25.05	< 70.62	23.01 ± 5.15	< 9.34	4
WISP129-62	1.168	< 19.61	< 5.24	10.99 ± 3.06	25.12 ± 4.92	< 8.96	9
WISP129-72	0.800	···	< 7.14	< 7.92	14.91 ± 3.52	< 6.88	4
WISP129-74	1.469	< 3.75	< 10.42	< 11.50	12.56 ± 1.99	···	5
WISP129-76	0.837	···	< 12.64	11.23 ± 4.52	15.41 ± 3.11	< 6.33	8
WISP129-83	1.290	< 4.94	< 2.54	< 23.94	9.94 ± 1.68	< 3.82	4
WISP129-87	1.341	< 5.44	< 4.22	< 8.32	8.50 ± 1.50	< 3.38	4
WISP129-90	0.684	···	< 13.07	< 14.88	6.77 ± 1.03	< 6.29	4
WISP129-94	1.033	···	< 2.97	< 3.90	6.01 ± 1.40	< 2.71	12
WISP129-96	0.396	···	···	···	12.75 ± 2.18	< 4.35	4
WISP129-101	0.964	···	< 5.32	< 3.72	13.68 ± 2.65	< 5.78	4
WISP129-108	0.624	···	···	···	16.33 ± 2.32	< 2.38	0
WISP129-109	1.133	···	< 2.99	< 4.43	8.55 ± 1.29	1.99 ± 0.94	2
WISP129-123	1.498	< 3.33	< 3.61	< 3.62	7.29 ± 1.36	···	4
WISP129-124	1.241	< 6.94	2.11 ± 0.79	9.13 ± 1.50	8.62 ± 1.28	< 3.01	0
WISP129-140	0.570	···	···	···	5.27 ± 1.50	< 3.15	12
WISP129-147	0.594	···	···	···	4.70 ± 0.91	< 2.09	12
WISP129-152	1.330	9.39 ± 3.59	< 8.09	< 6.87	6.68 ± 0.96	< 5.04	0
WISP129-153	1.397	< 5.10	< 4.11	< 5.33	7.19 ± 1.17	< 2.69	4
WISP129-154	0.706	···	< 13.25	< 25.39	7.56 ± 1.68	< 9.66	4
WISP129-166	0.902	···	< 8.58	< 10.73	13.62 ± 2.75	< 5.82	4
WISP129-170	0.319	···	···	···	12.92 ± 3.05	< 3.76	12
WISP129-192	0.426	···	···	···	10.66 ± 2.35	< 10.72	12
WISP129-200	0.718	···	< 8.61	< 9.93	7.76 ± 1.98	< 18.92	5
WISP129-202	1.189	< 5.90	< 2.51	< 4.18	5.52 ± 1.31	< 3.61	5
WISP129-208	1.458	< 5.13	< 7.08	< 10.19	19.18 ± 2.89	< 14.20	13

Table A.1 (cont'd)

Galaxy ID	Redshift	[O II] 3726+3729 Flux	Hβ Flux	[O III] 4959+5007 Flux	Hα Flux	[S II] 6717+6731 Flux	Quality Flag
WISP129-2063	0.654	···	< 37.87	< 18.01	5.47 ± 1.48	< 3.06	12
WISP129-2079	0.417	···	···	···	9.24 ± 1.68	< 3.47	12
WISP129-2086	1.106	···	< 1.93	< 3.62	7.48 ± 1.76	< 4.45	12
WISP129-2092	0.771	···	< 6.84	< 9.68	16.03 ± 4.20	< 3.87	5
WISP129-2093	0.419	···	···	···	8.44 ± 1.12	< 1.78	12
WISP129-2097	1.032	···	< 1.29	···	4.87 ± 0.60	< 1.30	12
WISP129-2117	1.151	< 12.13	< 3.99	< 4.71	9.75 ± 3.09	< 6.07	12
WISP129-2150	0.586	···	···	···	5.25 ± 0.70	< 1.58	12
WISP131-16	0.603	···	···	< 151.70	75.83 ± 7.63	35.96 ± 13.42	0
WISP131-18	0.597	···	···	···	102.22 ± 2.41	30.05 ± 5.02	0
WISP131-19	0.446	···	···	···	17.56 ± 2.56	< 4.32	4
WISP131-20	1.236	< 13.71	< 6.78	< 6.89	47.37 ± 8.18	< 19.43	4
WISP131-22	0.627	···	···	< 33.79	56.78 ± 3.49	< 5.10	5
WISP131-27	0.814	···	···	< 13.07	16.82 ± 2.53	< 4.95	12
WISP131-31	0.915	···	< 4.05	7.28 ± 2.27	14.73 ± 5.26	< 9.48	8
WISP131-32	0.498	···	···	···	19.32 ± 3.95	< 7.08	4
WISP131-34	0.416	···	···	···	17.34 ± 4.46	< 7.29	5
WISP131-37	0.465	···	···	···	33.68 ± 2.55	19.60 ± 6.85	2
WISP131-38	0.608	···	···	···	21.63 ± 2.41	< 4.89	4
WISP131-39	0.554	···	···	···	45.33 ± 1.89	9.78 ± 2.44	0
WISP131-40	0.808	···	< 5.59	< 7.81	25.39 ± 3.07	8.31 ± 2.16	2
WISP131-41	0.515	···	···	···	5.61 ± 1.40	< 3.15	4
WISP131-44	0.644	···	···	< 56.50	13.86 ± 2.42	< 3.07	12
WISP131-45	0.640	···	···	< 17.05	14.44 ± 2.50	< 3.70	5
WISP131-46	0.421	···	···	···	15.23 ± 2.52	7.30 ± 2.96	2
WISP131-48	0.830	···	< 13.61	< 12.54	21.32 ± 6.46	< 9.87	12
WISP131-50	1.412	< 5.46	< 9.49	< 12.22	9.10 ± 1.79	< 5.28	12
WISP131-54	0.811	···	< 10.48	< 8.93	27.73 ± 4.16	< 7.39	5
WISP131-56	0.399	···	···	···	14.97 ± 2.37	< 4.64	4
WISP131-64	0.466	···	···	···	7.40 ± 1.72	< 3.40	12
WISP131-68	1.934	···	5.02 ± 1.53	36.23 ± 1.97	···	···	2
WISP131-77	0.399	···	···	···	8.12 ± 1.58	< 3.44	12
WISP131-82	0.632	···	···	< 21.04	9.64 ± 1.90	< 2.25	5
WISP131-83	0.677	···	< 43.35	···	9.53 ± 2.87	< 7.41	12
WISP131-87	1.399	< 3.07	< 5.28	< 4.20	6.94 ± 1.41	< 4.37	12
WISP131-88	1.368	14.73 ± 2.95	< 9.16	38.31 ± 2.33	29.01 ± 1.19	5.30 ± 1.19	0
WISP131-95	1.388	< 5.96	< 3.20	< 7.32	9.52 ± 2.17	< 5.15	5
WISP131-111	1.445	< 3.62	< 5.33	< 8.98	9.11 ± 1.55	< 8.34	5
WISP131-127	0.572	···	···	···	8.35 ± 1.29	< 2.23	5
WISP131-137	0.897	···	< 3.67	11.90 ± 2.77	9.61 ± 2.15	< 3.65	0
WISP131-144	0.839	···	< 4.58	< 9.34	13.42 ± 1.87	< 2.77	5
WISP131-149	2.199	< 4.10	8.80 ± 2.68	18.04 ± 2.21	···	···	10
WISP131-157	1.257	< 5.47	< 1.53	< 2.21	7.78 ± 0.97	< 2.05	12
WISP131-178	1.903	< 1.75	11.95 ± 1.70	20.56 ± 1.26	···	···	1
WISP131-180	0.974	···	< 3.25	< 7.63	9.76 ± 1.34	< 3.06	4
WISP131-186	0.434	···	···	···	6.41 ± 1.60	< 2.92	4
WISP131-187	1.196	< 25.33	< 2.36	6.02 ± 2.04	4.65 ± 1.00	< 2.25	8
WISP131-190	0.554	···	···	···	6.64 ± 1.09	< 1.76	12

Table A.1 (cont'd)

Galaxy ID	Redshift	[O II] 3726+3729 Flux	Hβ Flux	[O III] 4959+5007 Flux	Hα Flux	[S II] 6717+6731 Flux	Quality Flag
WISP131-191	0.370	···	···	···	19.22 ± 1.75	< 2.08	12
WISP131-198	0.994	···	< 3.94	< 6.39	8.37 ± 1.92	< 4.43	4
WISP131-231	0.397	···	···	···	7.29 ± 1.69	< 2.63	12
WISP131-260	0.929	···	< 4.10	2.90 ± 1.12	8.27 ± 2.29	< 5.16	8
WISP131-303	1.348	6.56 ± 2.69	< 25.95	< 6.22	4.24 ± 1.13	< 2.04	8
WISP131-309	0.345	···	···	···	15.13 ± 3.34	< 7.89	12
WISP131-1011	1.076	···	< 2.90	7.52 ± 1.60	3.96 ± 1.02	< 2.07	0
WISP131-1027	0.631	···	···	< 21.61	4.54 ± 1.03	< 4.00	5
WISP131-2024	1.122	···	< 2.50	2.78 ± 1.15	3.71 ± 1.08	< 1.79	8
WISP131-2141	1.032	···	< 5.91	< 7.86	9.12 ± 2.83	< 4.35	4
WISP132-7	0.876	···	< 21.00	< 57.55	45.98 ± 7.22	< 16.34	5
WISP132-11	0.621	···	···	< 23.26	13.46 ± 2.05	< 3.85	0
WISP132-17	1.216	< 28.99	< 5.27	10.17 ± 3.33	31.66 ± 3.60	10.38 ± 2.78	8
WISP132-19	0.525	···	···	···	17.56 ± 2.76	7.72 ± 2.19	0
WISP132-21	0.531	···	···	···	5.78 ± 1.86	< 3.54	12
WISP132-25	0.883	···	···	< 8.05	11.97 ± 2.34	7.53 ± 2.04	2
WISP132-26	1.229	< 15.06	< 14.06	< 12.48	39.49 ± 2.95	4.92 ± 2.06	3
WISP132-29	0.870	···	< 8.45	< 6.83	32.88 ± 5.01	< 10.70	4
WISP132-30	1.229	< 17.05	3.09 ± 1.44	4.52 ± 2.26	25.56 ± 4.54	9.67 ± 3.37	8
WISP132-35	1.474	8.21 ± 2.92	< 6.64	6.25 ± 2.43	29.84 ± 6.76	···	9
WISP132-37	0.719	···	< 17.05	< 38.16	7.58 ± 1.84	< 41.37	12
WISP132-40	0.629	···	···	< 456.85	13.17 ± 2.89	< 11.07	4
WISP132-45	0.994	···	< 7.89	10.70 ± 2.67	12.06 ± 2.46	8.16 ± 2.13	8
WISP132-49	0.605	···	···	< 59.15	11.21 ± 1.81	< 3.77	4
WISP132-55	0.610	···	···	···	16.77 ± 1.40	3.67 ± 1.12	0
WISP132-60	1.220	< 15.11	< 3.45	9.27 ± 2.21	11.74 ± 1.44	< 3.32	0
WISP132-74	1.118	···	< 6.03	< 3.65	8.53 ± 1.51	< 4.24	4
WISP132-75	1.210	< 19.13	···	< 12.14	10.96 ± 1.40	4.14 ± 1.13	2
WISP132-76	1.009	···	< 5.03	< 5.58	9.70 ± 1.50	< 3.48	4
WISP132-99	0.957	···	< 3.30	< 5.77	4.64 ± 1.35	< 4.35	12
WISP132-120	0.927	···	< 3.10	< 6.06	8.85 ± 1.14	< 2.65	4
WISP132-143	1.167	< 9.33	< 4.69	< 4.67	7.10 ± 1.37	2.87 ± 1.07	2
WISP132-161	1.092	···	< 1.79	< 3.26	6.09 ± 0.73	1.79 ± 0.56	10
WISP132-180	1.098	···	< 2.34	3.49 ± 1.07	7.21 ± 1.25	< 1.66	8
WISP132-187	0.661	···	< 25.14	< 28.13	6.01 ± 1.16	< 1.92	12
WISP132-2001	0.608	···	···	···	58.52 ± 6.07	16.14 ± 4.63	0
WISP132-2044	1.383	< 3.12	< 1.77	< 5.10	5.83 ± 0.92	< 2.00	12
WISP132-2051	0.381	···	···	···	12.26 ± 1.95	< 2.98	4
WISP132-2085	0.895	···	< 2.06	3.06 ± 1.09	5.63 ± 1.09	< 2.23	8
WISP135-10	0.479	···	···	···	38.30 ± 4.04	6.48 ± 3.14	2
WISP135-19	1.062	···	4.69 ± 1.25	< 3.73	12.14 ± 2.28	< 5.01	0
WISP135-21	1.020	···	8.56 ± 3.81	34.42 ± 3.76	24.41 ± 2.96	< 3.10	1
WISP135-22	1.044	···	< 3.70	21.02 ± 1.87	38.19 ± 2.17	6.95 ± 3.17	0
WISP135-27	1.059	···	···	···	14.73 ± 3.05	< 5.82	12
WISP135-30	1.221	< 59.09	< 6.62	< 7.90	16.29 ± 3.92	< 7.66	4
WISP135-31	0.933	···	< 4.62	< 4.85	25.74 ± 3.37	5.96 ± 2.28	3
WISP135-36	1.029	···	< 4.12	< 6.79	16.22 ± 2.19	< 4.67	4
WISP135-37	1.031	···	< 11.04	< 9.39	19.13 ± 2.63	< 5.76	4

Table A.1 (cont'd)

Galaxy ID	Redshift	[O II] 3726+3729 Flux	Hβ Flux	[O III] 4959+5007 Flux	Hα Flux	[S II] 6717+6731 Flux	Quality Flag
WISP135-42	0.611	···	···	< 35.89	8.81 ± 2.20	< 4.03	12
WISP135-45	1.133	···	< 2.87	5.70 ± 1.46	28.37 ± 1.33	5.56 ± 1.43	0
WISP135-49	1.141	···	< 3.46	< 5.14	10.52 ± 1.85	< 2.65	4
WISP135-51	0.447	···	···	···	9.67 ± 2.73	< 3.19	4
WISP135-54	0.865	···	< 4.97	4.21 ± 1.65	6.56 ± 1.84	< 2.39	8
WISP135-56	1.064	···	< 3.26	< 2.62	8.35 ± 2.11	3.81 ± 1.44	2
WISP135-59	1.029	···	< 4.05	7.70 ± 2.37	7.51 ± 1.67	< 3.79	0
WISP135-64	0.402	···	···	···	15.16 ± 1.78	5.86 ± 2.77	2
WISP135-67	0.650	···	< 53.14	< 19.03	7.74 ± 2.09	< 4.50	12
WISP135-71	1.137	···	< 3.16	< 4.53	10.55 ± 2.99	< 3.91	4
WISP135-73	1.012	···	< 3.38	< 3.92	10.31 ± 1.81	< 3.60	4
WISP135-89	1.018	···	< 0.47	< 3.68	5.50 ± 1.69	< 3.61	12
WISP135-96	1.112	···	4.70 ± 1.04	18.37 ± 1.25	7.85 ± 1.75	< 2.68	0
WISP135-108	1.122	···	4.96 ± 1.57	< 6.34	11.18 ± 1.76	< 8.06	0
WISP135-119	0.564	···	···	···	8.65 ± 1.37	< 3.23	4
WISP135-151	1.004	···	< 4.11	13.40 ± 1.69	< 6.35	< 4.85	12
WISP135-178	1.081	···	< 2.22	9.62 ± 1.61	2.61 ± 0.86	< 1.37	0
WISP135-184	1.002	···	< 2.65	< 3.68	9.12 ± 1.44	< 2.58	4
WISP135-190	1.364	< 3.61	< 5.46	< 5.39	5.80 ± 0.96	< 1.54	4
WISP135-273	0.369	···	···	···	7.88 ± 1.50	< 4.16	12
WISP135-1011	1.076	···	< 4.46	< 7.37	17.96 ± 1.86	< 2.18	5
WISP135-1016	1.345	< 4.49	< 3.52	< 5.74	5.63 ± 1.27	< 2.65	12
WISP135-2022	0.900	···	6.49 ± 3.18	13.95 ± 2.17	16.88 ± 2.70	< 5.19	8
WISP135-2037	0.710	···	< 4.35	< 3.84	9.13 ± 2.02	< 5.09	1
WISP135-2042	1.178	< 14.58	< 2.02	< 3.40	6.79 ± 1.26	< 2.82	12
WISP135-2053	0.478	···	···	···	9.25 ± 1.30	< 2.36	4
WISP135-2055	0.581	···	···	···	6.82 ± 1.42	< 2.12	4
WISP135-2072	1.182	< 11.99	< 3.22	< 2.80	8.00 ± 1.77	< 5.63	4
WISP136-3	0.536	···	···	···	103.63 ± 7.68	< 33.40	4
WISP136-9	0.432	···	···	···	35.29 ± 3.17	< 7.07	4
WISP136-11	0.921	···	< 11.85	55.35 ± 6.36	40.16 ± 14.30	< 15.05	8
WISP136-14	0.885	···	12.92 ± 6.27	< 9.80	71.57 ± 5.51	< 10.65	0
WISP136-17	0.871	···	< 2.90	< 4.04	11.77 ± 2.53	< 5.02	12
WISP136-23	0.532	···	···	···	12.48 ± 1.42	< 2.53	4
WISP136-26	0.655	···	< 27.10	< 61.99	11.48 ± 3.41	< 3.15	5
WISP136-28	0.648	···	···	< 13.61	16.61 ± 1.47	2.75 ± 1.23	2
WISP136-30	0.500	···	···	···	30.95 ± 1.82	5.47 ± 1.19	2
WISP136-33	0.533	···	···	···	11.90 ± 1.43	2.81 ± 1.22	2
WISP136-37	0.752	···	< 11.75	< 48.93	24.53 ± 6.34	< 5.83	5
WISP136-38	1.200	< 8.00	3.30 ± 1.33	9.20 ± 1.52	27.25 ± 2.69	< 7.05	0
WISP136-39	0.926	···	< 4.45	< 5.77	22.29 ± 2.43	9.68 ± 2.16	2
WISP136-40	0.899	···	< 4.92	13.34 ± 2.60	29.99 ± 2.13	7.87 ± 2.83	1
WISP136-41	1.171	< 3.31	< 0.30	2.51 ± 1.23	32.25 ± 1.83	19.06 ± 6.63	8
WISP136-44	1.115	···	< 2.93	4.01 ± 1.29	3.70 ± 1.26	< 3.01	8
WISP136-48	1.815	6.85 ± 1.40	3.11 ± 1.22	27.60 ± 1.54	···	···	0
WISP136-49	0.928	···	< 2.39	< 3.01	6.74 ± 1.09	< 2.76	13
WISP136-53	1.140	···	< 2.34	7.77 ± 1.69	9.65 ± 1.26	< 2.99	0
WISP136-57	1.340	< 6.28	< 4.46	< 8.66	6.71 ± 1.86	< 3.85	12

Table A.1 (cont'd)

Galaxy ID	Redshift	[O II] 3726+3729 Flux	Hβ Flux	[O III] 4959+5007 Flux	Hα Flux	[S II] 6717+6731 Flux	Quality Flag
WISP136-58	1.333	< 4.85	< 1.40	15.64 ± 6.82	6.97 ± 1.17	< 5.73	9
WISP136-59	1.469	8.39 ± 2.48	···	···	···	···	0
WISP136-61	0.540	···	···	···	10.93 ± 1.08	< 3.19	4
WISP136-65	0.975	···	< 1.30	< 4.71	18.56 ± 2.70	< 1.90	13
WISP136-69	1.321	7.41 ± 1.66	< 18.03	21.32 ± 3.36	23.38 ± 2.46	< 4.62	1
WISP136-72	0.393	···	···	···	8.73 ± 1.83	< 3.35	4
WISP136-74	1.321	13.42 ± 5.62	< 6.14	22.32 ± 10.52	23.77 ± 2.18	< 5.72	1
WISP136-75	1.187	< 8.57	< 3.94	4.13 ± 1.87	5.61 ± 0.90	2.26 ± 1.01	8
WISP136-83	1.285	< 7.60	< 1.35	< 6.55	10.81 ± 1.55	< 4.13	5
WISP136-85	0.531	···	···	···	13.98 ± 1.70	2.55 ± 1.07	2
WISP136-95	0.616	···	···	< 95.45	4.95 ± 1.00	< 2.18	12
WISP136-96	0.412	···	···	···	6.70 ± 1.48	< 2.80	12
WISP136-100	0.533	···	···	···	5.20 ± 0.94	< 2.30	5
WISP136-102	0.969	···	< 2.01	< 3.66	6.35 ± 1.24	3.39 ± 1.53	2
WISP136-106	1.504	< 2.26	< 4.01	< 4.61	7.02 ± 1.62	···	5
WISP136-108	1.648	3.49 ± 0.74	< 1.29	3.32 ± 0.88	···	···	8
WISP136-116	1.220	< 2.35	< 1.17	< 1.65	2.96 ± 0.75	< 1.81	12
WISP136-119	0.584	···	···	···	4.63 ± 0.86	< 2.41	4
WISP136-141	1.473	3.44 ± 1.16	< 5.54	< 7.09	8.81 ± 1.19	···	0
WISP136-142	0.811	···	< 2.68	< 3.79	6.58 ± 1.52	< 3.61	5
WISP136-153	0.532	···	···	···	2.95 ± 0.83	< 1.55	12
WISP136-161	0.586	···	···	···	3.42 ± 0.77	< 1.61	12
WISP136-169	0.953	···	< 2.49	< 3.06	5.75 ± 1.70	< 2.66	12
WISP136-177	0.561	···	···	···	3.57 ± 0.94	< 2.54	13
WISP136-182	0.287	···	···	···	19.86 ± 3.47	< 4.98	5
WISP136-189	1.644	4.74 ± 1.08	< 1.76	8.77 ± 1.24	···	···	1
WISP136-190	1.459	< 1.00	< 1.51	< 3.33	7.53 ± 1.17	< 0.92	5
WISP136-200	0.315	···	···	···	8.08 ± 1.54	< 3.39	12
WISP136-210	0.562	···	···	···	5.57 ± 0.80	< 2.58	4
WISP136-221	1.898	< 1.49	< 1.71	5.55 ± 0.76	···	···	12
WISP136-223	1.237	< 4.73	< 1.36	4.18 ± 0.95	2.50 ± 0.68	< 1.75	0
WISP136-236	1.076	···	< 1.58	7.88 ± 0.97	5.23 ± 0.75	3.05 ± 0.86	0
WISP136-240	0.442	···	···	···	3.73 ± 0.74	< 1.21	4
WISP136-251	0.710	···	< 6.50	< 6.50	5.34 ± 1.13	< 7.88	5
WISP136-255	1.382	< 1.62	< 2.62	< 4.71	5.89 ± 1.59	< 2.47	12
WISP136-282	0.343	···	···	···	13.08 ± 2.88	< 6.96	12
WISP136-301	0.481	···	···	···	3.20 ± 0.52	< 1.19	12
WISP136-339	1.478	< 1.97	< 4.81	< 5.24	7.06 ± 2.17	···	5
WISP136-360	2.199	< 2.27	< 2.09	10.80 ± 1.60	···	···	4
WISP136-1011	1.204	< 1.75	< 0.85	< 1.55	5.93 ± 0.92	< 2.09	4
WISP136-1017	0.985	···	< 1.83	< 2.98	5.17 ± 1.14	< 1.98	12
WISP136-2060	0.591	···	···	···	3.69 ± 0.48	< 1.41	12
WISP136-2101	2.042	< 1.19	2.18 ± 0.74	6.68 ± 0.96	···	···	10
WISP143-6	0.376	···	···	···	181.43 ± 36.50	< 54.44	5
WISP143-11	0.994	···	< 16.87	< 40.83	45.34 ± 8.15	< 5.04	4
WISP143-12	1.052	···	< 5.10	< 5.59	22.96 ± 4.05	8.01 ± 3.62	2
WISP143-13	0.980	···	< 6.06	< 6.24	18.65 ± 3.56	< 19.89	12
WISP143-14	0.982	···	< 3.27	10.76 ± 1.98	70.39 ± 2.71	7.61 ± 2.26	0

Table A.1 (cont'd)

Galaxy ID	Redshift	[O II] 3726+3729 Flux	Hβ Flux	[O III] 4959+5007 Flux	Hα Flux	[S II] 6717+6731 Flux	Quality Flag
WISP143-17	0.990	···	29.64 ± 12.43	10.57 ± 2.40	48.33 ± 5.09	< 9.98	0
WISP143-24	0.922	···	< 2.53	< 4.35	12.87 ± 2.38	3.30 ± 1.63	3
WISP143-27	0.933	···	< 6.43	···	24.89 ± 3.16	6.67 ± 2.70	2
WISP143-28	1.097	···	···	< 5.21	30.00 ± 2.72	5.07 ± 2.12	2
WISP143-33	1.338	< 10.91	< 14.61	< 18.04	27.19 ± 4.26	< 9.98	4
WISP143-35	0.481	···	···	···	22.00 ± 1.29	5.92 ± 1.35	2
WISP143-39	0.577	···	···	···	12.76 ± 1.00	5.38 ± 1.23	2
WISP143-42	1.336	< 5.90	< 2.17	< 19.95	15.42 ± 1.63	< 4.12	4
WISP143-44	0.892	···	< 3.72	6.11 ± 2.46	21.11 ± 2.17	5.02 ± 2.48	0
WISP143-48	1.326	8.40 ± 1.88	< 10.19	< 18.25	19.04 ± 2.12	21.17 ± 9.41	0
WISP143-52	1.091	···	4.60 ± 1.76	8.90 ± 2.56	33.03 ± 1.41	7.21 ± 1.53	0
WISP143-53	0.361	···	···	···	33.11 ± 4.47	< 5.86	5
WISP143-54	0.924	···	3.46 ± 0.86	5.23 ± 1.52	18.57 ± 2.02	< 3.30	8
WISP143-56	1.614	19.14 ± 2.11	17.79 ± 2.69	173.40 ± 3.22	···	···	1
WISP143-57	1.487	< 27.28	< 4.63	10.01 ± 2.47	13.65 ± 1.77	···	1
WISP143-58	0.943	···	< 6.18	17.60 ± 4.81	4.95 ± 1.49	< 2.97	1
WISP143-60	1.225	< 7.01	< 2.02	< 2.56	8.00 ± 1.56	< 3.77	4
WISP143-61	0.915	···	< 3.19	< 5.96	9.94 ± 1.93	< 4.98	5
WISP143-63	0.492	···	···	···	13.21 ± 1.25	1.65 ± 0.70	2
WISP143-66	0.987	···	< 2.55	< 3.08	7.01 ± 1.17	< 1.83	4
WISP143-67	1.196	< 7.35	< 4.43	< 1.65	9.47 ± 2.11	< 4.42	4
WISP143-68	1.472	< 3.23	3.12 ± 1.16	9.58 ± 1.64	15.55 ± 2.70	8.59 ± 3.39	9
WISP143-71	0.991	···	< 3.23	9.28 ± 2.72	9.70 ± 1.20	< 2.42	1
WISP143-73	0.577	···	···	···	8.91 ± 1.20	4.06 ± 1.76	3
WISP143-74	0.828	···	< 3.83	< 4.85	7.84 ± 0.99	< 2.28	12
WISP143-80	1.330	< 4.23	< 2.08	< 9.01	6.42 ± 1.41	< 2.99	4
WISP143-82	0.876	···	< 3.16	4.84 ± 2.13	6.96 ± 1.71	< 2.62	8
WISP143-91	0.841	···	< 7.08	< 16.40	22.80 ± 3.05	4.54 ± 1.85	3
WISP143-95	1.198	< 10.86	< 1.61	< 2.59	5.84 ± 0.99	< 2.65	12
WISP143-97	2.116	< 3.10	3.40 ± 1.10	29.42 ± 1.51	···	···	0
WISP143-102	1.448	< 2.24	< 2.69	< 2.39	3.58 ± 1.00	< 7.90	13
WISP143-107	0.643	···	···	< 7.33	3.85 ± 1.12	< 2.00	4
WISP143-108	0.670	···	< 9.03	28.76 ± 4.22	6.68 ± 0.78	1.46 ± 0.45	9
WISP143-116	1.199	< 8.78	< 3.51	8.02 ± 2.82	10.97 ± 1.93	< 5.06	0
WISP143-120	0.419	···	···	···	6.49 ± 1.48	< 1.57	4
WISP143-123	0.872	···	< 2.55	< 4.10	10.75 ± 2.23	< 8.13	4
WISP143-126	1.324	5.72 ± 1.27	< 3.19	6.56 ± 1.77	5.72 ± 0.92	< 2.43	1
WISP143-129	1.083	···	< 3.49	8.55 ± 1.37	3.63 ± 1.06	< 2.09	0
WISP143-132	0.386	···	···	···	12.47 ± 1.24	< 1.41	4
WISP143-145	1.480	< 2.39	< 4.86	< 5.11	8.12 ± 2.36	···	13
WISP143-146	0.534	···	···	···	3.85 ± 1.01	2.78 ± 1.31	2
WISP143-157	1.560	< 2.35	3.97 ± 1.37	12.29 ± 1.50	30.13 ± 5.38	···	9
WISP143-159	0.406	···	···	···	4.29 ± 1.10	< 1.78	4
WISP143-161	0.475	···	···	···	6.37 ± 1.03	< 2.03	4
WISP143-163	0.888	···	< 2.47	10.73 ± 1.33	< 5.53	< 4.52	5
WISP143-165	0.648	···	···	< 17.86	4.96 ± 1.01	< 2.04	4
WISP143-167	1.385	< 2.79	< 5.08	14.20 ± 1.81	3.53 ± 1.09	< 2.86	1
WISP143-170	0.538	···	···	···	3.62 ± 0.77	< 1.47	5

Table A.1 (cont'd)

Galaxy ID	Redshift	[O II] 3726+3729 Flux	Hβ Flux	[O III] 4959+5007 Flux	Hα Flux	[S II] 6717+6731 Flux	Quality Flag
WISP143-173	1.985	8.72 ± 1.65	2.91 ± 1.02	13.28 ± 1.16	···	···	0
WISP143-175	1.425	< 1.75	< 3.88	13.59 ± 1.53	6.98 ± 1.15	< 3.91	0
WISP143-177	0.848	···	< 3.94	9.17 ± 2.65	9.26 ± 2.30	< 2.76	1
WISP143-194	1.323	5.47 ± 2.00	< 2.39	9.09 ± 2.07	6.81 ± 1.06	< 2.59	9
WISP143-197	1.382	< 5.69	< 17.07	< 11.54	18.51 ± 3.05	< 4.98	5
WISP143-220	1.677	2.68 ± 0.71	< 2.19	9.72 ± 1.01	···	···	1
WISP143-222	1.252	< 4.87	< 2.10	< 7.65	8.60 ± 1.32	< 2.82	4
WISP143-232	0.389	···	···	···	6.97 ± 1.54	< 2.26	4
WISP143-236	0.599	···	···	···	6.41 ± 1.66	< 4.03	4
WISP143-253	0.521	···	···	···	3.59 ± 0.92	< 1.67	12
WISP143-254	1.256	< 5.67	< 1.96	9.79 ± 3.54	5.45 ± 1.09	< 2.06	0
WISP143-264	1.484	< 2.07	< 2.70	10.68 ± 2.16	11.86 ± 1.66	···	0
WISP143-288	0.993	···	< 2.68	< 3.62	6.25 ± 1.17	< 2.04	4
WISP143-304	1.061	···	< 2.38	< 2.29	5.22 ± 0.86	< 4.72	4
WISP143-321	1.281	< 2.55	1.27 ± 0.55	< 4.45	6.09 ± 0.92	< 2.65	8
WISP143-323	0.310	···	···	···	6.34 ± 1.27	< 2.10	4
WISP143-2005	0.479	···	···	···	11.55 ± 2.15	< 3.76	5
WISP143-2037	1.405	< 2.06	< 5.77	< 7.67	3.85 ± 0.78	< 1.94	4
WISP146-7	0.532	···	···	···	43.23 ± 3.47	< 6.25	4
WISP146-8	0.860	···	< 3.47	9.08 ± 1.75	115.83 ± 32.99	< 34.97	1
WISP146-16	1.178	< 15.85	···	···	30.78 ± 1.77	< 2.94	5
WISP146-17	0.559	···	···	···	25.05 ± 2.89	< 7.52	5
WISP146-19	0.959	···	< 5.18	< 4.88	29.71 ± 2.09	11.40 ± 2.12	0
WISP146-22	1.177	< 26.97	< 10.02	7.95 ± 2.71	29.63 ± 2.42	< 4.58	8
WISP146-27	0.625	···	···	< 28.16	12.76 ± 2.18	5.76 ± 1.96	2
WISP146-28	1.778	3.28 ± 1.06	< 4.36	15.25 ± 2.27	···	···	0
WISP146-29	0.417	···	···	···	13.84 ± 2.16	< 4.36	4
WISP146-32	1.206	< 11.41	< 3.86	11.32 ± 2.60	5.27 ± 1.68	< 2.95	8
WISP146-33	1.208	< 10.46	5.48 ± 1.05	43.71 ± 1.62	44.50 ± 1.84	5.70 ± 1.57	0
WISP146-36	1.181	< 25.90	< 3.36	< 4.04	24.03 ± 1.86	< 3.72	4
WISP146-47	0.962	···	< 3.77	9.84 ± 1.94	8.24 ± 2.10	< 4.63	0
WISP146-54	1.057	···	< 2.31	8.10 ± 1.19	7.53 ± 1.41	···	8
WISP146-57	0.609	···	···	···	8.73 ± 0.97	< 2.62	0
WISP146-60	0.590	···	···	···	9.18 ± 1.00	7.47 ± 1.66	2
WISP146-64	0.957	···	< 3.52	28.55 ± 5.21	11.79 ± 1.08	< 2.24	0
WISP146-72	1.506	< 2.16	< 2.43	9.74 ± 1.31	13.89 ± 1.26	···	1
WISP146-74	1.440	< 4.77	< 4.31	9.36 ± 1.98	5.08 ± 0.66	< 1.75	9
WISP146-77	1.217	< 10.45	< 2.39	8.12 ± 1.46	7.89 ± 0.80	< 2.93	1
WISP146-79	1.305	< 4.75	< 2.56	< 32.85	6.29 ± 0.99	< 2.28	4
WISP146-91	1.775	5.78 ± 1.69	< 2.77	7.19 ± 1.21	···	···	0
WISP146-95	1.337	< 3.90	< 6.15	< 3.86	6.62 ± 1.53	< 2.85	4
WISP146-96	1.562	6.28 ± 1.22	2.89 ± 1.16	24.17 ± 1.28	···	···	0
WISP146-113	0.587	···	···	···	7.59 ± 0.82	1.90 ± 0.58	10
WISP146-120	1.310	< 16.13	< 7.97	6.88 ± 2.54	5.45 ± 0.98	< 3.67	9
WISP146-150	1.133	···	< 3.12	7.30 ± 1.79	5.43 ± 1.77	< 2.25	8
WISP146-186	1.279	< 3.77	< 3.27	< 4.42	3.79 ± 0.78	< 1.75	4
WISP146-187	1.201	< 12.97	< 1.75	< 2.18	5.99 ± 1.10	2.80 ± 0.76	11
WISP146-190	1.042	···	< 1.92	5.14 ± 0.92	3.70 ± 0.74	< 1.83	1

Table A.1 (cont'd)

Galaxy ID	Redshift	[O II] 3726+3729 Flux	Hβ Flux	[O III] 4959+5007 Flux	Hα Flux	[S II] 6717+6731 Flux	Quality Flag
WISP146-215	1.114	···	3.37 ± 0.95	9.55 ± 0.89	4.82 ± 0.62	< 1.09	0
WISP146-240	1.051	···	< 1.82	< 2.71	6.42 ± 1.41	< 3.07	4
WISP146-244	1.800	2.88 ± 0.80	2.26 ± 0.86	7.90 ± 1.00	···	···	1
WISP146-275	1.139	···	< 2.19	< 2.35	7.41 ± 1.56	< 3.03	4
WISP146-310	2.032	2.50 ± 0.69	< 2.71	10.75 ± 0.92	···	···	0
WISP146-1014	1.084	···	< 2.19	< 4.78	7.81 ± 1.20	< 2.02	5
WISP147-18	0.563	···	···	···	24.08 ± 1.75	9.68 ± 2.47	0
WISP147-21	0.452	···	···	···	59.68 ± 1.76	13.55 ± 1.59	0
WISP147-22	0.848	···	< 3.33	< 8.11	17.37 ± 2.06	6.07 ± 2.56	2
WISP147-23	0.851	···	< 8.62	< 7.42	23.40 ± 4.34	< 6.41	4
WISP147-25	0.551	···	···	···	7.07 ± 2.09	< 5.96	4
WISP147-34	0.882	···	< 4.75	< 4.25	14.35 ± 2.51	< 3.77	4
WISP147-35	1.112	···	< 7.86	< 9.03	15.41 ± 4.13	< 6.87	12
WISP147-36	1.304	< 7.19	< 3.28	< 46.33	12.75 ± 2.21	< 4.07	4
WISP147-39	0.978	···	< 3.43	5.84 ± 1.96	21.01 ± 1.86	< 4.33	0
WISP147-42	0.711	···	< 12.64	< 19.74	13.76 ± 3.20	< 9.69	4
WISP147-46	1.457	< 5.64	8.82 ± 2.97	43.64 ± 4.48	< 25.41	< 53.88	2
WISP147-48	1.109	···	< 5.26	< 3.96	26.83 ± 2.06	3.34 ± 1.27	3
WISP147-51	0.933	···	···	< 6.46	7.35 ± 1.69	< 2.92	12
WISP147-54	1.095	···	< 4.97	10.59 ± 1.87	12.08 ± 1.71	3.80 ± 1.62	8
WISP147-56	0.363	···	···	···	13.13 ± 1.83	< 4.82	13
WISP147-58	1.091	···	< 4.05	5.78 ± 1.65	6.62 ± 1.77	< 4.35	0
WISP147-72	2.196	< 6.48	10.44 ± 2.32	50.59 ± 2.53	···	···	2
WISP147-73	1.091	···	< 3.75	6.15 ± 1.61	13.21 ± 1.91	< 4.21	8
WISP147-82	1.570	4.58 ± 2.04	< 3.63	21.88 ± 4.88	55.85 ± 13.25	···	9
WISP147-88	1.305	< 3.73	< 4.40	< 143.15	10.80 ± 1.96	< 3.86	5
WISP147-90	0.707	···	< 9.92	< 5.67	8.31 ± 1.23	< 20.20	5
WISP147-114	1.418	< 2.03	< 2.92	3.56 ± 1.23	5.26 ± 1.50	< 2.71	9
WISP147-125	1.328	< 5.72	< 13.88	< 8.58	9.21 ± 1.91	< 4.66	4
WISP147-164	0.974	···	< 2.00	9.18 ± 3.22	8.21 ± 2.10	< 4.15	1
WISP147-180	0.431	···	···	···	8.36 ± 1.61	< 3.36	12
WISP147-185	1.515	3.26 ± 1.34	< 2.08	8.74 ± 1.25	···	···	0
WISP147-202	0.408	···	···	···	14.52 ± 2.10	< 2.83	12
WISP147-208	0.375	···	···	···	16.13 ± 1.89	< 3.69	13
WISP147-235	0.492	···	···	···	7.47 ± 0.71	< 1.36	4
WISP147-2014	1.088	···	< 2.73	< 1.98	12.52 ± 1.02	< 2.51	5
WISP147-2022	2.267	3.34 ± 1.18	< 2.08	13.18 ± 2.91	···	···	0
WISP147-2024	0.319	···	···	···	22.96 ± 2.28	< 3.51	4
WISP167-8	0.505	···	···	···	17.04 ± 2.45	< 4.39	12
WISP167-9	0.489	···	···	···	53.40 ± 6.08	21.50 ± 4.81	2
WISP167-11	0.494	···	···	···	33.37 ± 2.91	< 5.92	4
WISP167-12	0.557	···	···	···	40.75 ± 3.62	8.42 ± 2.61	0
WISP167-13	0.929	···	< 8.09	11.85 ± 3.25	43.29 ± 6.63	< 8.61	0
WISP167-16	0.618	···	···	< 313.66	15.42 ± 3.64	< 8.24	4
WISP167-17	0.562	···	···	···	29.68 ± 2.77	5.53 ± 2.18	3
WISP167-27	0.926	···	< 4.78	< 8.51	17.99 ± 1.83	< 4.61	5
WISP167-28	0.996	···	< 8.20	< 11.21	31.32 ± 9.01	< 8.66	5
WISP167-30	0.560	···	···	···	23.06 ± 2.88	4.11 ± 1.92	2

Table A.1 (cont'd)

Galaxy ID	Redshift	[O II] 3726+3729 Flux	Hβ Flux	[O III] 4959+5007 Flux	Hα Flux	[S II] 6717+6731 Flux	Quality Flag
WISP167-31	0.512	···	···	···	30.17 ± 3.21	< 7.92	12
WISP167-34	1.126	···	< 10.95	< 5.23	10.30 ± 1.89	< 5.18	5
WISP167-39	1.314	20.44 ± 9.72	< 15.05	< 50.51	13.19 ± 1.87	5.11 ± 1.69	1
WISP167-40	0.494	···	···	···	21.31 ± 5.48	< 13.48	5
WISP167-42	0.934	···	< 5.44	< 8.46	9.68 ± 1.88	< 4.29	4
WISP167-45	0.921	···	···	···	12.61 ± 1.82	< 4.18	4
WISP167-51	1.308	< 6.77	< 9.57	< 284.97	7.16 ± 1.76	< 2.74	4
WISP167-62	1.119	···	< 4.48	< 5.12	8.53 ± 1.70	< 3.11	4
WISP167-67	0.854	···	···	< 6.26	8.50 ± 1.50	< 3.84	5
WISP167-81	1.250	< 3.90	< 5.92	< 6.88	9.70 ± 2.11	< 5.05	4
WISP167-84	1.066	···	< 2.87	7.43 ± 1.58	16.04 ± 2.95	< 7.73	8
WISP167-85	0.566	···	···	···	9.32 ± 2.24	< 5.16	4
WISP167-86	1.317	11.03 ± 4.67	< 7.84	< 12.05	13.15 ± 2.15	< 4.42	0
WISP167-87	1.250	< 8.74	< 4.50	< 6.88	8.81 ± 1.84	< 7.40	5
WISP167-93	1.319	< 4.46	< 4.98	< 7.01	11.02 ± 1.37	< 3.27	4
WISP167-95	0.958	···	< 5.73	< 7.53	8.55 ± 1.33	< 2.78	12
WISP167-97	0.928	···	···	···	14.36 ± 1.09	< 2.71	4
WISP167-100	1.320	< 4.69	< 3.68	19.68 ± 7.55	8.91 ± 1.15	< 3.36	1
WISP167-102	1.271	< 7.32	3.63 ± 1.10	7.54 ± 1.35	7.86 ± 1.45	< 2.65	9
WISP167-110	0.664	···	< 7.01	< 12.05	6.18 ± 1.13	3.49 ± 1.09	2
WISP167-114	0.921	···	< 8.64	< 42.36	12.49 ± 1.05	< 2.84	4
WISP167-129	0.671	···	< 24.11	< 28.78	11.07 ± 1.34	3.38 ± 1.21	2
WISP167-144	0.581	···	···	···	4.15 ± 1.15	< 3.62	5
WISP167-170	1.300	11.35 ± 3.60	< 5.53	< 32.71	4.22 ± 1.05	< 2.30	0
WISP167-174	1.379	7.77 ± 3.11	< 16.39	< 5.26	4.54 ± 0.96	< 2.16	8
WISP167-229	1.163	< 20.27	< 4.33	< 5.74	11.78 ± 2.30	< 11.48	12
WISP167-1018	1.446	< 3.15	< 3.72	12.75 ± 2.29	4.77 ± 0.70	< 4.03	0
WISP167-2010	0.858	···	< 6.63	12.44 ± 2.80	11.53 ± 1.23	< 2.62	1
WISP167-2044	1.289	6.26 ± 2.38	< 10.38	< 21.30	5.62 ± 1.12	< 2.15	1
WISP167-2105	0.632	···	···	< 26.95	5.25 ± 1.05	< 2.18	13

Note. — Emission line fluxes in units of 10^{-17}erg/s/cm^2/Å. Flux limits are 3σ.

Table A.2. Emisson Line Fluxes for galaxies with detected [S III] or He I Lines

Galaxy ID	Redshift	Hα Flux	[S II] 6717+6731 Flux	[S III] 9069 Flux	[S III] 9532 Flux	He I 10830 Flux	Quality Flag
WISP17-17	0.643	33.46 ± 2.81	13.46 ± 2.51	10.35 ± 2.87	< 7.75	···	0
WISP68-26	0.265	< 28.35	< 15.35	< 18.53	10.65 ± 2.92	< 6.21	0
WISP68-52	0.776	17.33 ± 8.34	< 5.39	4.01 ± 1.29	···	···	1
WISP69-65	0.379	18.10 ± 2.70	< 2.62	< 3.35	4.73 ± 1.17	< 3.05	0
WISP73-32	0.606	10.96 ± 2.29	11.79 ± 3.77	6.70 ± 1.55	< 4.36	···	0
WISP76-16	0.323	72.02 ± 4.37	20.33 ± 3.01	< 7.00	10.12 ± 2.19	< 4.85	0
WISP76-17	0.694	19.49 ± 5.49	< 12.16	6.71 ± 1.44	< 5.08	···	0
WISP76-86	0.376	8.43 ± 2.12	< 5.05	< 5.97	< 0.50	5.62 ± 1.66	8
WISP78-49	0.569	15.48 ± 2.32	6.64 ± 3.08	< 5.34	6.11 ± 2.28	···	0
WISP78-67	0.557	29.23 ± 1.61	4.20 ± 1.13	< 3.69	4.14 ± 1.35	···	0
WISP79-79	0.660	9.35 ± 0.77	4.04 ± 0.97	< 2.43	3.10 ± 0.80	···	0
WISP79-108	0.406	18.68 ± 1.02	< 2.09	< 1.59	2.06 ± 0.62	< 1.60	0
WISP81-58	0.308	27.49 ± 1.17	4.85 ± 1.09	< 3.71	3.66 ± 0.69	12.01 ± 4.63	1
WISP87-55	0.486	12.08 ± 1.48	2.31 ± 0.99	···	···	4.32 ± 1.46	0
WISP87-72	0.496	7.84 ± 1.71	< 4.23	< 6.07	5.29 ± 1.70	< 3.80	0
WISP94-19	0.561	43.43 ± 2.53	10.63 ± 2.57	< 4.63	8.35 ± 1.61	···	0
WISP94-21	0.562	51.47 ± 2.43	17.25 ± 2.61	< 4.28	4.84 ± 1.62	···	0
WISP96-14	0.500	30.55 ± 1.93	15.15 ± 1.58	< 3.16	2.03 ± 1.00	< 2.37	0
WISP96-31	0.559	17.77 ± 0.70	5.22 ± 1.05	1.90 ± 0.41	2.29 ± 0.52	···	0
WISP96-35	0.528	12.20 ± 1.32	10.93 ± 2.95	< 1.58	4.85 ± 1.52	< 4.44	1
WISP96-75	0.650	5.82 ± 0.63	1.35 ± 0.54	< 0.69	1.24 ± 0.37	···	0
WISP96-137	0.651	2.88 ± 0.69	< 0.77	< 0.86	0.87 ± 0.29	···	1
WISP97-76	0.304	24.86 ± 2.49	< 4.63	< 6.72	7.72 ± 1.84	< 4.08	0
WISP114-11	0.468	147.38 ± 7.03	27.45 ± 6.84	< 6.92	11.02 ± 2.24	< 8.35	0
WISP114-20	0.319	41.93 ± 3.59	< 4.62	< 5.18	9.55 ± 1.19	< 5.72	0
WISP115-38	0.519	17.81 ± 2.45	< 6.78	5.83 ± 1.55	< 4.80	< 7.46	0
WISP120-16	0.551	77.87 ± 2.50	24.25 ± 2.67	< 4.09	14.54 ± 1.91	···	0
WISP124-113	0.618	7.25 ± 0.92	< 2.04	< 3.98	4.46 ± 1.08	···	0
WISP129-108	0.624	16.33 ± 2.32	< 2.38	< 3.34	6.18 ± 1.21	···	0
WISP131-16	0.603	75.83 ± 7.63	35.96 ± 13.42	< 12.61	12.68 ± 2.89	···	0
WISP131-18	0.597	102.22 ± 2.41	30.05 ± 5.02	10.67 ± 2.02	16.05 ± 1.34	···	0
WISP131-39	0.554	45.33 ± 1.89	9.78 ± 2.44	< 3.05	10.17 ± 1.42	···	0
WISP132-11	0.621	13.46 ± 2.05	< 3.85	10.22 ± 1.90	< 6.98	···	0
WISP132-19	0.525	17.56 ± 2.76	7.72 ± 2.19	< 6.20	5.37 ± 2.54	< 6.94	0
WISP132-55	0.610	16.77 ± 1.40	3.67 ± 1.12	< 3.32	2.59 ± 1.03	···	0
WISP132-2001	0.608	58.52 ± 6.07	16.14 ± 4.63	< 11.04	11.17 ± 3.74	···	0
WISP135-2037	0.710	9.13 ± 2.02	< 5.09	2.85 ± 0.83	< 2.30	···	1
WISP146-57	0.609	8.73 ± 0.97	< 2.62	< 1.72	2.65 ± 0.84	···	0
WISP147-18	0.563	24.08 ± 1.75	9.68 ± 2.47	···	11.37 ± 1.67	10.55 ± 1.71	0
WISP147-21	0.452	59.68 ± 1.76	13.55 ± 1.59	< 5.12	9.51 ± 1.02	5.07 ± 1.23	0
WISP167-12	0.557	40.75 ± 3.62	8.42 ± 2.61	10.89 ± 2.64	< 6.25	···	0

Note. — Emission line fluxes in units of 10^{-17}erg/s/cm^2/Å. Flux limits are 3σ.

Bibliography

Agarwal, B., Dalla Vecchia, C., Johnson, J. L., Khochfar, S., & Paardekooper, J.-P. 2014, Monthly Notices of the Royal Astronomical Society, 443, 648

Agarwal, B., Davis, A. J., Khochfar, S., Natarajan, P., & Dunlop, J. S. 2013, Monthly Notices of the Royal Astronomical Society, 432, 3438

Agarwal, B., Khochfar, S., Johnson, J. L., Neistein, E., Dalla Vecchia, C., & Livio, M. 2012, Monthly Notices of the Royal Astronomical Society, 425, 2854

Aird, J., Nandra, K., Laird, E. S., Georgakakis, A., Ashby, M. L. N., Barmby, P., Coil, A. L., Huang, J.-S., Koekemoer, A. M., Steidel, C. C., & Willmer, C. N. A. 2010, Monthly Notices of the Royal Astronomical Society, 401, 2531

Alexander, D. M., Bauer, F. E., Brandt, W. N., Schneider, D. P., Hornschemeier, A. E., Vignali, C., Barger, A. J., Broos, P. S., Cowie, L. L., Garmire, G. P., Townsley, L. K., Bautz, M. W., Chartas, G., & Sargent, W. L. W. 2003, The Astronomical Journal, 126, 539

Alexander, T. & Natarajan, P. 2014, Science, 345, 1330

Andrews, B. H. & Martini, P. 2013, The Astrophysical Journal, 765, 140

Assef, R. J., Stern, D., Kochanek, C. S., Blain, A. W., Brodwin, M., Brown, M. J. I., Donoso, E., Eisenhardt, P. R. M., Jannuzi, B. T., Jarrett, T. H., Stanford, S. A., Tsai, C.-W., Wu, J., & Yan, L. 2013, The Astrophysical Journal, 772, 26

Atek, H., Kneib, J.-P., Pacifici, C., Malkan, M., Charlot, S., Lee, J., Bedregal, A., Bunker, A. J., Colbert, J. W., Dressler, A., Hathi, N., Lehnert, M., Martin, C. L., McCarthy, P., Rafelski, M., Ross, N., Siana, B., & Teplitz, H. I. 2014, The Astrophysical Journal, 789, 96

Atek, H., Malkan, M., McCarthy, P., Teplitz, H. I., Scarlata, C., Siana, B., Henry, A., Colbert, J. W., Ross, N. R., Bridge, C., Bunker, A. J., Dressler, A., Fosbury, R. A. E., Martin, C., & Shim, H. 2010, The Astrophysical Journal, 723, 104

Atek, H., Siana, B., Scarlata, C., Malkan, M., McCarthy, P., Teplitz, H., Henry, A., Colbert, J., Bridge, C., Bunker, A. J., Dressler, A., Fosbury, R. A. E., Hathi, N. P., Martin, C., Ross, N. R., & Shim, H. 2011, The Astrophysical Journal, 743, 121

Baldwin, J. A., Phillips, M. M., & Terlevich, R. 1981, Proceedings of the Astronomical Society of the Pacific, 93, 5

Bedregal, A. G., Scarlata, C., Henry, A. L., Atek, H., Rafelski, M., Teplitz, H. I., Dominguez, A., Siana, B., Colbert, J. W., Malkan, M., Ross, N. R., Martin, C. L., Dressler, A., Bridge, C., Hathi, N. P., Masters, D., McCarthy, P. J., & Rutkowski, M. J. 2013, The Astrophysical Journal, 778, 126

Bennert, V. N., Auger, M. W., Treu, T., Woo, J.-H., & Malkan, M. A. 2011, The Astrophysical Journal, 742, 107

Bertin, E. & Arnouts, S. 1996, Astronomy & Astrophysics Supplement, 117, 393

Blecha, L. & Loeb, A. 2008, Monthly Notices of the Royal Astronomical Society, 390, 1311

Bongiorno, A., Mignoli, M., Zamorani, G., Lamareille, F., Lanzuisi, G., Miyaji, T., Bolzonella, M., Carollo, C. M., Contini, T., Kneib, J. P., Le Fèvre, O., Lilly, S. J., Mainieri, V., Renzini, A., Scodeggio, M., Bardelli, S., Brusa, M., Caputi, K., Civano, F., Coppa, G., Cucciati, O., de la Torre, S., de Ravel, L., Franzetti, P., Garilli, B., Halliday, C., Hasinger, G., Koekemoer, A. M., Iovino, A., Kampczyk, P., Knobel, C., Kovač, K., Le Borgne, J.-F., Le Brun, V., Maier, C., Merloni, A., Nair, P., Pello, R., Peng, Y., Perez Montero, E., Ricciardelli,

E., Salvato, M., Silverman, J., Tanaka, M., Tasca, L., Tresse, L., Vergani, D., Zucca, E., Abbas, U., Bottini, D., Cappi, A., Cassata, P., Cimatti, A., Guzzo, L., Leauthaud, A., Maccagni, D., Marinoni, C., McCracken, H. J., Memeo, P., Meneux, B., Oesch, P., Porciani, C., Pozzetti, L., & Scaramella, R. 2010, Astronomy & Astrophysics, 510, A56

Brammer, G., Pirzkal, N., McCullough, P., & MacKenty, J. 2014, Time-varying Excess Earth-glow Backgrounds in the WFC3/IR Channel, Tech. rep.

Bromm, V. & Loeb, A. 2003, The Astrophysical Journal, 596, 34

Cardelli, J. A., Clayton, G. C., & Mathis, J. S. 1989, The Astrophysical Journal, 345, 245

Cattaneo, A., Dekel, A., Devriendt, J., Guiderdoni, B., & Blaizot, J. 2006, Monthly Notices of the Royal Astronomical Society, 370, 1651

Coil, A. L., Aird, J., Reddy, N., Shapley, A. E., Kriek, M., Siana, B., Mobasher, B., Freeman, W. R., Price, S. H., & Shivaei, I. 2015, The Astrophysical Journal, 801, 35

Colbert, J. W., Teplitz, H., Atek, H., Bunker, A., Rafelski, M., Ross, N., Scarlata, C., Bedregal, A. G., Dominguez, A., Dressler, A., Henry, A., Malkan, M., Martin, C. L., Masters, D., McCarthy, P., & Siana, B. 2013, The Astrophysical Journal, 779, 34

Conroy, C., Gunn, J. E., & White, M. 2009, The Astrophysical Journal, 699, 486

Domínguez, A., Siana, B., Henry, A. L., Scarlata, C., Bedregal, A. G., Malkan, M., Atek, H., Ross, N. R., Colbert, J. W., Teplitz, H. I., Rafelski, M., McCarthy, P., Bunker, A., Hathi, N. P., Dressler, A., Martin, C. L., & Masters, D. 2013, The Astrophysical Journal, 763, 145

Eddington, A. S. 1926, The Internal Constitution of the Stars

Edelson, R. A. & Malkan, M. A. 1986, The Astrophysical Journal, 308, 59

Erb, D. K., Steidel, C. C., Trainor, R. F., Bogosavljević, M., Shapley, A. E., Nestor, D. B., Kulas, K. R., Law, D. R., Strom, A. L., Rudie, G. C., Reddy, N. A., Pettini, M., Konidaris, N. P., Mace, G., Matthews, K., & McLean, I. S. 2014, The Astrophysical Journal, 795, 33

Felten, J. E. 1977, The Astronomical Journal, 82, 861

Ferland, G. J., Porter, R. L., van Hoof, P. A. M., Williams, R. J. R., Abel, N. P., Lykins, M. L., Shaw, G., Henney, W. J., & Stancil, P. C. 2013, Revista Mexicana de Astronomía y Astrofísica, 49, 137

Ferrarese, L. & Merritt, D. 2000, The Astrophysical Journal Letters, 539, L9

Ford, H. C., Bartko, F., Bely, P. Y., Broadhurst, T., Burrows, C. J., Cheng, E. S., Clampin, M., Crocker, J. H., Feldman, P. D., Golimowski, D. A., Hartig, G. F., Illingworth, G., Kimble, R. A., Lesser, M. P., Miley, G., Neff, S. G., Postman, M., Sparks, W. B., Tsvetanov, Z., White, R. L., Sullivan, P., Krebs, C. A., Leviton, D. B., La Jeunesse, T., Burmester, W., Fike, S., Johnson, R., Slusher, R. B., Volmer, P., & Woodruff, R. A. 1998, in Society of Photo-Optical Instrumentation Engineers (SPIE) Conference Series, Vol. 3356, Space Telescopes and Instruments V, ed. P. Y. Bely & J. B. Breckinridge, 234–248

Froning, C. S. & Green, J. C. 2009, Astrophysics & Space Science, 320, 181

Gebhardt, K., Bender, R., Bower, G., Dressler, A., Faber, S. M., Filippenko, A. V., Green, R., Grillmair, C., Ho, L. C., Kormendy, J., Lauer, T. R., Magorrian, J., Pinkney, J., Richstone, D., & Tremaine, S. 2000, The Astrophysical Journal Letters, 539, L13

Giacconi, R., Zirm, A., Wang, J., Rosati, P., Nonino, M., Tozzi, P., Gilli, R., Mainieri, V., Hasinger, G., Kewley, L., Bergeron, J., Borgani, S., Gilmozzi, R.,

Grogin, N., Koekemoer, A., Schreier, E., Zheng, W., & Norman, C. 2002, The Astrophysical Journal Supplement, 139, 369

Gültekin, K., Richstone, D. O., Gebhardt, K., Lauer, T. R., Tremaine, S., Aller, M. C., Bender, R., Dressler, A., Faber, S. M., Filippenko, A. V., Green, R., Ho, L. C., Kormendy, J., Magorrian, J., Pinkney, J., & Siopis, C. 2009, The Astrophysical Journal, 698, 198

Haardt, F. & Maraschi, L. 1993, The Astrophysical Journal, 413, 507

Hainline, K. N., Hickox, R. C., Greene, J. E., Myers, A. D., Zakamska, N. L., Liu, G., & Liu, X. 2014, The Astrophysical Journal, 787, 65

Hainline, K. N., Shapley, A. E., Greene, J. E., & Steidel, C. C. 2011, The Astrophysical Journal, 733, 31

Hainline, K. N., Shapley, A. E., Greene, J. E., Steidel, C. C., Reddy, N. A., & Erb, D. K. 2012, The Astrophysical Journal, 760, 74

Hao, L., Strauss, M. A., Fan, X., Tremonti, C. A., Schlegel, D. J., Heckman, T. M., Kauffmann, G., Blanton, M. R., Gunn, J. E., Hall, P. B., Ivezić, Ž., Knapp, G. R., Krolik, J. H., Lupton, R. H., Richards, G. T., Schneider, D. P., Strateva, I. V., Zakamska, N. L., Brinkmann, J., & Szokoly, G. P. 2005, The Astronomical Journal, 129, 1795

Häring, N. & Rix, H.-W. 2004, The Astrophysical Journal Letters, 604, L89

Hasinger, G., Cappelluti, N., Brunner, H., Brusa, M., Comastri, A., Elvis, M., Finoguenov, A., Fiore, F., Franceschini, A., Gilli, R., Griffiths, R. E., Lehmann, I., Mainieri, V., Matt, G., Matute, I., Miyaji, T., Molendi, S., Paltani, S., Sanders, D. B., Scoville, N., Tresse, L., Urry, C. M., Vettolani, P., & Zamorani, G. 2007, The Astrophysical Journal Supplement, 172, 29

Heckman, T. M. 1980, Astronomy & Astrophysics, 87, 152

Heckman, T. M., Kauffmann, G., Brinchmann, J., Charlot, S., Tremonti, C., & White, S. D. M. 2004, The Astrophysical Journal, 613, 109

Henry, A., Scarlata, C., Domínguez, A., Malkan, M., Martin, C. L., Siana, B., Atek, H., Bedregal, A. G., Colbert, J. W., Rafelski, M., Ross, N., Teplitz, H., Bunker, A. J., Dressler, A., Hathi, N., Masters, D., McCarthy, P., & Straughn, A. 2013, The Astrophysical Journal Letters, 776, L27

Hopkins, P. F., Hernquist, L., Cox, T. J., Di Matteo, T., Robertson, B., & Springel, V. 2006, The Astrophysical Journal Supplement, 163, 1

Hopkins, P. F., Hernquist, L., Martini, P., Cox, T. J., Robertson, B., Di Matteo, T., & Springel, V. 2005, The Astrophysical Journal Letters, 625, L71

Hopkins, P. F., Richards, G. T., & Hernquist, L. 2007, The Astrophysical Journal, 654, 731

Jeans, J. H. 1902, Royal Society of London Philosophical Transactions Series A, 199, 1

Johnson, J. L., Whalen, D. J., Li, H., & Holz, D. E. 2013, The Astrophysical Journal, 771, 116

Jones, T., Martin, C., & Cooper, M. C. 2015, ArXiv e-prints

Juneau, S., Bournaud, F., Charlot, S., Daddi, E., Elbaz, D., Trump, J. R., Brinchmann, J., Dickinson, M., Duc, P.-A., Gobat, R., Jean-Baptiste, I., Le Floc'h, É., Lehnert, M. D., Pacifici, C., Pannella, M., & Schreiber, C. 2014, The Astrophysical Journal, 788, 88

Juneau, S., Dickinson, M., Alexander, D. M., & Salim, S. 2011, The Astrophysical Journal, 736, 104

Kashi, A., Proga, D., Nagamine, K., Greene, J., & Barth, A. J. 2013, The Astrophysical Journal, 778, 50

Kauffmann, G. & Haehnelt, M. 2000, Monthly Notices of the Royal Astronomical Society, 311, 576

Kauffmann, G. & Heckman, T. M. 2009, Monthly Notices of the Royal Astronomical Society, 397, 135

Kewley, L. J., Dopita, M. A., Sutherland, R. S., Heisler, C. A., & Trevena, J. 2001, The Astrophysical Journal, 556, 121

Kewley, L. J., Groves, B., Kauffmann, G., & Heckman, T. 2006, Monthly Notices of the Royal Astronomical Society, 372, 961

Kimble, R. A., Woodgate, B. E., Bowers, C. W., Kraemer, S. B., Kaiser, M. E., Gull, T. R., Heap, S. R., Danks, A. C., Boggess, A., Green, R. F., Hutchings, J. B., Jenkins, E. B., Joseph, C. L., Linsky, J. L., Maran, S. P., Moos, H. W., Roesler, F., Timothy, J. G., Weistrop, D. E., Grady, J. F., Loiacono, J. J., Brown, L. W., Brumfield, M. D., Content, D. A., Feinberg, L. D., Isaacs, M. N., Krebs, C. A., Krueger, V. L., Melcher, R. W., Rebar, F. J., Vitagliano, H. D., Yagelowich, J. J., Meyer, W. W., Hood, D. F., Argabright, V. S., Becker, S. I., Bottema, M., Breyer, R. R., Bybee, R. L., Christon, P. R., Delamere, A. W., Dorn, D. A., Downey, S., Driggers, P. A., Ebbets, D. C., Gallegos, J. S., Garner, H., Hetlinger, J. C., Lettieri, R. L., Ludtke, C. W., Michika, D., Nyquist, R., Rose, D. M., Stocker, R. B., Sullivan, J. F., Van Houten, C. N., Woodruff, R. A., Baum, S. A., Hartig, G. F., Balzano, V., Biagetti, C., Blades, J. C., Bohlin, R. C., Clampin, M., Doxsey, R., Ferguson, H. C., Goudfrooij, P., Hulbert, S. J., Kutina, R., McGrath, M., Lindler, D. J., Beck, T. L., Feggans, J. K., Plait, P. C., Sandoval, J. L., Hill, R. S., Collins, N. R., Cornett, R. H., Fowler, W. B., Hill, R. J., Landsman, W. B., Malumuth, E. M., Standley, C., Blouke, M., Grusczak, A., Reed, R., Robinson, R. D., Valenti, J. A., & Wolfe, T. 1998, The Astrophysical Journal Letters, 492, L83

Konigl, A. & Kartje, J. F. 1994, The Astrophysical Journal, 434, 446

Kormendy, J. & Richstone, D. 1995, Annual Reviews of Astronomy & Astrophysics, 33, 581

Koski, A. T. 1978, The Astrophysical Journal, 223, 56

Kriek, M. & Conroy, C. 2013, The Astrophysical Journal Letters, 775, L16

Kriek, M., Shapley, A. E., Reddy, N. A., Siana, B., Coil, A. L., Mobasher, B., Freeman, W. R., de Groot, L., Price, S. H., Sanders, R., Shivaei, I., Brammer, G. B., Momcheva, I. G., Skelton, R. E., van Dokkum, P. G., Whitaker, K. E., Aird, J., Azadi, M., Kassis, M., Bullock, J. S., Conroy, C., Davé, R., Kereš, D., & Krumholz, M. 2015, The Astrophysical Journal Supplement, 218, 15

Kriek, M., van Dokkum, P. G., Labbé, I., Franx, M., Illingworth, G. D., Marchesini, D., & Quadri, R. F. 2009, The Astrophysical Journal, 700, 221

Kuemmel, M., Kuntschner, H., & Walsh, J. 2007, Space Telescope European Coordinating Facility Newsletter, 43, 8

Kümmel, M., Walsh, J. R., Pirzkal, N., Kuntschner, H., & Pasquali, A. 2009, Proceedings of the Astronomical Society of the Pacific, 121, 59

Laird, E. S., Nandra, K., Pope, A., & Scott, D. 2010, Monthly Notices of the Royal Astronomical Society, 401, 2763

Lamareille, F., Mouhcine, M., Contini, T., Lewis, I., & Maddox, S. 2004, Monthly Notices of the Royal Astronomical Society, 350, 396

Lamastra, A., Bianchi, S., Matt, G., Perola, G. C., Barcons, X., & Carrera, F. J. 2009, Astronomy & Astrophysics, 504, 73

Lang, D., Hogg, D. W., Mierle, K., Blanton, M., & Roweis, S. 2010, The Astronomical Journal, 139, 1782

Ly, C., Rigby, J. R., Cooper, M., & Yan, R. 2015, The Astrophysical Journal, 805, 45

Madau, P. & Dickinson, M. 2014, Annual Reviews of Astronomy & Astrophysics, 52, 415

Magorrian, J., Tremaine, S., Richstone, D., Bender, R., Bower, G., Dressler, A., Faber, S. M., Gebhardt, K., Green, R., Grillmair, C., Kormendy, J., & Lauer, T. 1998, The Astronomical Journal, 115, 2285

Maier, C., Lilly, S. J., Ziegler, B. L., Contini, T., Pérez Montero, E., Peng, Y., & Balestra, I. 2014, The Astrophysical Journal, 792, 3

Mainzer, A., Bauer, J., Grav, T., Masiero, J., Cutri, R. M., Dailey, J., Eisenhardt, P., McMillan, R. S., Wright, E., Walker, R., Jedicke, R., Spahr, T., Tholen, D., Alles, R., Beck, R., Brandenburg, H., Conrow, T., Evans, T., Fowler, J., Jarrett, T., Marsh, K., Masci, F., McCallon, H., Wheelock, S., Wittman, M., Wyatt, P., DeBaun, E., Elliott, G., Elsbury, D., Gautier, IV, T., Gomillion, S., Leisawitz, D., Maleszewski, C., Micheli, M., & Wilkins, A. 2011, The Astrophysical Journal, 731, 53

Mandel, E. & Tody, D. 1995, in Astronomical Society of the Pacific Conference Series, Vol. 77, Astronomical Data Analysis Software and Systems IV, ed. R. A. Shaw, H. E. Payne, & J. J. E. Hayes, 125

Mannucci, F., Cresci, G., Maiolino, R., Marconi, A., & Gnerucci, A. 2010, Monthly Notices of the Royal Astronomical Society, 408, 2115

Masters, D., McCarthy, P., Siana, B., Malkan, M., Mobasher, B., Atek, H., Henry, A., Martin, C. L., Rafelski, M., Hathi, N. P., Scarlata, C., Ross, N. R., Bunker, A. J., Blanc, G., Bedregal, A. G., Domínguez, A., Colbert, J., Teplitz, H., & Dressler, A. 2014, The Astrophysical Journal, 785, 153

McCarthy, P. J., Yan, L., Freudling, W., Teplitz, H. I., Malumuth, E. M., Weymann, R. J., Malkan, M. A., Fosbury, R. A. E., Gardner, J. P., Storrie-Lombardi, L. J., Thompson, R. I., Williams, R. E., & Heap, S. R. 1999, The Astrophysical Journal, 520, 548

Mehta, V., Scarlata, C., Colbert, J. W., Dai, S., Dressler, A., Henry, A., Malkan, M., Rafelski, M., Siana, B., Teplitz, H., Bagley, M., Beck, M., Ross, N. R., Rutkowski, M., & Wang, Y. 2015, ArXiv e-prints

Oke, J. B. 1974, The Astrophysical Journal Supplement, 27, 21

Park, D., Woo, J.-H., Bennert, V. N., Treu, T., Auger, M. W., & Malkan, M. A. 2015, The Astrophysical Journal, 799, 164

Pirzkal, N., Rothberg, B., Ly, C., Malhotra, S., Rhoads, J. E., Grogin, N. A., Dahlen, T., Noeske, K. G., Meurer, G. R., Walsh, J. R., Hathi, N. P., Cohen, S. H., Bellini, A., Holwerda, B. W., Straughn, A. N., Mechtley, M., & Windhorst, R. A. 2013, The Astrophysical Journal, 772, 48

Rafelski, M., Teplitz, H. I., Gardner, J. P., Coe, D., Bond, N. A., Koekemoer, A. M., Grogin, N., Kurczynski, P., McGrath, E. J., Bourque, M., Atek, H., Brown, T. M., Colbert, J. W., Codoreanu, A., Ferguson, H. C., Finkelstein, S. L., Gawiser, E., Giavalisco, M., Gronwall, C., Hanish, D. J., Lee, K.-S., Mehta, V., de Mello, D. F., Ravindranath, S., Ryan, R. E., Scarlata, C., Siana, B., Soto, E., & Voyer, E. N. 2015, ArXiv e-prints

Richstone, D., Ajhar, E. A., Bender, R., Bower, G., Dressler, A., Faber, S. M., Filippenko, A. V., Gebhardt, K., Green, R., Ho, L. C., Kormendy, J., Lauer, T. R., Magorrian, J., & Tremaine, S. 1998, Nature, 395, A14

Sanders, R. L., Shapley, A. E., Kriek, M., Reddy, N. A., Freeman, W. R., Coil, A. L., Siana, B., Mobasher, B., Shivaei, I., Price, S. H., & de Groot, L. 2015, The Astrophysical Journal, 799, 138

Schramm, M. & Silverman, J. D. 2013, The Astrophysical Journal, 767, 13

Schulze, A. & Wisotzki, L. 2014, Monthly Notices of the Royal Astronomical Society, 438, 3422

Shapley, A. E., Reddy, N. A., Kriek, M., Freeman, W. R., Sanders, R. L., Siana, B., Coil, A. L., Mobasher, B., Shivaei, I., Price, S. H., & de Groot, L. 2015, The Astrophysical Journal, 801, 88

Shen, Y., Greene, J. E., Ho, L. C., Brandt, W. N., Denney, K. D., Horne, K., Jiang, L., Kochanek, C. S., McGreer, I. D., Merloni, A., Peterson, B. M., Petitjean, P., Schneider, D. P., Schulze, A., Strauss, M. A., Tao, C., Trump, J. R., Pan, K., & Bizyaev, D. 2015, The Astrophysical Journal, 805, 96

Shim, H., Colbert, J., Teplitz, H., Henry, A., Malkan, M., McCarthy, P., & Yan, L. 2009, The Astrophysical Journal, 696, 785

Shirazi, M., Brinchmann, J., & Rahmati, A. 2014, The Astrophysical Journal, 787, 120

Soltan, A. 1982, Monthly Notices of the Royal Astronomical Society, 200, 115

Stark, D. P., Richard, J., Charlot, S., Clément, B., Ellis, R., Siana, B., Robertson, B., Schenker, M., Gutkin, J., & Wofford, A. 2015, Monthly Notices of the Royal Astronomical Society, 450, 1846

Stark, D. P., Richard, J., Siana, B., Charlot, S., Freeman, W. R., Gutkin, J., Wofford, A., Robertson, B., Amanullah, R., Watson, D., & Milvang-Jensen, B. 2014, Monthly Notices of the Royal Astronomical Society, 445, 3200

Steidel, C. C., Hunt, M. P., Shapley, A. E., Adelberger, K. L., Pettini, M., Dickinson, M., & Giavalisco, M. 2002, The Astrophysical Journal, 576, 653

Steidel, C. C., Rudie, G. C., Strom, A. L., Pettini, M., Reddy, N. A., Shapley, A. E., Trainor, R. F., Erb, D. K., Turner, M. L., Konidaris, N. P., Kulas, K. R., Mace, G., Matthews, K., & McLean, I. S. 2014, The Astrophysical Journal, 795, 165

Steidel, C. C., Shapley, A. E., Pettini, M., Adelberger, K. L., Erb, D. K., Reddy, N. A., & Hunt, M. P. 2004, The Astrophysical Journal, 604, 534

Stern, D., Assef, R. J., Benford, D. J., Blain, A., Cutri, R., Dey, A., Eisenhardt, P., Griffith, R. L., Jarrett, T. H., Lake, S., Masci, F., Petty, S., Stanford, S. A., Tsai, C.-W., Wright, E. L., Yan, L., Harrison, F., & Madsen, K. 2012, The Astrophysical Journal, 753, 30

Stern, J. & Laor, A. 2012, Monthly Notices of the Royal Astronomical Society, 426, 2703

Straughn, A. N., Pirzkal, N., Meurer, G. R., Cohen, S. H., Windhorst, R. A., Malhotra, S., Rhoads, J., Gardner, J. P., Hathi, N. P., Jansen, R. A., Grogin, N., Panagia, N., di Serego Alighieri, S., Gronwall, C., Walsh, J., Pasquali, A., & Xu, C. 2009, The Astronomical Journal, 138, 1022

Sun, M., Trump, J. R., Brandt, W. N., Luo, B., Alexander, D. M., Jahnke, K., Rosario, D. J., Wang, S. X., & Xue, Y. Q. 2015, The Astrophysical Journal, 802, 14

Tanaka, T. & Haiman, Z. 2009, The Astrophysical Journal, 696, 1798

Teplitz, H. I., Capak, P., Brooke, T., Shenoy, S., Brinkworth, C., Desai, V., Khan, I., & Laher, R. 2010, in Astronomical Society of the Pacific Conference Series, Vol. 434, Astronomical Data Analysis Software and Systems XIX, ed. Y. Mizumoto, K.-I. Morita, & M. Ohishi, 437

Thompson, R. I., Rieke, M., Schneider, G., Hines, D. C., & Corbin, M. R. 1998, The Astrophysical Journal Letters, 492, L95

Treister, E., Schawinski, K., Urry, C. M., & Simmons, B. D. 2012, The Astrophysical Journal Letters, 758, L39

Tremonti, C. A., Heckman, T. M., Kauffmann, G., Brinchmann, J., Charlot, S., White, S. D. M., Seibert, M., Peng, E. W., Schlegel, D. J., Uomoto, A., Fukugita, M., & Brinkmann, J. 2004, The Astrophysical Journal, 613, 898

Treu, T., Malkan, M. A., & Blandford, R. D. 2004, The Astrophysical Journal Letters, 615, L97

Trouille, L. & Barger, A. J. 2010, The Astrophysical Journal, 722, 212

Trump, J. R., Impey, C. D., Elvis, M., McCarthy, P. J., Huchra, J. P., Brusa, M., Salvato, M., Capak, P., Cappelluti, N., Civano, F., Comastri, A., Gabor, J., Hao, H., Hasinger, G., Jahnke, K., Kelly, B. C., Lilly, S. J., Schinnerer, E., Scoville, N. Z., & Smolčić, V. 2009, The Astrophysical Journal, 696, 1195

Trump, J. R., Sun, M., Zeimann, G. R., Luck, C., Bridge, J. S., Grier, C. J., Hagen, A., Juneau, S., Montero-Dorta, A., Rosario, D. J., Brandt, W. N., Ciardullo, R., & Schneider, D. P. 2015, ArXiv e-prints

Vaona, L., Ciroi, S., Di Mille, F., Cracco, V., La Mura, G., & Rafanelli, P. 2012, Monthly Notices of the Royal Astronomical Society, 427, 1266

Veilleux, S. & Osterbrock, D. E. 1987, The Astrophysical Journal Supplement, 63, 295

Woo, J.-H., Treu, T., Malkan, M. A., & Blandford, R. D. 2008, The Astrophysical Journal, 681, 925

Wright, E. L., Eisenhardt, P. R. M., Mainzer, A. K., Ressler, M. E., Cutri, R. M., Jarrett, T., Kirkpatrick, J. D., Padgett, D., McMillan, R. S., Skrutskie, M., Stanford, S. A., Cohen, M., Walker, R. G., Mather, J. C., Leisawitz, D., Gautier, III, T. N., McLean, I., Benford, D., Lonsdale, C. J., Blain, A., Mendez, B., Irace, W. R., Duval, V., Liu, F., Royer, D., Heinrichsen, I., Howard, J., Shannon, M., Kendall, M., Walsh, A. L., Larsen, M., Cardon, J. G., Schick, S., Schwalm, M., Abid, M., Fabinsky, B., Naes, L., & Tsai, C.-W. 2010, The Astronomical Journal, 140, 1868

Zahid, H. J., Kashino, D., Silverman, J. D., Kewley, L. J., Daddi, E., Renzini, A., Rodighiero, G., Nagao, T., Arimoto, N., Sanders, D. B., Kartaltepe, J., Lilly, S. J., Maier, C., Geller, M. J., Capak, P., Carollo, C. M., Chu, J., Hasinger, G., Ilbert, O., Kajisawa, M., Koekemoer, A. M., Kovac, K., Le Fèvre, O., Masters, D., McCracken, H. J., Onodera, M., Scoville, N., Strazzullo, V., Sugiyama, N., Taniguchi, Y., & The COSMOS Team. 2014, The Astrophysical Journal, 792, 75

Zhang, Z. T., Liang, Y. C., & Hammer, F. 2013, Monthly Notices of the Royal Astronomical Society, 430, 2605